Visual Sensing and Defect Detection of Gas Tungsten Arc Welding

A Dissertation Presented for the
Doctor of Philosophy
Degree
The University of Tennessee, Knoxville

Zongyao Chen
May 2019

Copyright © 2018 by Zongyao Chen
All rights reserved.

DEDICATION

To my wife, Jing Wu

ACKNOWLEDGEMENTS

I would like to express my sincere gratitude to my advisor, Dr. Zhili Feng for his valuable guidance and continued support of my Ph.D. research. I would like to thank Dr. Jian Chen from Oak Ridge National Laborary for his supervision and guidance. I truly appreciate my committee members, Dr. William Hamel, Dr. Hahn Choo, Dr. Anming Hu, for their time and valuable suggestions on this dissertation.

The staffs in Oak ridge national lab Dr. Stan David, Dr. Wei Tang, Dr. Hui Huang, Dr. Xinghua Yu, Dr. Zhengang Wu, Dr. Roger Miller, Doug Kyle, Alan Frederick, Shuhong Zhang have been very supportive to my research, and I enjoyed working with them.

I would like to express my deepest gratitude and thanks to my dear parents for their continuous support and guidance. I cannot overcome the difficulties during my doctoral study without their encouragement and suggestions. I also express my appreciation to parents' in law for their help to look after our life in United State.

I would also offer my special thanks to my Wife, Jing Wu, for her endless support and understanding for my research work. Her constant encouragement and support was, in the end, what made this dissertation possible.

ABSTRACT

Weld imperfections or defects such as incomplete penetration and lack of fusion are critical issues that affect the integration of welding components. The molten weld pool geometry is the major source of information related to the formation of these defects. In this dissertation, a new visual sensing system has been designed and set up to obtain weld pool images during GTAW. The weld pool dynamical behavior can be monitored using both active and passive vision method with the interference of arc light in the image significantly reduced through the narrow band pass filter and laser based auxiliary light source.

Computer vision algorithms based on passive vision images were developed to measure the 3D weld pool surface geometry in real time. Specifically, a new method based on the reversed electrode image (REI) was developed to calculate weld pool surface height in real time. Meanwhile, the 2D weld pool boundary was extracted with landmarks detection algorithms. The method was verified with bead-on-plate and butt-joint welding experiments.

Supervised machine learning was used to develop the capability to predict, in real-time, the incomplete penetration on thin SS304 plate with the key features extracted from weld pool images. An integrated self-adaptive close loop control system consisting the non-contact visual sensor, machine learning based defect predictor, and welding power source was developed for real-time welding penetration control for bead on plate welding. Moreover, the data driven methods were first applied to detect incomplete penetration and LOF in multi-pass U groove welding. New features extracted from reversed electrode image played the most important role to predict these defects. Finally, real time welding experiments were conducted to verify the feasibility of the developed models.

TABLE OF CONTENTS

CHAPTER I Introduction 1
1.1 Background and Motivation 1
1.2 Objective 3
1.3 Major Contributions 5
1.4 Organization 7
CHAPTER II Literature Review 8
2.1 Visual Sensing of Weld Pool 8
2.1.1 Weld pool image segmentation 8
2.1.2 Monitoring 3D weld pool geometry 11
2.2 Visual Sensing of Material Deformation during Welding 14
2.3 Penetration Detection and Control in Arc Welding 15
CHAPTER III Monitoring Weld Pool Surface with Active Vision Image 20
3.1 Visual Sensing System Design 20
3.2 Weld Pool Characters in Active Vision Image 22
3.3 Weld Pool Image Segmentation 24
3.4. Experiment Result 26
3.4.1 Experiment parameters 26
3.4.2 Welding current effect 26
3.4.3 Welding speed effect 27
3.5. Discussion 28
3.5.1 Weld pool depression 28
3.5.2 Welding penetration 29
3.5.3 Undercut defect in high speed welding condition 31
3.6. Conclusions 34
CHAPTER IV Visual Sensing of 3D Weld Pool Geometry with Passive Vision Image 35
4.1 Method Overview 35
4.2 Description of 3D Weld Pool Geometry for Bead on Plate Welding 36
4.3 Passive Vision Image Acquisition 37
4.3.1 Hardware system 37
4.3.2 Passive vision images 37
4.4 2D Weld Pool Geometry Measurement with Adaptive Passive Vision Method 39
4.4.1 Conventional image segmentation method 39
4.4.2 Software framework of adaptive passive vision method 40
4.4.3 Landmarks detection 41
4.4.4 Camera exposure time determination based on SVM 41
4.3.4 Experiment validation 44
4.5 Monitoring Weld Pool Surface from Reversed Electrode Image 45
4.5.1 Acquisition of reversed electrode image during GTAW 46
4.5.2 Reflection model of weld pool surface 47
4.5.3 Algorithm of weld pool surface height calculation 49
4.5.4 Experimental validation of SH measurement 51
4.6 Validation of 3D Weld Pool Geometry Measurement 56
4.7. Conclusion 61

CHAPTER V Penetration Prediction with Machine Learning Models 62
5.1 Definition of Welding Penetration 63
5.2 Data Collection 64
5.3 Evaluation Criteria 65
5.4 Linear Regression for Penetration Prediction 67
5.4.1 Linear regression model 67
5.4.2 Feature selection 67
5.5 Penetration Prediction using Artificial Neural Network 70
5.6 Bagging Tree Model Prediction 72
5.7 Penetration Prediction on Butt Joint Welding 75
5.8 Conclusion 78
CHAPTER VI Penetration Control of Bead on Plate Welding 80
6.1 Framework 80
6.2 Modeling Welding Dynamic Behavior 81
6.2.1 Dynamic modeling identification 81
6.2.2 Simulation 83
6.3 Penetration Control on Uniform Thickness Plate 84
6.4 Penetration Control on Different Thickness Plate 87
6.4.1 System modeling 87
6.4.2 Experiment 89
6.5 Conclusion 91
CHAPTER VII Penetration Detection of Narrow U-groove Welding 93
7.1 Welding Parameters 93
7.1.1 Welding joint design 93
7.1.2 Establishment of database 94
7.2 Image Characters of Root Pass Welding 95
7.2.1 Images character of multi-optical sensing condition 95
7.2.2 Acquire images with different welding condition 96
7.3 Training of Prediction Model 99
7.3.1 Classification based on the extracted features 99
7.3.2 Backside width prediction with bag tree model 102
7.4 Experiment Validation 102
7.5 Conclusions 104
CHAPTER VIII Lack of Fusion Detection inside Narrow U-groove 106
8.1. Introduction of Lack of Fusion Defect 106
8.2. Design of Multi-pass Welding Experiments 106
8.3 Experimental Observations 108
8.3.1 Weld bead geometry 108
8.3.2 Characters of passive vision images 112
8.3.3 Features extraction from passive vision image 114
8.4 Predict Lack of Fusion with Data Driven model 115
8.5 Software Integration 118
8.6 Conclusions 118
CHAPTER IX Conclusions and Recommendations 119
9.1 Conclusions 119
9.2 Future Work 122

BIBLIOGRAPHY 123
VITA 132

LIST OF TABLES

Table 1. Welding parameters on 6mm SS304 plate 26
Table 2. Extracted features from detected landmarks 43
Table 3. Welding parameters of surface height measurement 51
Table 4. Welding parameters range of training database 66
Table 5. Description of Input features 66
Table 6. Result of the sequential forward feature selection 69
Table 7. Performance evaluation of ANN regression model 72
Table 8. Performance of predication with bagging tree 74
Table 9. Identified coefficient for the experiment on 2mm workpiece 88
Table 10. Identified coefficient for the experiment on 3mm workpiece 89
Table 11. Optimized PID parameter 90
Table 12. Welding parameters of root pass welding 94
Table 13. Welding parameters of multi-pass narrow gap weld 108
Table 14. Performance of bagging tree model with different training datasets 117

LIST OF FIGURES

Figure 1. Typical defect in a multi-pass weldment 2
Figure 2. Illustration of intelligent welding quality control system 3
Figure 3. Flow chart of developing intelligent welding automation system 4
Figure 4. Process flow chart of an entire pulsed image. (a) Original image; (b) median filtered image; (c) sharpened image; (d) transformed threshold image; (e) fined image; (f) Image after false edge cutting; (g) Image after curve fitting 9
Figure 5. Reflected matrix dot of laser light. (a) acquired reflected image; (b) extracted reflected dots on imaging plane; (c) corresponding projected dots on workpiece ... 12
Figure 6. Welding pool image and its 3D reconstruction using SFS technique 13
Figure 7. The diagram of experimental system for weld pool monitoring during pulsed 16
Figure 8. Weld pool image of weld on aluminum alloy. (a) partial penetrated weld; (b) complete penetrated weld 17
Figure 9. Arc radiation distribution from 200 to 1100 nm 21
Figure 10. Photo of weld pool monitoring system with laser light illumination 22
Figure 11. The active vision weld pool image 23
Figure 12. The tracing ray of laser light on weld pool surface 23
Figure 13. Active vision Welding pool image segmentation 25
Figure 14. Weld pool images under changing current with 2mm/s travel speed 27
Figure 15. Weld pool image under changing welding speed with 250A welding current 28
Figure 16. Weld pool depression area 29
Figure 17. Weld bead width vs. heat input 30
Figure 18. Weld penetration depth vs. heat input 31
Figure 19. CDA vs. penetration depth 32
Figure 20. Cross section view of the weld bead with undercut 32
Figure 21. Schematic of weld pool with under cut 33
Figure 22. Definition of weld pool geometry. (a) Top side view of weld pool top surface; (b) the cross-section view of weld pool 36
Figure 23. Passive vision weld pool image acquisition system 37
Figure 24. Passive vision weld pool image. (a) Image captured with 10 μs exposure time; (b) under exposed weld pool image; (c) right exposed weld pool image; (d) over exposed weld pool image 38
Figure 25. Result of using canny detectors on active and passive vision weld pool images. (a) The original active vision image; (b-c) result of edge detection with threshold 0.15 and 0.45; (d) the original passive vision image; (e-f) result of edge detection with threshold 0.15 and 0.45 39
Figure 26. Flow chart of 2D weld pool geometry measurement with adaptive passive vision method 40
Figure 27. Searching Landmarks on passive vision image 41
Figure 28. Landmarks detection under three exposure condition. (a) Under exposed image; (b) right exposed image; (c) over exposed image 42
Figure 29. (a-c) Landmarks detection on the weld pool image obtained with constant exposure time for experiment 1-3; (d-e) landmarks detection on the weld pool image obtained adaptive controlled exposure time for experiment 1-3 44

Figure 30. Diagram of acquire REI from rear view camera 46
Figure 31. (a) Reflection diagram of concave weld pool surface; (b) reflection diagram of convex weld pool surface..... 47
Figure 32. (a) DERI vs SH; (b) 3D surface plot of DERI vs SH and weld pool width 49
Figure 33. Flow chart of SH calculation 50
Figure 34. (a) Finding REI location in under exposed image; (b) image binarization and window search 50
Figure 35. Weld bead cross section view of experiment 1-4 52
Figure 36. Calculated DERI curve of weld 1-4 54
Figure 37. Reversed electrode image of case 1-4 at 20 second after welding started 54
Figure 38. Calculated SH index of experiment case 1-4 55
Figure 39. Wedge shape SS304 workpiece..... 56
Figure 40. Front view and backside view of weld bead 57
Figure 41. Cross section view of the weld bead 57
Figure 42. Comparison of DERI from image type I 59
Figure 43. Weld pool edge detection from image type II 59
Figure 44. 2D geometry measurement of topside weld pool 59
Figure 45. Measurement of weld pool surface height..... 60
Figure 46. Weld pool surface shape weld in four penetration state during autogenous GTAW. (a) Partial penetration; (b) critical penetration; (c) full penetration; (d) over penetration..... 64
Figure 47. The structure of feedforward neural network for penetration prediction 70
Figure 48. Feature importance analysis 73
Figure 49. A-Topside view of weld bead; B-Back side view of weld bead 75
Figure 50. (a) REI of partial penetrated weld; (b) weld pool image of partial penetrated weld; (c) REI of completed penetrated weld; (d) weld pool image of completed penetrated weld 76
Figure 51. Calculation of weld pool topside width..... 77
Figure 52. Weld pool surface height calculation 77
Figure 53. Prediction of weld pool backside width 78
Figure 54. The schematic diagram of PID closed-loop control system 80
Figure 55. (a) Input signal of step test; (b) output signal of step test 82
Figure 56. PID control system blocks using simulink 83
Figure 57. (a)Observation of input current; (b) observation of system output 83
Figure 58. Topside view and backside view of weld bead with non-optimized PID gains 84
Figure 59. Output signal of non-optimized PID gains 85
Figure 60. Topside view and backside view of weld bead with optimized PID gains 86
Figure 61. System output with optimized PID gains 86
Figure 62. Static correlations between the welding current and backside width on different thickness plate 87
Figure 63. The schematic diagram of self-tuning PID closed-loop control system..... 90
Figure 64. Topside view and backside view of weld bead on non-uniform thickness plate 90
Figure 65. (a) Input current during welding on non-uniform thickness plate; (b) output backside width during welding on different thickness plate..... 91

Figure 66. Design of narrow U groove welding joint 93
Figure 67. Images acquired during U-groove welding with changing exposure time..... 95
Figure 68. Features extracted from passive vision image 96
Figure 69. Passive vision images of 5 welds with different welding current 97
Figure 70. Passive vision images of 3 welds with different root face 98
Figure 71. Comparison of the four features under three penetration conditions 99
Figure 72. Out-of-bag error vs number of grown trees 101
Figure 73. Predictor importance estimates 101
Figure 74. Error distribution for training and testing. (a) Error of the training dataset; (b) error of the testing dataset 102
Figure 75. Three penetration condition inside U groove weld. (a) Incomplete penetrated weld performed at 100A current and 1mm/s welding speed; (b) complete penetrated weld performed at 130A current and 1mm/s speed; (c) over penetrated weld performed at 150A current 103
Figure 76. Real time backside width prediction of root pass weld 104
Figure 77. Schematic of layer plan in U-groove joint 107
Figure 78. Description of weld pool surface inside U groove 109
Figure 79. Topside view of the multi pass weld on workpiece I 110
Figure 80. Cross section views of the finished weld joint on workpiece I 110
Figure 81. Topside view of the multi pass weld on workpiece II 111
Figure 82. Cross section views of the finished weld joint on workpiece II 111
Figure 83. Passive vision images under lack of fusion condition 113
Figure 84. Passive vision images under complete fusion condition 113
Figure 85. Features extraction from weld images 114
Figure 86. Extracted features of the third weld with lack of fusion defect 115
Figure 87. Comparison of feature in fusion and lack of fusion condition 116
Figure 88. Software interface for LOP and LOF detection 118

LIST OF ABBREVIATIONS AND SYMBOLS

LOF	Lack of fusion
IP	Incomplete penetration
2D	Two dimensional
3D	Three dimensional
REI	Reversed electrode image
DERI	Distance between REI and electrode
SH	Surface height
Wt	Weld pool topside width
Lt	Weld pool trailing length
SVM	Support vector machine
ANN	Artificial neural network
SFS	Sequential feature selection
ASM	Active shape model
PCA	Principal component analysis
BW	Backside width
RMSE	Root mean square error
MAE	Mean absolute error
MSE	Mean square error
SVD	Singular value decomposition
PID	Proportional–integral–derivative
RF	Root face

CHAPTER I
INTRODUCTION

1.1 Background and Motivation

Welding is one of the most important technologies in manufacturing industry. Among the hundreds of welding technics which have been applied to the assembling and joining of metal material, the gas tungsten arc welding is one of the most commonly used technology for the welding and joining of stainless steel, carbon steel and aluminum. GTAW (also known as TIG welding) uses a non-consumable tungsten tip with protection of inert shielding gas to conduct the weld. Currently, this process can be conducted manually or automatically. The manual GTAW is a relatively difficult technic for human welders to master. And longtime exposure to the strong arc and dangerous gases produced during welding is harmful to human welders' health. Hence the cost of manual welding remains high for many manufacturing industries. Automatic GTAW is performed by robotic or automatic welding system which highly increased the efficiency of production. The welding parameters such as welding current, welding speed are usually predetermined before automatic welding. However, it is very difficult to proactively adjust the welding parameters in real-time to compensate unexpected variations that will cause welding defects.

According to the industrial standards and codes, such as the ASME Boiler & Pressure Vessel Code[1], the typical welding defect can be found in the multi-pass weldment such as incomplete penetration, lack of fusion, porosity and cracks as shown in Figure 1. The incomplete penetration (IP): It happens when the weld bead does not penetrate the toe of a fillet weld but only bridges across it. Lack of fusion (LOF): This

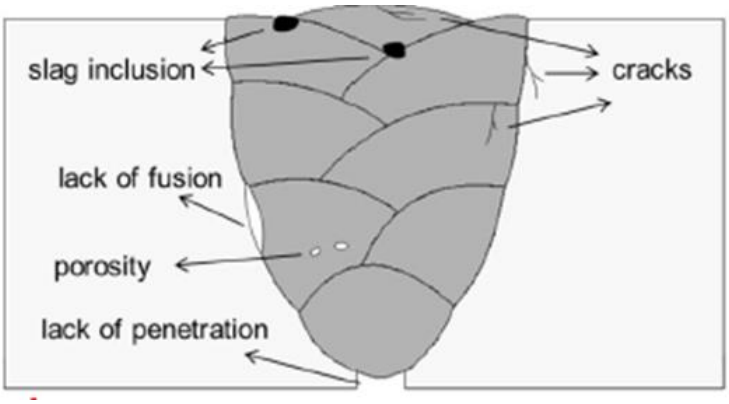

Figure 1. Typical defect in a multi-pass weldment

type of defect usually occurs due to the poor adhesion of the current weld bead to the base metal or adjoining weld beads. Cracks: As the most detriment defects, the cracks can grow under tensile stress resulting in component failure. The locations of cracks can be near and under the weld surface[2].

These defects left in the welding structure is a major threat to the safety for the structural components such as pipe-line or the pressure vessel[3]. The detection and repairing of these defects are time consuming and expensive.

In manual welding, the adjustment can be made by the well-trained welder to produce a high-quality weld without defects. However, the welding quality highly rely on the experience of the human welder which may vary from person to person. Second, some operations at special hazard environment such as nuclear industry may not suitable for the human welder to participate in the task. For these reasons, recent years have seen growing demands for developing intelligent welding control system which can automatic adjust the weld parameter during welding process and produce high quality weld with less defect.

Although, a number of researches have been conducted to develop intelligent arc welding system to reduce welding defect[4-6]. They are still far from practical application in industry. The major issue is how to detect welding defect during the GTAW process. Since there no direct measurement of weld defect in real time is available, in-direct measurement should be developed with advanced sensing technology.

1.2 Objective

The research goal is to develop an intelligent automatic welding monitoring system with vision sensing for real-time weld defect detection and adaptive adjustment to the welding process conditions to eliminate or minimize the formation of major weld defects including incomplete penetration and lack of fusion.

As shown in Figure 2, a new integrated sensing system was developed to monitoring the weld pool behavior and collect signals during TIG welding. Intelligent control software was developed based on the computer vision algorithm and artificial intelligent method to simulate the human welder's knowledge and behavior to make decisions based on the information of weld pool geometry.

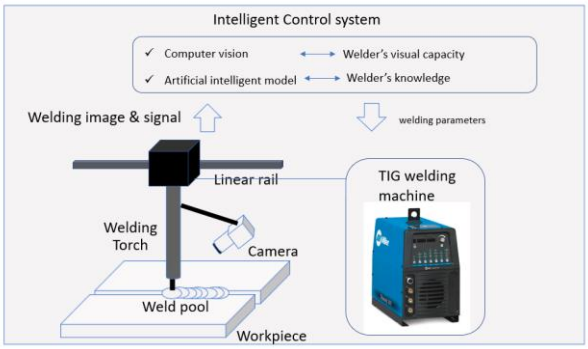

Figure 2. Illustration of intelligent welding quality control system

The outline of the research is shown in Figure 3, the first part of research is to monitor the 3D weld pool geometry during welding process. A new integrated sensing system was established to acquire the weld pool images and collect signals during TIG welding process. Image processing algorithms were developed to quantitatively measure the topside weld pool geometry with computer vision method.

As shown in Figure 2, the visual sensing system includes a weld pool surface measurement camera and the necessary auxiliary illumination sources and optical filters. The visual sensing system can obtain weld pool image using both passive vision method and active vision method. The active vision image is obtained with laser light illumination, while the passive vision image is obtained without auxiliary illumination. Besides that, arc voltage sensor and current sensor is also integrated into the hardware system. Software implementation is required to quantitatively measure the weld pool geometry. Image segmentation algorithm will be developed to extract the weld pool profile.

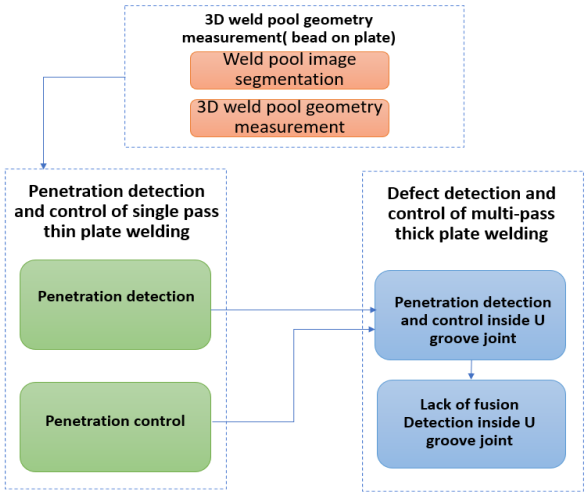

Figure 3. Flow chart of developing intelligent welding automation system

The feature from 2D weld pool geometry such as weld pool width and length were automatically calculated through the software. Then, the feature extracted from weld pool surface will be further investigated and quantitatively related to the weld pool surface height.

The second part is to detect incomplete penetration and control penetration on autogenous bead-on-plate weld. All the variables measured from part I can be used to predict weld penetration state in real time. The machine learning method was established to improve the accuracy of backside width prediction. A close loop penetration control system was further established based on the feedback form machine learning model.

In the third part of research, we focus on detect incomplete penetration and lack of fusion for multi-pass welding in U-groove. In real welding condition, the autogenous butt joint welding is more often applied on weld thin plate. Filler wire welding inside groove type joint is more applicable on thick workpiece. However, the weld pool measurement of groove type welding is significantly affected by the shape of weld joint. More experiment studies were conducted on the U-groove joint welding to monitor the defect including lack of fusion and penetration. New algorithm was developed to detect and eliminate lack of fusion and incomplete penetration in real time welding.

1.3 Major Contributions

This research aims at developing a novel system using multiple visual sensing techniques to monitor the GTAW process. Systematic method was established based on the theory and technology from multiple field including computer vision, machine learning, welding technology and control theory. Through these efforts, the huge human labor and

maintenance cost can be saved which will significantly increase the quality and efficiency in manufacturing industry. The specific contributions are listed as follows,

1. Established a new welding monitoring system to obtain weld pool image during GTAW. The interference of arc was significantly reduced through the narrow band pass filter and laser based auxiliary light.
2. Observe weld pool dynamical behaviors during GTAW process using both active and passive vision method. Study and compare the weld pool geometry between partial and full penetration.
3. Develop new weld pool edge detection algorithm to measure weld pool 2D geometry in real time. The algorithm can determine the optimal camera exposure condition using support vector machine (SVM) method. It can automatically track weld pool boundary with sufficient accuracy and robustness.
4. Developed a new method based on reversed electrode image (REI) to calculate the weld pool surface height (3D information) via 2D weld pool mage in real time.
5. Detected welding penetration during autogenous bead on plate welding using machine learning approach. Features related to 3D weld pool geometry was calculated using real time software. Welding backside width (BW) was predicted using regression model. The accuracy of prediction was further improved after feature selection.
6. Implemented welding penetration feed-back control system based on the predicted backside width. Developed the self-tuning PID controller to adjust

welding current in real time. Conducted welding experiment on the workpiece with different thickness.

7. Established a new data driven model to predict penetration for the root pass weld in U-groove joint. The essential features were extracted from reversed electrode images.
8. Studied the REI under multi pass welding inside U-groove joint. Established a bagging tree classification model to determine the fusion condition based on the features extracted from reversed electrode images.

1.4 Organization

Chapter 2 reviews the related works in the welding process defect detection and control using visual sensing and artificial intelligent method. In Chapter 3, weld pool surface geometry is studied based on the active vision images. Chapter 4 descripts the adaptive passive vision system to measure the 3D weld pool surface geometry for bead on plate welding. Chapter 5 presents penetration prediction with machine learning approach for bead on plate weld and butt joint weld. The implementation of close loop penetration control system is presented in Chapter 6. Penetration detection was further applied on the U-joint, and the implementation and experiment result is presented in Chapter 7. Chapter 8 presents the lack fusion detection in multi-pass welding U-groove joint. Chapter 9 draws the conclusions.

CHAPTER II
LITERATURE REVIEW

2.1 Visual Sensing of Weld Pool

Many sensing techniques have been attempted to monitor weld quality such as radiographic sensing[7], visual sensing[8, 9], ultrasonic/acoustic sensing[10], arc voltage and current measurement[11]. Recently, the vision sensing approaches has drawn more and more attention since it can directly monitor the weld pool dynamic characters during arc welding process. In manual welding, a skilled welder determines weld quality based on his/her observation of weld pool top surface. Many researchers [12-17] have been motivated to develop instruments or sensing system to monitor the weld pool which is important way to detect the weld defect including incomplete penetration, lack of fusion and porosity during welding process. In this section, the related works of measuring weld pool geometry with visual sensing method are first discussed.

2.1.1 Weld pool image segmentation

Extract weld pool boundary from the acquired images is the first task of visual sensing. Although many image processing algorithms have been developed, weld pool segmentation task remains challenging due to the following reasons: First, the interference from intensive arc light affect the quality of weld pool image. Second, the variation of weld pool boundary can be very different from one welding application to another. Third, some of the object including the electrode and the droplet may hide part of the weld pool boundary. Early researchers applied conventional edge detection method, which work on images without the presence of strong arc light. As shown in Figure 4, an edge detection procedures proposed by a previous researcher was applied on the aluminum GTAW [18].

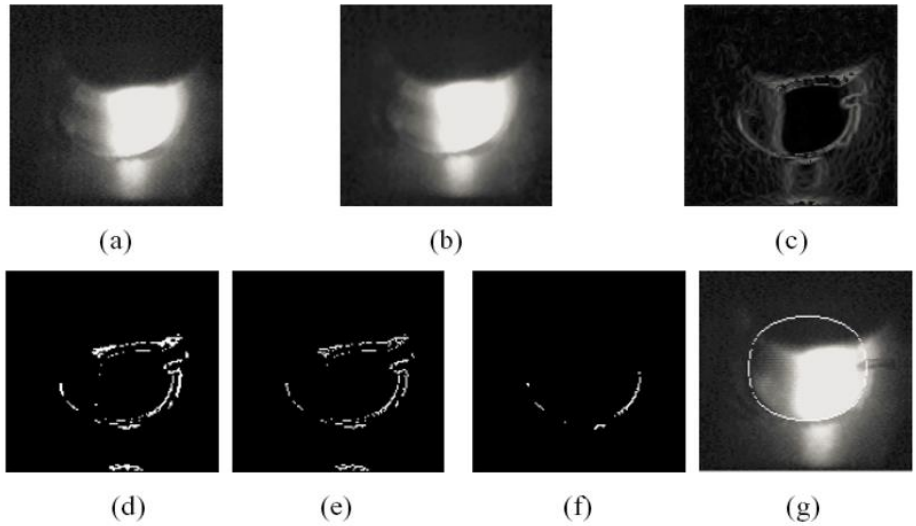

Figure 4. Process flow chart of an entire pulsed image. (a) Original image; (b) median filtered image; (c) sharpened image; (d) transformed threshold image; (e) fined image; (f) Image after false edge cutting; (g) Image after curve fitting

A passive vision system was established to obtain the weld pool image without the present of additional light source. Edge detection procedures are as follows. First enhance the image with filters [15, 19-21]. Next step is to select region of interest (ROI) [22, 23] to decrease processing time and to decrease noise. ROI can be determined automatically or manually. Following is to threshold into binary image by automatically determining the threshold [18]; by fixed threshold [20]; by fuzzy logic local thresholding [24]. Last step is boundary generation by thinning [20, 21], template matching [21, 24], curve fitting [18] , clustering [24].

In passive vision system, the arc light that was utilized as the light source may also overwhelms important features in the image. An alternative approach is to use the auxiliary laser light to illuminate the weld pool area[25] which is known as the active vision system. In [26], the weld pool boundary was extracted from laser light illuminated active vision

image with sufficient accuracy. Useful features including weld pool width, weld pool length and size were calculated and further applied in the adaptive control of welding penetration. However, all these methods using conventional segmentation method to extract the weld pool profile were verified on the weld within a certain range of welding and optical conditions.

In some practical welding condition, the weld must be performed on designed joint type such as butt joint, V- groove and U shape groove joint. The weld pool edge is more difficult to detect inside these joint due to the pool illumination condition inside the welding joint.

Conventional segmentation method such as edge detection, thresholding, and region-based techniques may be affected by noise and artifacts due to lack of ability of handling prior knowledge. Deformable models, on the other hand, incorporate prior knowledge such that it is more robust to noise and the presence of foreign objects. Deformable models are curves or surfaces that move under certain driving forces. Deformable models can be classified into three categories: active contour models (ACM), level set methods and active shape models (ASM).

Deformable models have been used for weld pool segmentation in various types of welding processes. Snakes were used in [27] and [28] for extracting weld pool boundary in GMAW and [9] for laser welding. In [27], the active contour with an application-dependent prior using adaboost is proposed to track the weld pool during GMAW. These algorithms were implemented with sufficient accuracy to detect the weld pool contour inside V-groove joint.

In [29], level set method was used to detect welding defects with small shapes in images characterized by low contrast level. Active shape model was used in [30] for weld pool segmentation in Plasma arc welding. Shi et al [31] used a part-based model for visual detection and localization of gas tungsten arc weld pool.

2.1.2 Monitoring 3D weld pool geometry

Three-dimensional geometry of weld pool in principle would provide more comprehensive information for penetration detection[8]. However, extracting the 3D information remains a challenging task for welding automation.

As an active vision method, structural light has been reported in a series of papers for 3D reconstruction of weld pool [32-36]. In their works, a structured laser pattern is projected onto the weld pool at a certain angle and laser light is reflected on an image plane. A high-speed camera equipped with a bandpass filter is used to capture the reflected laser pattern. Triangulation principle is applied to reconstruct the height information of the weld pool.

An early attempt has been made by Zhang et al. [26] to observe the three-dimensional weld pool surface with a commercial camera whose shutter was synchronized with a short duration pulsed illumination laser. This camera eliminated the bright arc light from the image and the two-dimensional boundary of the weld pool was clearly imaged. For three-dimensional weld pool surface imaging, the illumination laser is projected through a frosted glass to form multiple strips. However, due to the difficulty of precise system positioning, the system is only used for 3D observation not 3D measurement. Moreover, the camera is expensive, and the frame rate can only reach 30 frames per second.

The same group [32-34, 37] further developed a structured light technique to reconstruct 3D weld pool surface in GTAW. Laser light was projected onto the weld pool surface using dot-matrix pattern as shown in Figure 5, and the reflected laser light is received on an image plane. The projected points are then matched with the reflected ones to reconstruct the weld pool surface. The reconstruction results and the accuracy are quantitively discussed in [37]. The surface depth of the weld pool extracted from 3D reconstruction is used for real time control of welding penetration.

The structural light method usually obtains clear weld pool images without interference from arc light. However, it requires extra light source and is not cost efficient in real application. Shape from Shaping (SFS) is a 3D reconstruction technique that recover the three-dimensional information from variation of shading in a 2D image. It is first introduced by Horn [38] in 1970s. In this paper, a Lambertian model in Eq. (2.1) that maps the surface orientation of each scene point (x,y) to the pixel intensity in the 2D image.

$$I = R(p,q) \tag{2-1}$$

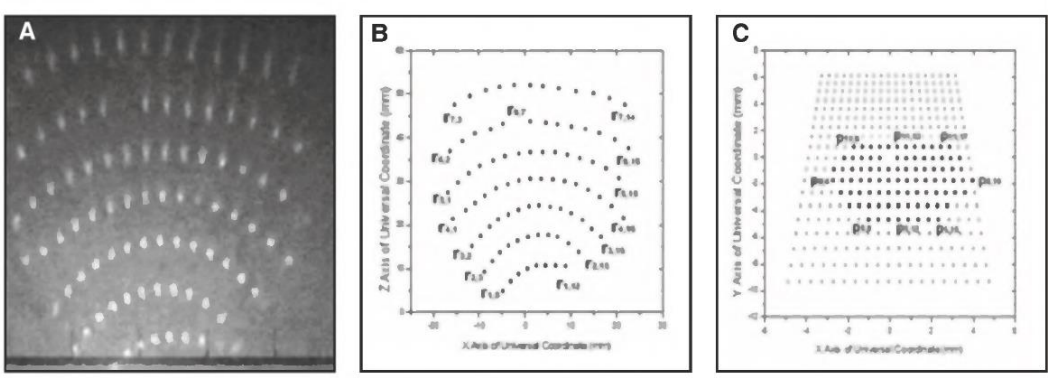

Figure 5. Reflected matrix dot of laser light. (a) acquired reflected image; (b) extracted reflected dots on imaging plane; (c) corresponding projected dots on workpiece

where $R(p,q)$ is the reflectance map of the surface point (x,y), $p = \frac{\partial z}{\partial x}$, $q = \frac{\partial z}{\partial y}$, z is the surface height, I is the normalized pixel intensity at each pixel (x,y).

The inverse problem of recovering surface shape from the known pixel intensity, I, is known as the shape from shading problem[39]. To find the unique solution of this problem, additional constraint is required. Ruo Zhang, et al. [40] divided the existing solutions into four groups: minimization, propagation, local and linear. Zhao, et al. [41, 42] first introduced SFS into welding field on. The SFS techniques applied in welding 3D reconstruction are all based on minimization theory. In his research, the SFS technique is used in passive vision image as shown in Figure 6, which does not require additional light source. Thus, it is cost efficient. However, it assumes that the light source is ideal, which is away from the illumination of arc light. Moreover, the weld pool image is interfered with noises, which may cause the image intensity deviate from the reflection model. In addition, it is difficult to determine illuminant direction. All these conditions may affect the accuracy of SFS method.

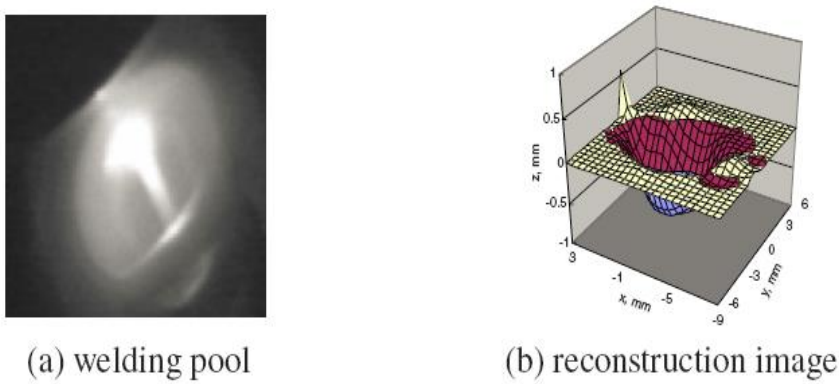

(a) welding pool (b) reconstruction image

Figure 6. Welding pool image and its 3D reconstruction using SFS technique

Stereo vision is another method to extract 3D information from digital images obtained by two or more CCD cameras. Mnich and his colleagues used a stereovision method to determine the 3D shape of the weld pool [43]. By comparing information about a scene from two or more viewpoints, 3D information can be extracted by examination of the relative positions of objects in the two planes. The main error in this system comes from the correspondence process.

2.2 Visual Sensing of Material Deformation during Welding

The strain analysis is essential to understand the formulation of residual stress and distortion during arc welding. The conventional strain measurement using strain gauge is not suitable for high temperature conditions. Digital image correlation (DIC) technique is a non-contact vision sensing method that can measure the full-field displacement and strain on the material surface. Normally the surface of the material was pre-painted with random speckle pattern. The principle of using DIC is to find the maximum of the correlation array between pixel intensity array subsets on the corresponding images of material surface.

Although strain measurement using DIC has been studied for several years[44-51] and attempted in some welding applications[51-54], in-situ DIC measurement during welding is still very challenging. First, the intense welding arc light affects the quality of the images obtained from camera sensor. Second, the speckle pattern on the surface is vulnerable to the high temperature. When the measurement gets close to the welding torch, the thermal and electromagnetic radiation imposes significant influence on the optical system. Strycker et al.[55] applied DIC on the tube during arc welding. Coules et al. applied DIC to measure the strain at 20mm and 30mm away from the weld line[56]. However,

most of these experimental measurements were conducted far away from the fusion zone, or at the back side of the workpiece. Recently, a new high-temperature DIC has been successfully developed to measure the strain field adjacent to the weld pool[57]. In ref [58, 59], the measured strain was further related to the distortion of work piece.

Thermal history in materials during welding is another critical factor affecting the quality of the weldment[57] . Previous studies suggest non-uniform thermal expansion and liquid metal shrinkage near the weld pool result in weld distortion and residual stresses[56, 60]. The infrared camera (IR) can be used to acquire the full temperature field. Based on the temperature measurement, the thermal expansion of the material was further calculated and related with the formation of residual strain and stress.

In my previous work, a newly-developed integrated optical system was utilized to monitor material's thermal and strain field adjacent to the fusion line during GTAW process[61]. It was found that the variation of the measurement data could be positively correlated to the change of welding parameters and the characteristics of the final weldment[62, 63].

2.3 Penetration Detection and Control in Arc Welding

Penetration has been a long-standing issue that affects safety and integrity of welded structures [4, 64, 65]. Many sensing and measurement technology have been developed to monitor welding penetration in decades.

The geometry weld pool can is a major source of information related to welding penetration. Extended researches were conducted using vision sensing approach to

detection penetration using infrared camera or high-speed digital camera [66-68] [5, 69, 70].

In bead on plate and butt joint welding, the backside weld pool width can directly indicate the penetration. As the full penetration started, a second weld pool surface was formulated on the backside on the base metal. An experiment setup which can monitoring the backside weld pool image during GTAW was developed as shown in Figure 7. The welding penetration can be directly detected from the weld pool image on back side. However, monitoring weld pool backside image can be a challenge task in real application such as welding inside the pipeline.

Monitoring of weld pool top side image requires less complex experiment setup. As shown in Figure 8, the 2D geometry of weld pool top surface can be identified from the passive vision weld pool image[41, 42, 69, 71]. Significant different of weld pool geometry can be found between partial penetration weld and full penetration weld[71]. Based on the features extracted from topside weld pool, the backside weld pool geometry can be calculated using predicted model.

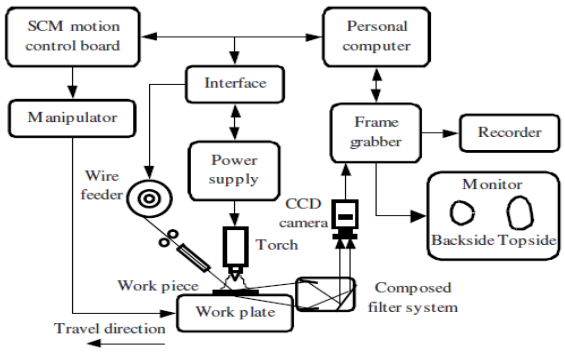

Figure 7. The diagram of experimental system for weld pool monitoring during pulsed

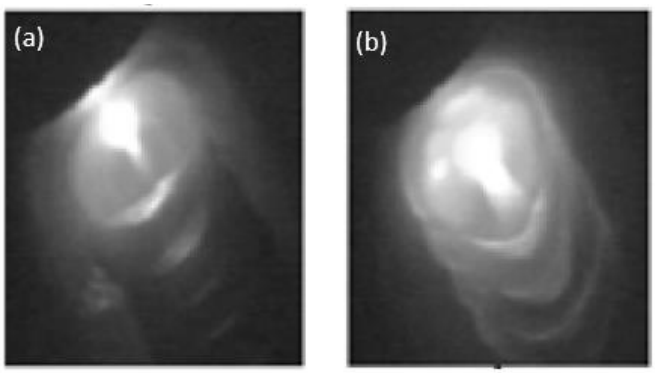

Figure 8. Weld pool image of weld on aluminum alloy. (a) partial penetrated weld; (b) complete penetrated weld

In reference[26, 36], the geometry characters such as weld pool width, length were measured from active vision weld pool images. The artificial neural network model was applied to predict back side width. The feedback control system was then established to control weld penetration in real time. The algorithms to detect of 2D weld pool geometry characters are discussed in 2.1.1.

The weld pool surface height can also be extracted base on the 3D weld pool surface reconstruction discussed in in section 2.1.2. In reference[72], the convexity of the weld pool top surface was calculated and used as a feature to detect penetration. In[73], the weld pool surface height was estimated using machine vision method and further related to the penetration during pulsed gas metal arc welding(P-GMAW) process[74].

The penetration depth of the weld pool is an important variable to describe the welding penetration. However, the depth of penetration cannot be observed from the surface of the weldment. In reference[35, 75], ultrasonic senor was applied to detect welding penetration depth from the received ultrasonic signal. The real time close loop control system was established as reported in previous reference[76].

Recently, the researchers from Kentucky University developed an analytic model to computer the depth of the weld penetration based on the computed temperature distribution and measured 3D weld pool surface which provided a possible way to estimate the penetration depth inside the welding material[77].

Several studies found out that the weld pool oscillation was related to penetration during Pulse GTAW. In pulsed GTAW, the weld current was changed from pulse current to base current repeatedly which trigger the oscillation. In reference[78-81], the arc voltage was used to monitor the oscillation of weld pool during Pulse-GTAW process. The oscillation was found in the voltage signal due to the minor fluctuation of arc length. By using, oscillation frequency was extracted with FFT transform of the voltage signal. The oscillation frequency was reduced during full penetration state compare with partial penetration state. The oscillation frequency was also extracted from the reflection of laser pattern using high speed camera. The method can be further applied to detect penetration in real time[79].

The sound of welding is useful source of information for sensing. During manual welding, the welder could distinguish a good weld and the bad weld based on the sound. In reference[82, 83], the welding sound were studied through time domain, frequency domain and wavelet transform. Different features were extracted and further correspondence to the penetration state of weld.

From the research pattern created by University of Kentucky, the measurement of arc length can be used to monitoring penetration in Pipe welding. The arc length can be measured from the arc voltage [84, 85] . The measured arc voltage increases as the arc

length increasing. In reference[72, 86], the detection of welding penetration was developed based on the assumption of the weld pool surface dynamic behavior. During the partial penetration stage, arc length and arc voltage was found reduced due to the elevation of weld pool top surface. The arc voltage was then decreased as the full penetration was created. The feedback control algorithm was further developed based on this assumption.

CHAPTER III
MONITORING WELD POOL SURFACE WITH ACTIVE VISION IMAGE

A new weld pool monitoring system was established with laser light illumination, allowing us to observe the dynamic weld pool geometry during welding. In this chapter, the weld pool dynamic behavior under different welding current and speed was studied.

Section 3.1 presents the implementation of active vision sensing system. Section 3.2 presents the weld pool characters with active vision image, welding pool surface depression can be observed in many experiment conditions; In section 3.3, a Robust algorithm was developed to extract features from images based on image registration method. Section 3.4 presents the experiment result from Monitoring Surface condition and welding pool depression under different current and speed. In Section 3.5, the formation of welding surface depression, welding penetration and undercut welding defect was further discussed. The conclusion was drawn in section 3.6.

3.1 Visual Sensing System Design

The intensive arc is major issue to monitoring the weld pool dynamic property during GTAW. The intensity distribution of arc radiation during GTAW with argon gas is shown in Figure 9. Arc radiation distribution from 200 to 1100 nm [87]. The spectrum covers the wavelength from 200 to 1100nm. It is worth nothing that the spectrum between 650 to 950 nm contains most intensive radiation. Band pass filter can be used reduce the arc radiation. Hence, the selection of band pass filter will avoid this range.

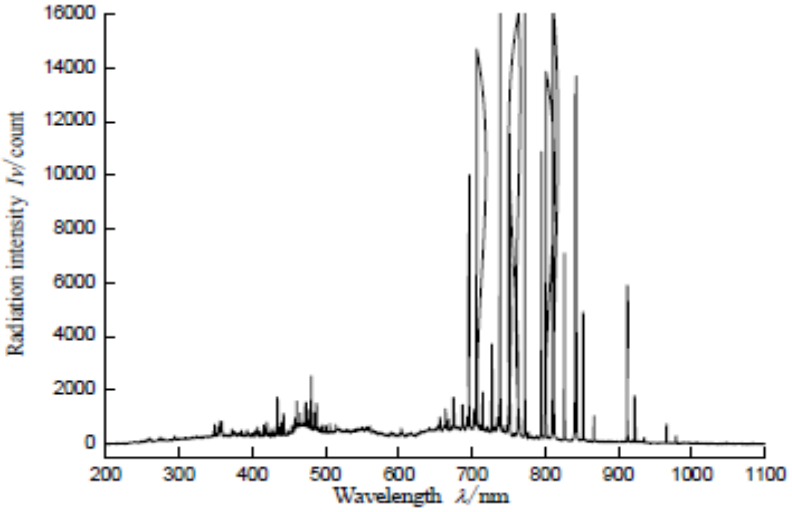

Figure 9. Arc radiation distribution from 200 to 1100 nm

The interference of arc light can be completely suppressed with bandpass filters. Additional method was made to further eliminate the rest arc light. One method is to adjust the camera exposure time and aperture to reduce the brightness of the whole image. The arc light can be suppressed by reducing the exposure time and aperture. However, the weld pool may not be visualized if the image is under exposed. Thus, the selecting a right camera exposure time and aperture is required to observe the weld pool shape. In many researches, it is called as passive vision method since there is no auxiliary light source is used and the arc light become the only light source. The other way is to used laser light as the light source while eliminate the arc light during the weld. The arc light can be almost suppressed with very short exposure time. Meanwhile, the synchronized laser light was projected on the weld pool area. The wavelength of the laser light can be selected to be able to pass the band pass filter. Such method was also called as active vision method since optical system has its own light source. The diagram of experiment system is shown in Figure 10, The welding torch was set perpendicular to the work pieces. Welding direction is towards left.

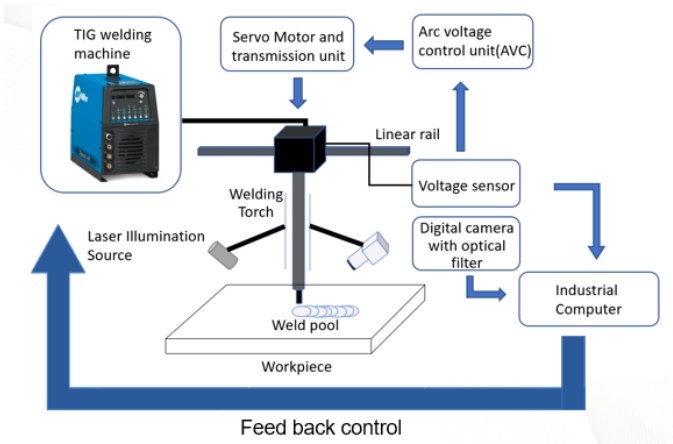

Figure 10. Photo of weld pool monitoring system with laser light illumination

The Laser illumination light was set at front side of the welding direction with the incident angle of 45°. A high-speed camera was set on the opposite side. A diffuser was added in front of the camera lens to increase the illumination area. Thus, the illuminated area can be increased to cover the whole welding pool. The laser light and digital camera was fixed with the welding torch. To eliminate the effect of arc light, a band-pass filter with specific wavelength was added in the front of camera lens and only the laser light and only limited amount of arc light was able to pass through the filter.

3.2 Weld Pool Characters in Active Vision Image

The typical weld pool image obtained with active vision method was shown in Figure 11. The effect of arc light was suppressed, and the laser light became the major light source. The reflection of the laser light was received by the digital camera on the opposite side of the laser light source. As shown in the diagram of tracing ray of light in Figure 12, the surface of the metal near the weld pool area produced the diffuse reflection which can be visualized in the image.

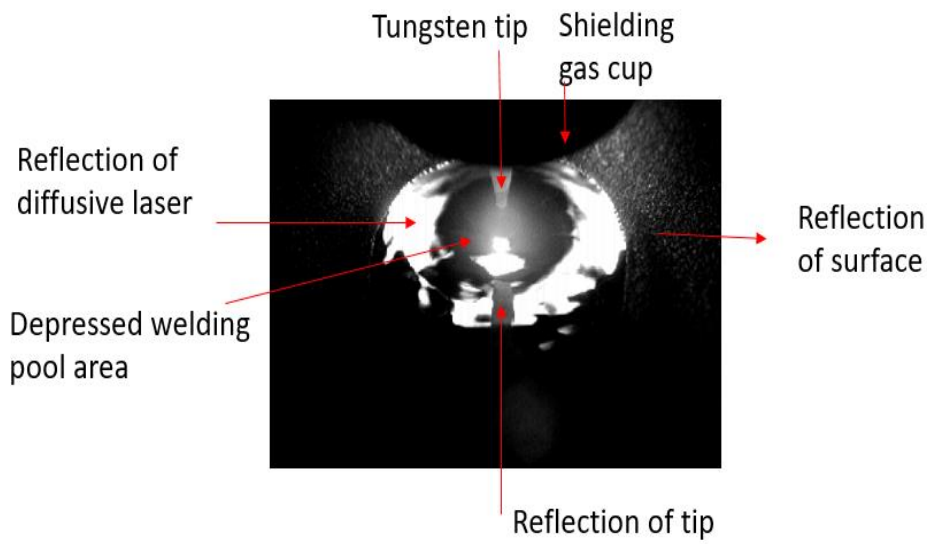

Figure 11. The active vision weld pool image

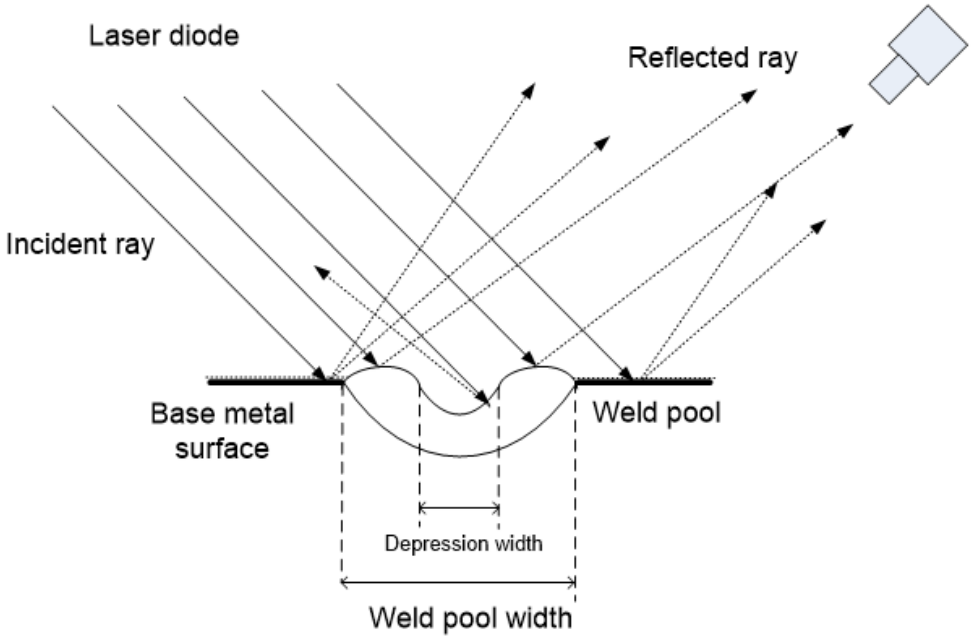

Figure 12. The tracing ray of laser light on weld pool surface

The mirror like weld pool surface produced the specular reflection of the laser light. Previous research indicated that if the weld current is beyond 200A, the intensity plasma jet impinges which may produce a depressed area in the central of weld pool[88]. This area was defined as center depressed area (CDA) in the following description. In Figure 11, the intensity of CDA was much lower than the outside area of weld pool since the reflection of laser light cannot be captured from CCD camera due to the deep surface depression. A continues circular shape white area was formed around CDA which is defined as light reflection area (LRA). The weld pool surface inside LRA is relatively close to a flat surface. Therefore, the reflection of laser light inside LRA can be captured by CCD camera.

3.3 Weld Pool Image Segmentation

The detection of weld pool boundary is required to measure the weld pool geometry from the image. Base on the intensity change on different area in the weld pool image. Algorithm 1 was developed to automatically extract the edge of weld pool from the laser reflection image using conventional image processing operations.

In the original weld pool image, there are lot of edge belongs to shielding gas cup and the tungsten tip which increase the challenge of algorithm design. The proposed method utilized the edge of the laser reflected area which is close to the weld pool's edge.

As shown in Figure 13, the laser light reflected area(LRA) can be distinguished from rest part of image after image banalization. However, this area not continues, small reflection from the surface remains in the binary image. By taking morphological filter can reduce these small dots outside the area of weld pool.

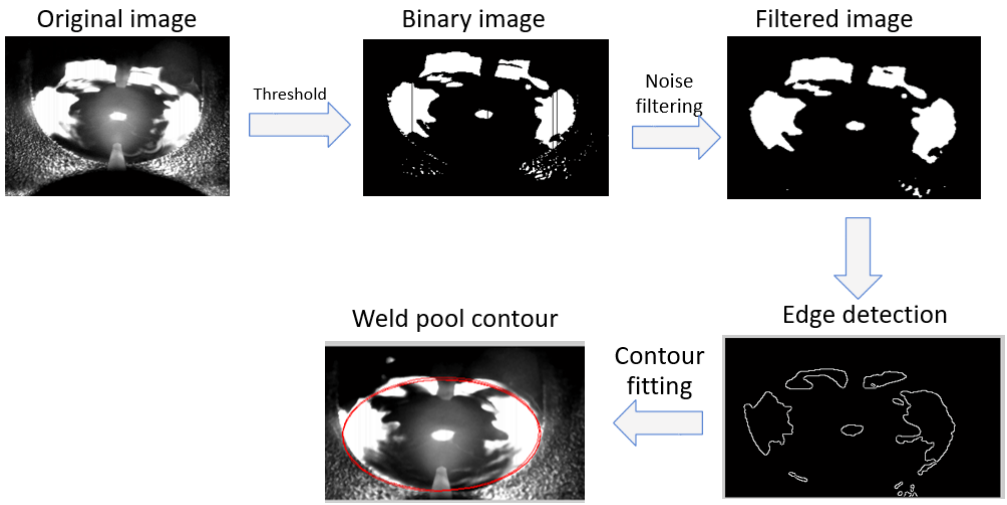

Figure 13. Active vision Welding pool image segmentation

Algorithm 1 Active vision weld pool image segmentation

Input: Image of weld pool, reference location on electrode
Output: ellipsoid contour of weld pool
1: Locate the center of weld pool based on the reference location
2: Compute binary image.
3: Remove the noise on the image using Median filter
4. Reduce the reflection on the material surface using morphological method
5: Initial the ellipsoid contour
6. Using the LRA as the reference image, and align the ellipsoid contour to the edge of the LRA image

The weld pool shape is close to an ellipsoid. Based on the LRA image, the edge of the welding pool was fitted using an ellipsoid shape contour model with optimal length and width. The LRA plays the most important role for the proposed algorithm. And the algorithm has been validated in many bead-on-plate experiments. However, due to the dynamic change of LRA under different speed and current. The accuracy may be affected. The limitations of the algorithm are listed as follows,

1) The algorithm can be applied on the welding condition with low traveling speed.

2) The rear edge cannot be detected due to insufficient illumination.

3) The reflection on the unmelted area many affect the contour detection. Thus, the surface finish of the material must be kept at constant level.

3.4. Experiment Result

3.4.1 Experiment parameters

Weld pool geometry was highly related with the current and travel speed. In this section, the bead on plate welding experiment with different current and travel speed were conducted on 6mm SS304 work piece. The welding voltage was controlled through AVC unit. The welding parameters are listed in Table 1. After each weld, the weld beads were section and etched. The penetration depth can be measured after welding.

3.4.2 Welding current effect

The weld pool surface depression, surface tension and weld penetration has been found highly related to with the welding current. The weld pool images with different current at 2mm/s welding speeding are shown in Figure 14. For the case of welding current less than 200A, the effect of arc pressure is insignificant, and the area of depression is small. The numerical study indicated that the weld pool surface can be considered as a flat surface if the current is less than 200A[89-91].

Table 1. Welding parameters on 6mm SS304 plate

Parameters	Value
Shielding gas	100% Argon
Gas flow rate	30 CFH
Electrode diameter	2.4mm
Voltage	12V
Current	(100,130,160,200,250,300,350,400) A
Welding speed	(1.5,2,3.3,6.5) mm/s
Arc length	2-5.1mm

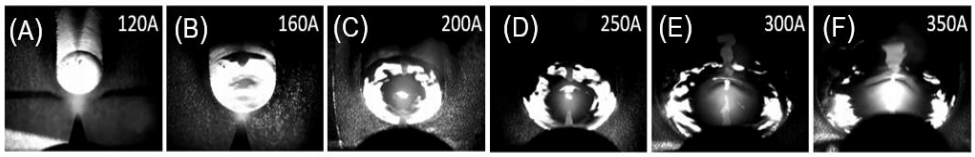

Figure 14. Weld pool images under changing current with 2mm/s travel speed

In Figure 14 (A-B), the LRA occupied the whole weld pool surface and the whole weld pool area was saturated which indicated that the flat weld pool surface was produced.In Figure 14 (C-F), the low intensity of the weld pool center indicated that the weld pool center was depressed with the increased of welding current. The numerical study also find out that the weld pool depression will significantly increase due to the arc pressure for high current GTAW above 200A [88, 91]. The arc pressure formulates a depression area in the center of the weld pool underneath the electrode. The arc force will also push the liquid pool towards the side of the weld pool area if the weld is partially penetrated. The simplified relationship between welding current and arc plasma force can be described as follows:

$$F_{arc}=\mu_o I^2/8\pi \tag{3-1}$$

μ_o is magnetic permeability of vacuum. The arc force was found approximately proportional to the square of current.

3.4.3 Welding speed effect

In Figure 15, the weld pool width and the width of the depression area were compared under four different speed and same welding current. The volume of weld pool was decreased as the travel speed increased. The depression can be found at four conditions. However, the depression area at low travel speed (less than 2mm/s) located in

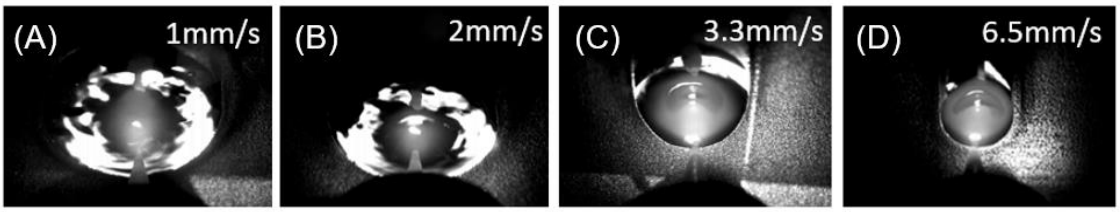

Figure 15. Weld pool image under changing welding speed with 250A welding current

the center of the pool as shown in Figure 15(A-B). As the travel speed goes up, the weld pool width was decreased, and the depression area only occupied the front of the pool. The liquid was pushed toward the rear part of the weld pool. And the width of the depressed area is same as the weld pool width.

3.5. Discussion

3.5.1 Weld pool depression

Figure 16 shows all the calculated depression area of the weld pool for different travel speed and welding current based on the active vision image. The calculation is based on the image pixels of the CDA. The real area can be calculated with calibration. The CDA was found positively related with welding current. For all the welding speed, the CDA is quite small and can be neglected at current below 160. The flat surface model is valid for low current condition. As the current increase above 200A, the CDA is significantly increased due to the increase of arc pressure.

For the low welding speed condition at 1.5mm/s and 2mm/s, the empirical equation (3-2) can be calculated based on the experiment data. The linear correlation can be found when the current is above 135A.

$$A=0.3813*current-50.238 \quad (3\text{-}2)$$

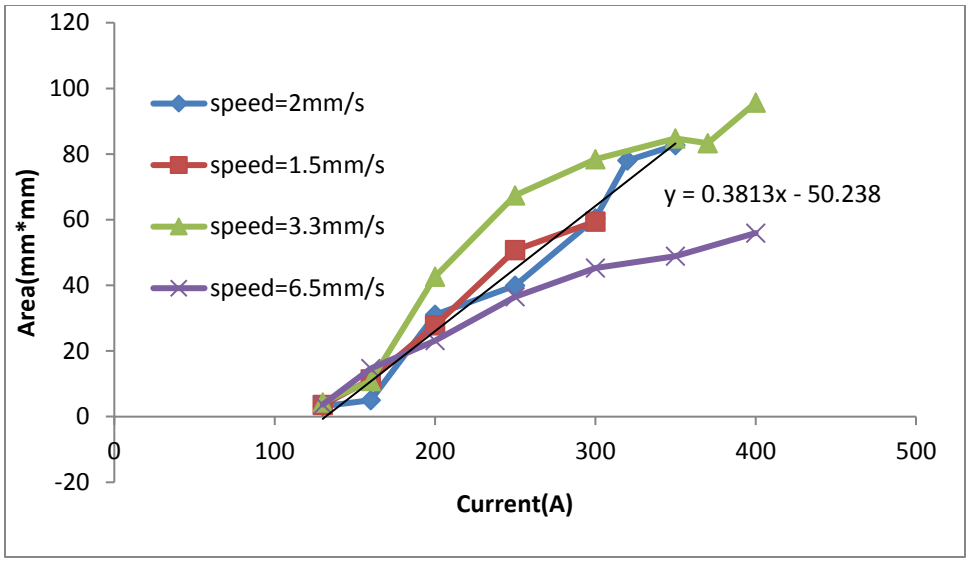

Figure 16. Weld pool depression area

The increasing rate of CDA with current is significantly between the high speed welding condition and the low speed condition. For high speed welding conditions, the arc pressure may not be the domain factors of CDA. Due to the increase of welding speed, the heat input was reduced which result in the decreasing of weld pool volume.

3.5.2 Welding penetration

The weld penetration was further analysis based on the cross-section view of weld bead. The weld bead width and penetration depth are the major variables to evaluate the penetration. The measured weld bead width vs. heat input is shown in Figure 17.

The calculation of heat input is described as follows,

$$Heat\ input = \frac{Voltage \times Current}{Travel\ speed} \tag{3-3}$$

Heat input unit(J/s), speed unit (mm/s)

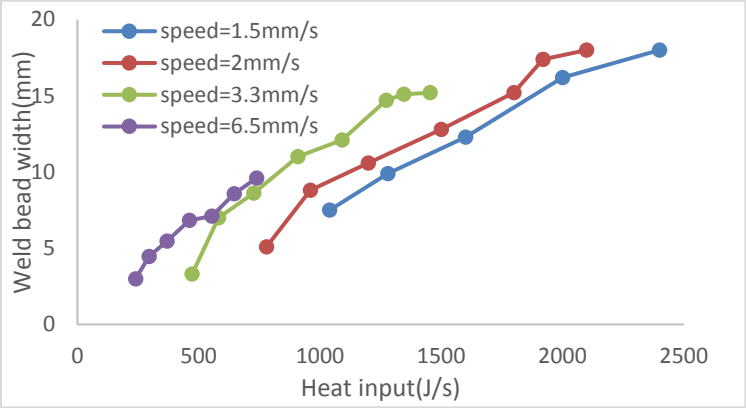

Figure 17. Weld bead width vs. heat input

The weld pool width was increased with current and decreased with increasing of travel speed. For the same welding speed, the weld bead width linearly increased with heat input. The heat input to produce the same weld width with high speed welding is less than the low speed condition.

The measured weld penetration depth vs. heat input is shown in Figure 18 . For same welding speed, the penetration depth linearly increased with heat input as the penetration depth is lower than 4mm. The weld partially penetrated the 6mm plate. A small increase of heat input changed the partial penetrated weld with 4mm penetration depth into full penetration (above 6mm).

In equation (3-4), the empirical model was established to estimate penetration depth from welding current and speed. The model was calculated with least square fitting method based on the experiment data.

$$D=0.0199*I-0.0336*V-0.0007*I*V-1.5485 \qquad (3\text{-}4)$$

It is worth nothing that working condition of this model is restrict for the bead on plate weld on 6mm SS304 plate without filler wire, and the welding voltage is controlled

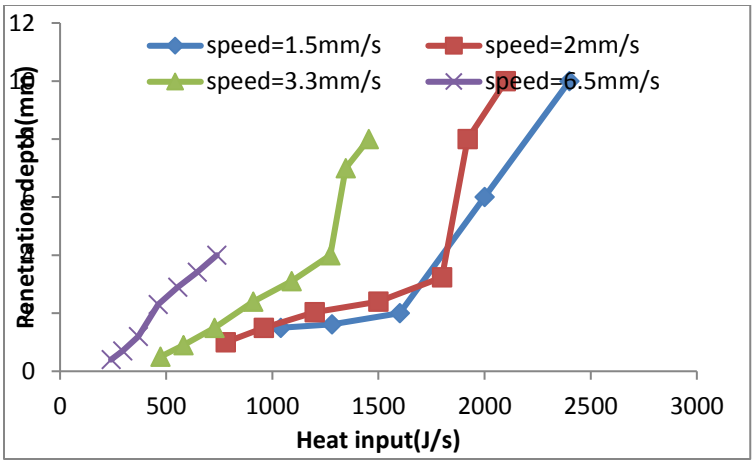

Figure 18. Weld penetration depth vs. heat input

under 12V through AVC control unit. It is assumed that the weld is under partial penetration in which the penetration depth is below 4mm. If the calculated result is above 4mm, a complete penetration may occur. The heat input to produce a same weld penetration depth using high speed condition is less than the low speed condition. The high speed welding condition also produced a high depth to width ratio compare to low speed welding. Hence, the high current and high speed welding condition is more energy efficient to achieve same penetration depth compare to welding with low current and low speed. The calculated depression area from weld pool image vs. penetration depth is shown in Figure 19. The depression area was increased with penetration depth as the penetration depth was below 4mm. The increasing rate was decreased as the weld is close to full penetration.

3.5.3 Undercut defect in high speed welding condition

Although high speed welding can achieve better efficiency, the welding speed was limited due to the defect of undercut or humping[92]. These defects reduced the integrity of welding joint. Figure 20 shows the cross-section view of the weld bead with undercut.

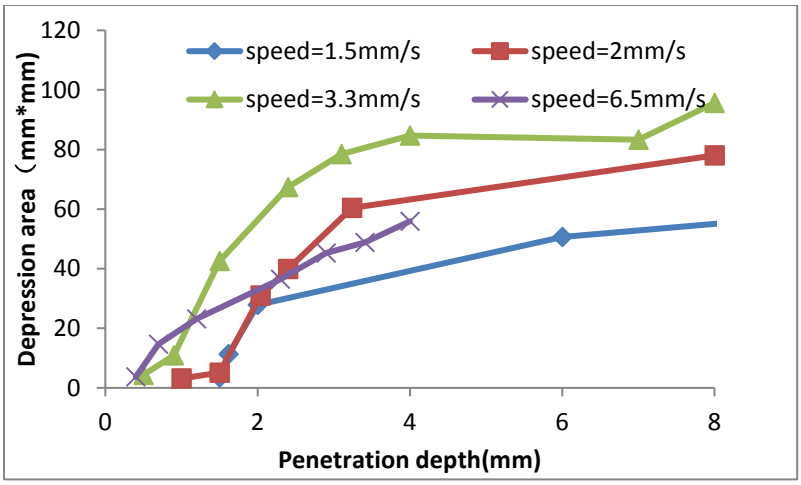

Figure 19. CDA vs. penetration depth

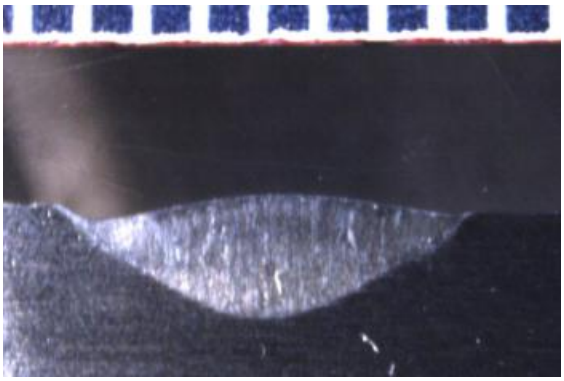

Figure 20. Cross section view of the weld bead with undercut

The defect was formulated under 6.5mm/s welding speed and 250A welding current. The undercut created the sharp groove on the side of weld bead unfilled by the solidified weld metal. The formation of under cutting may relate to surface tension, arc pressure and metallostatic pressure. The arc pressure balance model proposed by Yamauchi and Taka[93] explained the formation of undercut. The schematic of weld pool side view during welding is shown in Figure 21, there is a static balance between the arc pressure and metallostatic pressure[92]. If the metallostatic pressure is higher than the arc pressure, weld pool liquid exists underneath the arc. Conversely, if the arc pressure is much higher than metallostatic pressure, the weld pool liquid will be pushed towards the tail of the pool. An arc gouging region was formulated underneath the electrode. The undercut was produced when travel speed is too fast, and the molten pool failed to fill the arc gouging region before solidification and left a gap on the boundary of the weld bead. The weld pool image with under cutting defect is shown in Figure 15 (D). Due to the concave shape of arc gouging region, the intensity of this area was much lower than the surrounding area. The liquid existed at tail of weld pool. The solidified bead width is less than the width of the weld pool. A gap can be visualized at the trail of weld pool which indicates the formulation of undercut defect.

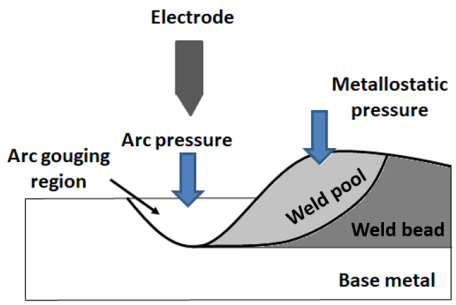

Figure 21. Schematic of weld pool with under cut

3.6. Conclusions

In this section, new image acquisition system based on laser light reflection was established to observe the weld pool top surface shape during bead on plate welding. Experimental study was conducted under different welding speed and current condition. The following conclusion can be draw based on the experiment result,

1. The depression on weld pool surface can be visualized with the reflection of laser light.

2. Arc plasma force creates depression on the weld pool top surface during the GTAW. The force is proportional to the square of the current. The depression is insignificant for the low current. And the welding pool surface can be considered as a flat surface.

3. A significate depression was produced for the high current welding above 200A. The weld pool cannot be considered as a flat surface. For low speed welding condition, CDA is increased with the current.

4. It was found that the welding penetration depth for partial penetrated weld linearly increased with heat input during same welding speed. The penetration depth increased rapidly with the heat input as the weld close to full penetration. The high speed welding achieves better efficiency to produce same penetration depth compare with the low speed welding condition.

5. The undercut defect was found during welding with 6.5mm/s speed. Hence, the up limit of welding speed is required to avoid this defect.

CHAPTER IV
VISUAL SENSING OF 3D WELD POOL GEOMETRY WITH PASSIVE VISION IMAGE

4.1 Method Overview

Three-dimensional weld pool surface geometry provides important information for welding defect detection during arc welding. In this chapter, new algorithms were developed to measure the weld pool 3D geometry based on the two-dimensional passive vision images. The passive vision system does not need additional light source. Compare to the active vision images, the passive vision image does not have interference from laser light reflection and the experiment setup is simple.

However, extracting weld pool geometry from camera with passive vision method remains challenging due to the interference of arc light. It was found out that the interference of arc light in the weld pool image can be effectively controlled by adjusting the camera exposure time based on the decision made from machine learning classifier. Meanwhile, new method was established to calculate the surface height (SH) from the reverse electrode image (REI). The method presented here established the foundation for real time penetration monitoring and control.

In the following part, Section 4.2 provides the definition of the 3D welds pool geometry. Section 4.3 describes the method to acquire passive vision images. Section 4.4 described the algorithm to detect 2D weld pool edge with adaptive passive vision method. Section 4.5 discussed the new method to calculated weld pool surface height based on the REI. In section 4.6, the bead on plate experiment was conducted on wedge shape plate. The weld pool width, trailing length and surface height (SH) was calculated in real time and the result agrees well with the measurement of weld bead geometry.

4.2 Description of 3D Weld Pool Geometry for Bead on Plate Welding

An illustration of the variables related to 3D weld pool geometry in bead on plate welding is shown in Figure 22. In Figure 22(a), the topside view contains 2D information of weld pool top surface. A tear-drop-shaped weld pool surface is formulated for bead on plate weld. Where the L is the total length of the weld pool, W_t is the width of the weld pool top surface. Point C is the center of the weld pool which is underneath the tungsten electrode. The distance between OC is defined as front length L_f . The weld pool trailing length L_t is defined as the distance between point C and D. Welding penetration and travel speed can change the ratio between trailing length and the total length. The tear drop shape will change to ellipsoid shape if the trailing length is reduced.

Figure 22(b) descripts the cross-section view of the weld pool at full penetration condition. The surface height is defined as distance between the base metal surface and the vertex of weld pool surface. SH is less than zero as a concave surface is formulated. Weld backside width W_b and root reinforcement on the backside of workpiece are the direct variables to describe welding penetration.

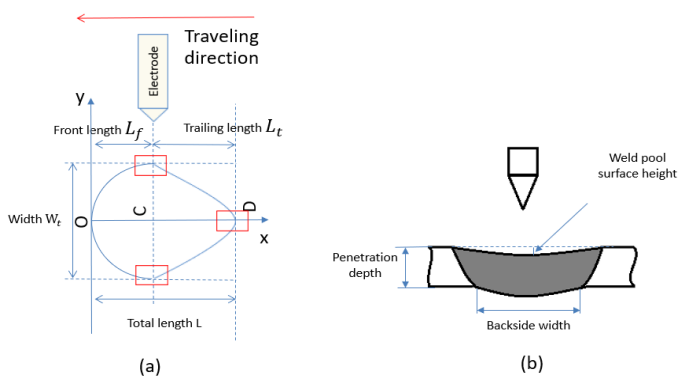

Figure 22. Definition of weld pool geometry. (a) Top side view of weld pool top surface; (b) the cross-section view of weld pool

4.3 Passive Vision Image Acquisition

4.3.1 Hardware system

The configuration of the passive vision weld pool image acquisition system is shown in Figure 23. The welding torch was set perpendicular to the work piece. The hall-effect current sensor and arc voltage control unit was integrated into the welding system to measure the welding current and voltage in real time. The high speed digital camera was mounted on the right side of the moving torch following the welding direction. A band pass filter was placed in front of the CCD camera to reduce the interference of arc light. The camera exposure time and aperture are the important factors to change the image intensity.

4.3.2 Passive vision images

In passive vison mode, no active laser light was applied during welding. The reflection of arc light was used as the major illuminations. By changing the camera exposure time and aperture, the intensity of the passive vision image can be adjusted.

Figure 23. Passive vision weld pool image acquisition system

The passive vision images obtained under different camera exposure time are shown in Figure 24. The exposure time is increased from Figure 24(a) to (b). As shown in Figure 24(a), most of the arc light was suppressed at 10 μs exposure time. And the tungsten electrode and the reversed electrode image (REI) were visible in the image.

In Figure 24 (B), as the weld pool image was obtained at 40 μs, the intensity of the arc was increased, and the REI was blocked by the saturated arc light. The weld pool edge was not visible due to the insufficiently illumination. In Figure 24(c), as the camera exposure time is increased to 100 μs, the weld pool edge became clearly visible. However, the saturated arc area only blocks the weld pool front edge. The over exposure image is shown in Figure 24(d), the size of saturated area expands as the exposure time is increased to 700 μs. The intense arc overwhelms the whole weld pool and weld pool edge is not visible. Therefore, 100 μs is the right exposure time to extract weld pool profile for this condition. Since the weld pool size varies with different welding parameters, the range of right exposure time is also changed accordingly.

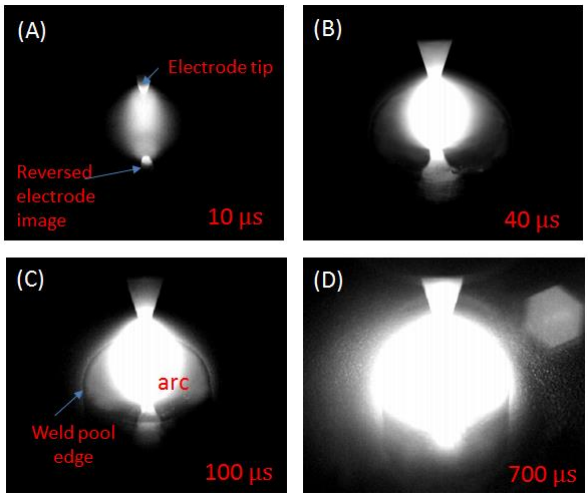

Figure 24. Passive vision weld pool image. (a) Image captured with 10 μs exposure time; (b) under exposed weld pool image; (c) right exposed weld pool image; (d) over exposed weld pool image

4.4 2D Weld Pool Geometry Measurement with Adaptive Passive Vision Method

4.4.1 Conventional image segmentation method

To calculate the parameters of the weld pool geometry, image segmentation is required to detect the weld pool edge first. Many image segmentation methods have been developed for this task.

In Figure 25, The canny edge detection was applied on both laser reflection image (a) and passive vision image (d)in same welding condition. The threshold of canny detector was changed from 0.15 to 0.45. The weld pool edge was covered by large amounts of pseudo edge. These pseudo edges belong to the feature such as saturated arc area, unmelted surface, reflection of laser. Hence, it remains challenge to distinguish the edge belongs to weld pool from other edges.

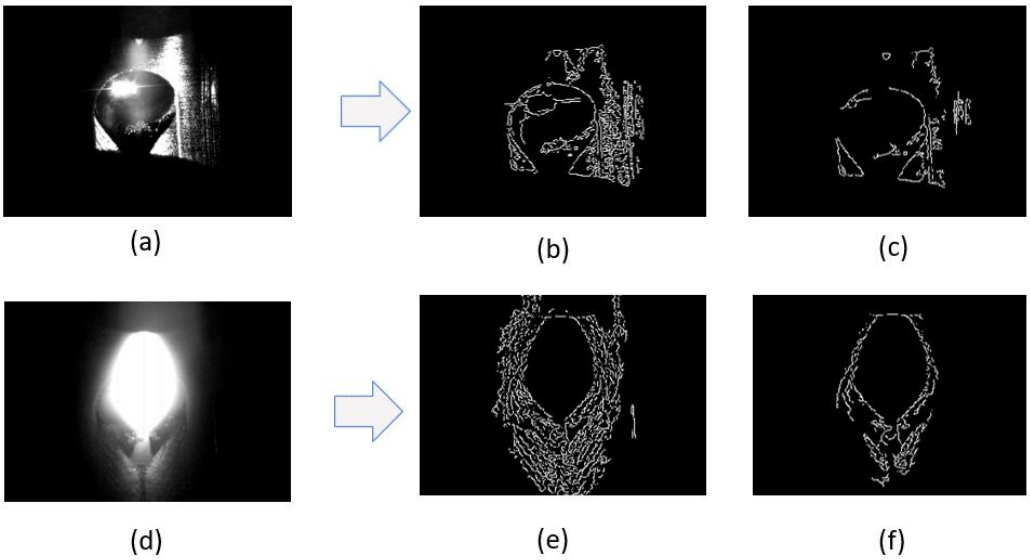

Figure 25. Result of using canny detectors on active and passive vision weld pool images. (a) The original active vision image; (b-c) result of edge detection with threshold 0.15 and 0.45; (d) the original passive vision image; (e-f) result of edge detection with threshold 0.15 and 0.45

4.4.2 Software framework of adaptive passive vision method

The flow chart of the software to measure the 2D weld pool geometry is shown in Figure 26. First, the weld pool image was acquired with a given exposure time. Landmark searching was conducted on the weld pool image. The features related with camera exposure condition were generated based on the distribution of the detected landmarks. SVM classification model was trained to determine the exposure condition of the weld pool image. If the weld pool image was under exposed or over exposed, the camera exposure time will be regulated until the right exposed image was obtained. Once the weld pool image is right exposed, the landmarks can be found on the edge of the weld pool. The weld pool edge was fitted based on the detected landmarks. Then, two-dimensional weld pool geometry such as weld pool width and weld pool length can be calculated with the detected weld pool edges.

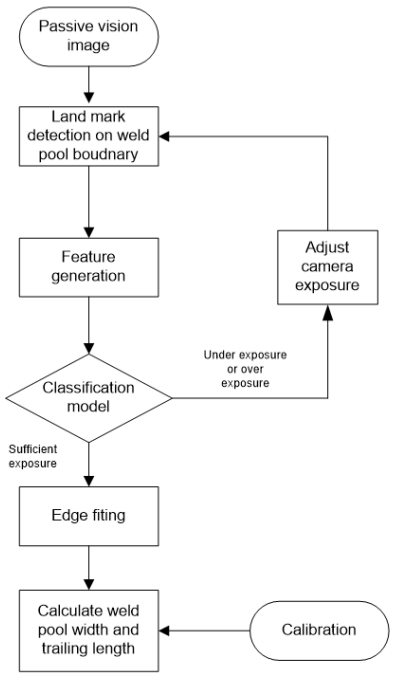

Figure 26. Flow chart of 2D weld pool geometry measurement with adaptive passive vision method

4.4.3 Landmarks detection

The landmarks searching method were mostly used in the shape analysis of image object. There are two major functions for the landmark detection in this algorithm. First, the useful features related with camera exposure condition were extracted based on the distribution of landmarks. Second, these landmarks were used to determine weld pool edge for the weld pool image obtained at right exposure condition. As shown in Figure 27, the detection of landmarks was conducted along the scanning lines in vertical and horizontal direction. Each landmark was generated based on the intensity variation along one scanning lines. There are three kinds of landmarks generated from the weld pool images. The red landmarks indicated the maximum intensity gradient along the vertical scanning line in Figure 27(A). In Figure 27(B), the green landmarks indicated the maximum intensity gradient along the horizontal scanning line, and the yellow landmarks indicated the edge of saturated arc light area.

4.4.4 Camera exposure time determination based on SVM

The camera exposure time can affect the accuracy of landmarks detection. As shown in Figure 28(A), the green landmarks on the weld pool side edge can hardly be detected correctly due to the insufficient exposure.

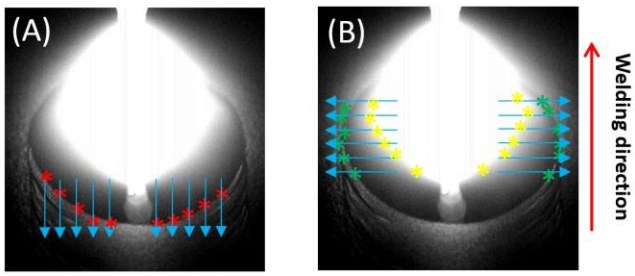

Figure 27. Searching Landmarks on passive vision image

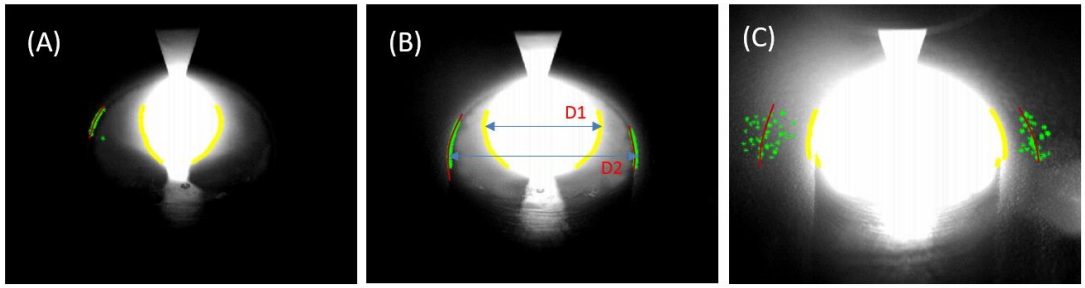

Figure 28. Landmarks detection under three exposure condition. (a) Under exposed image; (b) right exposed image; (c) over exposed image

In the right exposure condition shown in Figure 28(B), the green landmarks were detected on the weld pool side edge. For the over exposure image shown in Figure 28(C), the saturated arc light covered the side edge. And the green landmarks were randomly distributed outside the weld pool area. To improve the accuracy of landmarks detection, a support vector machine classification model was trained to determine the exposure conditions into under exposed, right exposed and over exposed condition. The camera exposure time in the following capture period will be adaptively adjusted to keep it in appropriate exposure condition.

In the linear SVM classification problem, a hyper plane was found that separates the data with maximal margin [94, 95]. Given training vectors $x_i \in R^n$, i =1,...,m, where n is the number of feature and m is the number of training data. The label vector $y \in I$ such and $y_i \in [1,3]$, SVM determines the hyperplane by solving the following optimization problem.

$$\min_{\omega,b,\xi} \quad \frac{1}{2}\omega^T\omega + C\sum_{i=1}^{l}\xi_i$$
$$s.t. \quad \begin{cases} y_i\left(\omega^T x_i + \omega_0\right) \geq 1-\xi_i, \\ \xi_i \geq 0, i=1,\ldots,l, \end{cases} \tag{4-1}$$

Where ω is a weight vector, ω_0 is the threshold, and C>0 is a cost coefficient, which represents a balance between the model complexity and the approximation error. When the constraint conditions are infeasible, slack variables ξ_i is introduced[96, 97].

As shown in Table 2, nine features were extracted for the detected landmarks and the original image. Two polynomial curve fitting were applied on the green landmarks as reference. Feature 6 & 7 was the sum of squared errors (SSR) of curve fitting. Feature 8 & 9 are the standard deviation of the green landmarks location in y direction.

The training database uses 120 weld pool images, including 30% insufficient exposure images, 30% over exposure image and 40% complete exposure images. The SVM provides a good generalization for this pattern classification problems. The accuracy of the classification model was 98.6% through 5-folds cross validation.

Table 2. Extracted features from detected landmarks

No	Features description
1	Average intensity of the image
2	Number of green landmarks on left edge
3	Number of green landmarks on right edge
4	D1: width of the saturated area
5	D2: maximum distance between two fitted curves
6	SSR of the curve fitting on left edge
7	SSR of the curve fitting on right edge
8	STD of green landmarks on left edge in y direction
9	STD of green landmarks on right edge in y direction

4.3.4 Experiment validation

Two bead-on-plate autogenous welds were performed on the 6mm thick SS304 plate. The welding current changed between 100A, 120A and 150A during one weld. The welding voltage was controlled at 11V through arc voltage control system. Welding speed was 2mm/s. Argon shielding gas flow rate was set at 20 CFH. As shown in Figure 29(A-C), the weld pool images of the first weld were obtained under constant exposure time at 750 μs. However, the arc light overwhelmed the weld pool area when the welding current is 100A and 120A. The weld pool boundary can be observed as the current went up to 150A. Thus, a constant camera exposure time may not able to obtain high quality weld pool images when the welding current is changed during the weld.

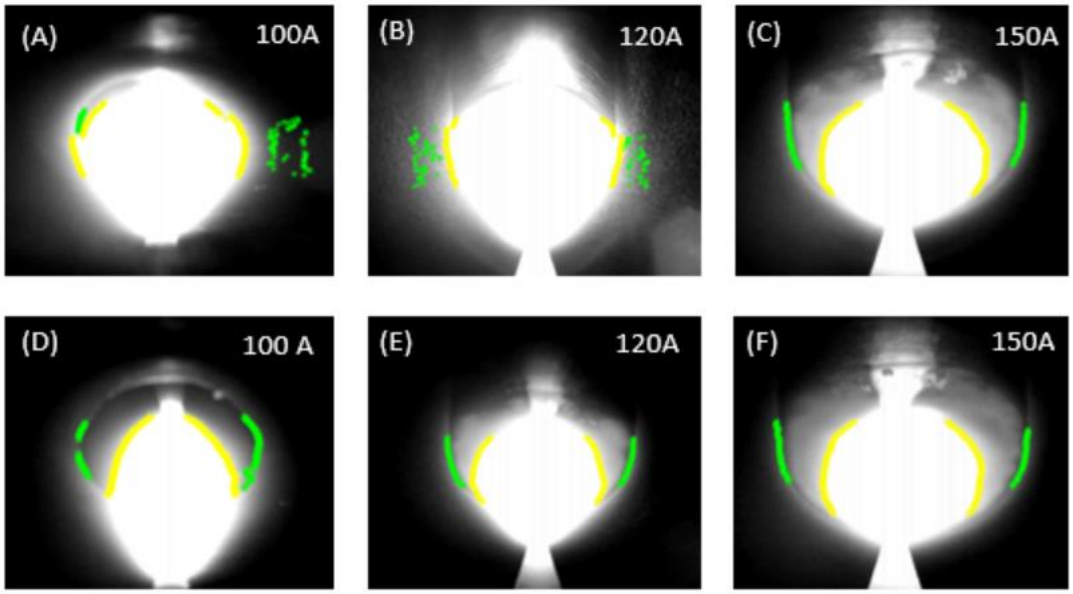

Figure 29. (a-c) Landmarks detection on the weld pool image obtained with constant exposure time for experiment 1-3; (d-e) landmarks detection on the weld pool image obtained adaptive controlled exposure time for experiment 1-3

A second weld was performed with same welding parameters as first one. However, the adaptive exposure control algorithm was applied during the weld. The weld pool images and the detected landmarks were shown in Figure 29(D-F). The exposure time was increased with the increase of weld pool area because more illumination is required to extract whole weld pool boundary. The green marks were detected on the side edge for all the three current. Hence, the weld pool images with appropriate exposure condition were obtained using the proposed algorithm. The weld pool boundary can be further extracted based on the green landmarks.

4.5 Monitoring Weld Pool Surface from Reversed Electrode Image

The surface height (SH) of weld pool top surface provides important information about the state of weld penetration during welding. In this section, a new method was developed to calculate weld pool surface height (SH) based on the reversed electrode image (REI) reflected on the weld pool surface. Due to the specular reflection of the weld pool top surface, REI is visible on the weld pool surface during GTAW. The position of the REI was determined with a robust image processing algorithm. Based on the principle of light reflection, the distance (DERI) between the electrode tip and the REI was related to the SH. By assuming the weld pool surface as a spherical mirror, a reflection model was established to calculate the SH based on the measurement of DERI, arc length and weld pool geometry. This method was verified with bead-on-plate welding experiments. The calculated SH index was found positively related to the face reinforcement or depression of the weld bead. The section 4.5 is written based on a paper published by Zongyao Chen, Jian Chen and Zhili Feng. Monitoring weld pool surface and penetration using reversed

electrode images. Welding Journal 96, no. 10 (2017). My contributions to the publication include (1) establish the hardware system, (2) design and conduct the experiments, (3) develop the image processing algorithm, (4) process the data analysis the experiment result.

4.5.1 Acquisition of reversed electrode image during GTAW

The schematic to acquire REI is shown in Figure 30. Considering weld pool top surface as a spherical surface mirror, a virtual reversed image of the tungsten tip is formulated on the other side of the weld pool due to specular reflection on the weld pool surface. Based on the pin-hole camera model, both image of electrode and the REI are visible from the camera with an adequate camera posture as shown in Figure 30.

The weld pool surface height is defined as the vertical distance from the vertex of the weld pool surface to the work piece. The distance (DERI) between the electrode tip and the reverse image is defined as,

$$DERI=D0+D1 \tag{4-2}$$

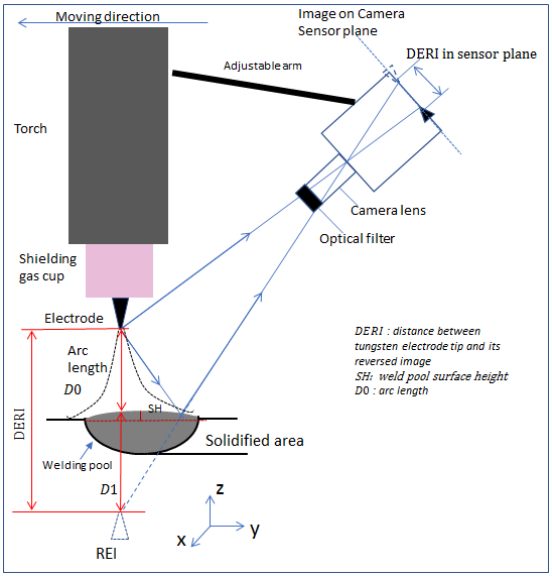

Figure 30. Diagram of acquire REI from rear view camera

Object distance, D0, is equal to the arc length during welding. As mentioned in previous research [85, 98] , the arc length is defined as the distance from the tip of the welding electrode to the adjacent surface of the weld pool. The image distance, D1, is the distance from REI to the weld pool surface, which is related to the shape of the weld pool surface.

4.5.2 Reflection model of weld pool surface

In this research, the sphere shape model was used to describe weld pool top surface. The reflection diagram of two types of spherical weld pool surface is shown in Figure 31. In Eq. 4.3, R is the radius of the sphere; d is the total length of the partial sphere which equals to the width of weld pool. Thus, SH is calculated as follows,

$$(R)^2=(R+SH)^2+(\mathrm{d}/2)^2 \tag{4-3}$$

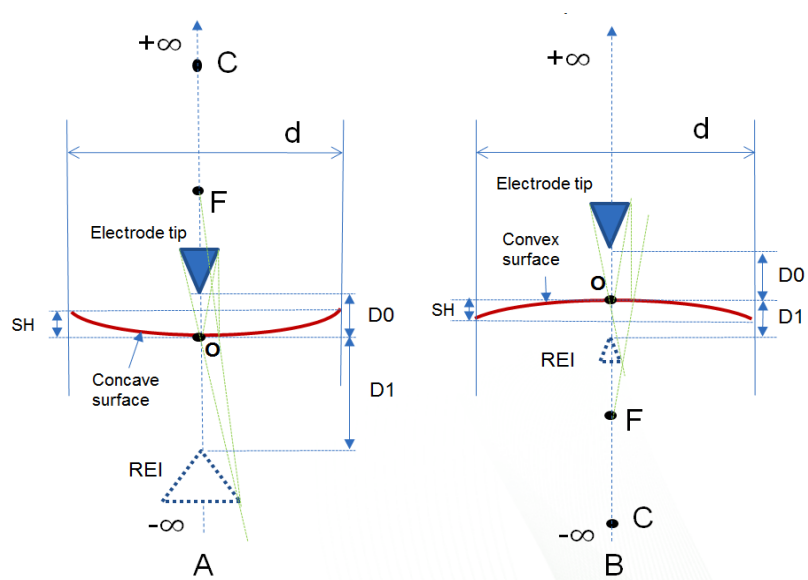

Figure 31. (a) Reflection diagram of concave weld pool surface; (b) reflection diagram of convex weld pool surface

In Figure 31, O is the vertex point on the spherical surface. Point C is the center of curvature, where OC=R. F is the focal point of the curved mirror. The distance between OF is the focal length, f ,which is equal to R/2. The concave weld pool has positive SH and the convex one has negative SH.

Based on the reflection law, the virtual image is formed in the opposite side of the mirror since the object distance D0 is smaller than the focus length f. The mirror equation describes the relationship between the object distance, D0, and the image distance, D1 as follows,

$$\frac{1}{f} = \frac{1}{D0} + \frac{1}{D1} \tag{4-4}$$

The object distance, D0, is less than the absolute value of image distance |D1| in the concave surface (SH<0 and F>0) in Figure 31A. A magnified REI is formed on the other side of the weld pool surface. For the convex surface in Figure 31B, a focused REI was formulated on the other side of the weld pool. The object distance D0 is larger than image distance|D1|. When the SH=0, weld pool surface is a flat mirror, D0 equals to |D1|. The REI image with same size as the electrode tip is formed.

In the proposed reflection model, the DERI is determined by the height, weld pool width and arc length. In Figure 32, the simulation curve described the relationship between DERI and SH. Figure 32A shows DERI is monotonically decreasing with the weld pool SH at constant arc length (D0=4.5mm) and weld pool width (d=10mm). In Figure 32B, the arc length is the only constant variable(D0=4.5mm), and the 3D surface plot describes the relationship among DERI, weld pool SH and weld pool width. The trend of the plot shows that the increasing of the SH causes the decrease of DERI.

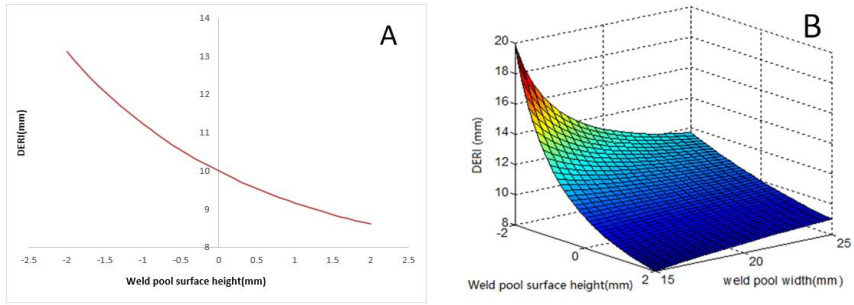

Figure 32. (a) DERI vs SH; (b) 3D surface plot of DERI vs SH and weld pool width

4.5.3 Algorithm of weld pool surface height calculation

The procedure of SH calculation is presented in Figure 33. Camera calibration is performed to identify the camera parameters before welding experiments. The position of REI was automatically extracted from the image obtained using designed image processing algorithm in real time, and the DERI in real object coordinate system is further calculated. Meanwhile, the arc length was determined from the arc voltage. With the measurement of weld pool width from passive vision image, the index of SH was calculated based on the proposed reflection model. The location of electrode tip Z_A is fixed because the camera is mounted on the moving welding torch. It is challenging to track the location of REI (Z_B) in the passive vision image, due to the disturbance of droplet and arc as shown in Figure 34(A). The algorithm was developed to automatically extract Z_B location and compute DERIs from the image sequence based on ROI method. The region of interest (ROI) was first identified from the binary image shown in Figure 34(B). Then a second search was conducted inside ROI to find the location of REI. Based on the proposed algorithm, DERIs can be calculated in real time with the error range within ± 2 pixel.

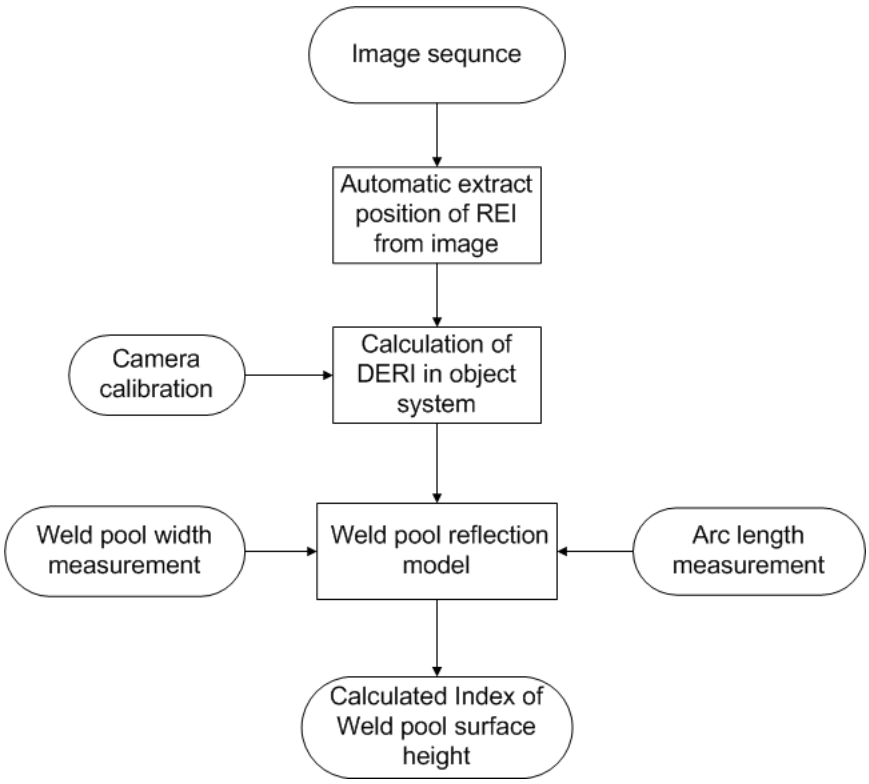

Figure 33. Flow chart of SH calculation

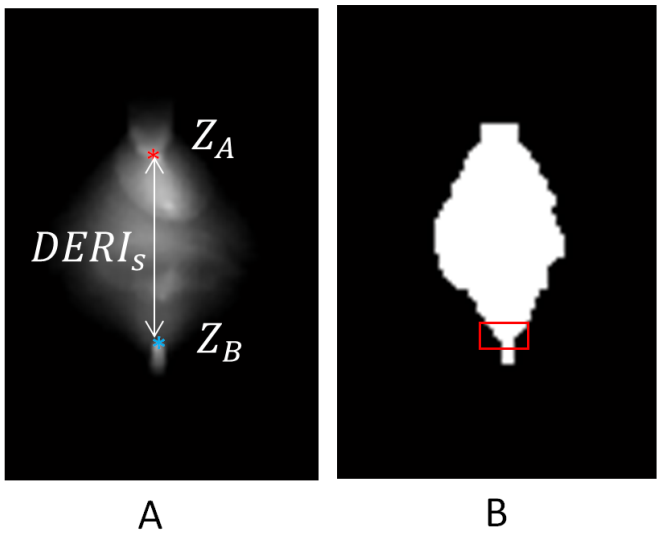

Figure 34. (a) Finding REI location in under exposed image; (b) image binarization and window search

4.5.4 Experimental validation of SH measurement

The experiment setup of the weld pool surface monitoring system is same as we describe in Figure 23. To validate the proposed method to calculate SH, bead-on-plate welding experiments were conducted on SS304 workpiece with uniform thickness from experiment 1 to experiment 4. The work piece was clamped tightly before welding. The welding parameters are shown in Table 3. All the welds were conducted at a constant current and welding speed. Experiment 1 and 2 were conducted on 3mm-thick stainless-steel workpiece with the same welding current and welding voltage. Welding speed of experiment 1 is much lower than that of experiment 2. The experiment 3 and 4 were conducted on the 6mm-thick SS304 workpiece. Experiment 3 was conducted with filler wire to increase the convexity of weld pool surface.

The weld bead cross-section view of cases 1-4 are shown in Figure 35. In case 1, a full penetration weld was produced on the 3mm-thick plate. A concave shaped weld bead was made on the workpiece. The depression of the weld bead was to -1.1mm. In case 2, a partial penetrated weld was produced on the same plate by increasing the travel speed. In case 3, a convex weld bead was created on the 6mm-thick workpiece with filer wire at 25 inch/mm, the face reinforcement measured from cross-section view was 1.2mm. The face reinforcement of the weld bead in case 2 and case 4 were close to zero.

Table 3. Welding parameters of surface height measurement

Number of experiment	Material	Thickness	Current	Travel speed	Voltage	Wire feed rate
1	SS304	3mm	120A	2mm/s	11V	/
2	SS304	3mm	120A	3mm/s	11V	/
3	SS304	6mm	150A	2mm/s	11V	10.6mm/s
4	SS304	6mm	150A	2mm/s	11V	/

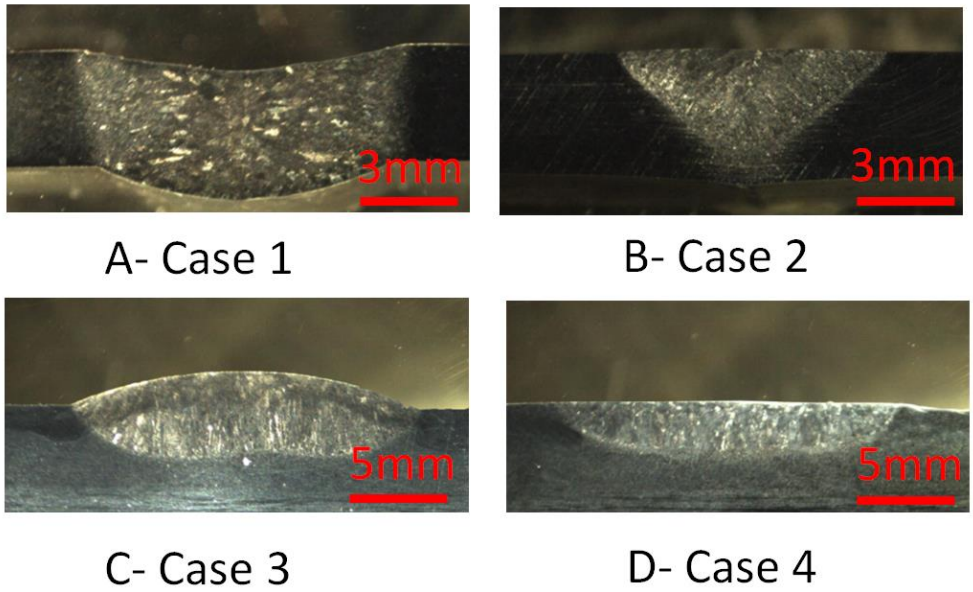

Figure 35. Weld bead cross section view of experiment 1-4

For the case 1-4, DERI were calculated from the REI using the developed method as shown in Figure 36. Once the arc started, the weld torch was automatically raised up in 2 second to maintain the arc length. The DERI continuously increased for the first 10 second until weld pool shape became relatively stabled.

The REI images in Figure 37 were obtained at 20 second when the weld pool became stabled. The REI are symmetrical since the shape of weld pool surface is close to a symmetrical sphere. And the unsymmetrical weld pool surface will cause aberration of the REI image which may affects the measurement of DERI.

From the REI image in Figure 37A-B, the measured DERI was larger in case 1 than that in case 2 due to the decreased weld pool SH. In case 2, the weld pool surface is close to flat when the partial penetrated weld occurred. The weld pool surface was considered as a flat mirror. The size of REI is close to the image of the electrode tip. As the penetration increased in case 1, a concave weld pool surface was formed in case 1. Compared to Figure 37B, the specular weld pool surface served as concave mirror which increased the size of REI image and DERI in Figure 37A.

During case 4, the weld pool surface was considered as a flat surface mirror since the convexity of weld pool was relatively small. In case 3, the convex weld pool with increased convexity was produced with adding filer wire. A small and focused REI image was found In Figure 37C due to the specular reflection on the convex shape weld pool surface. Compared with case 4, the increase of weld pool SH caused the decrease of measured DERI in case 3 as shown in the measured curve in Figure 36.

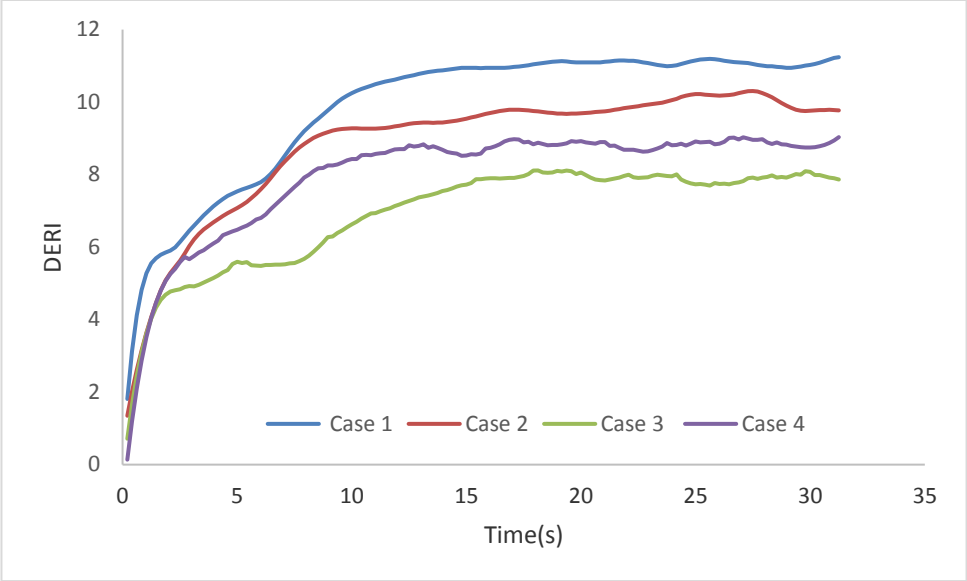

Figure 36. Calculated DERI curve of weld 1-4

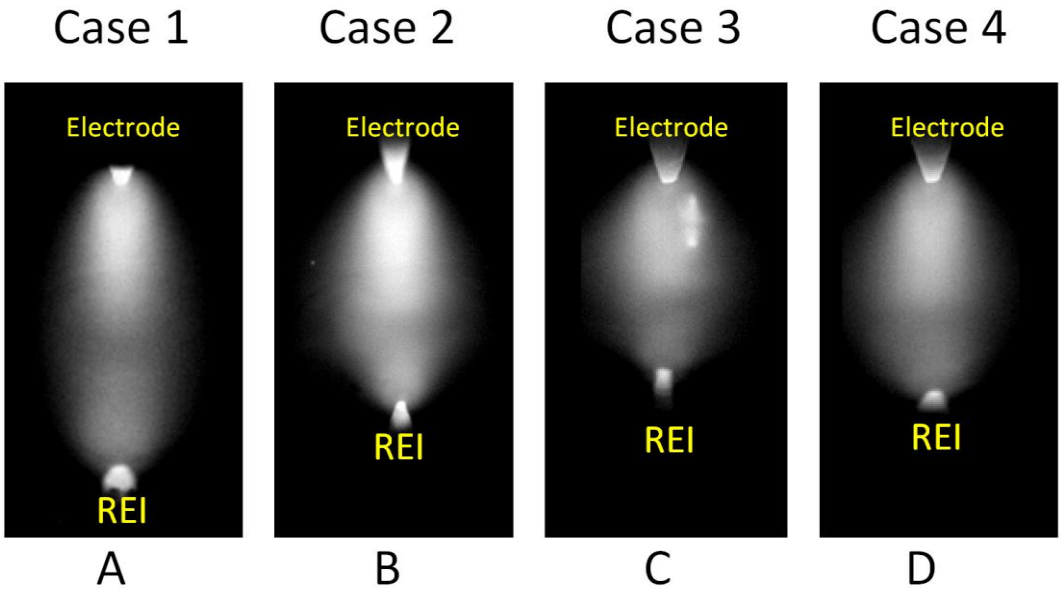

Figure 37. Reversed electrode image of case 1-4 at 20 second after welding started

The changing of arc length was another factor that caused the difference of measured DERI in the four cases. The changing of welding current caused the different arc length, which was 4.5±0.32 mm in cases 1 and 2 and 3.6±0.32 mm in case 3 and 4. Thus, the measured DERI in case 1 and 2 was largely increased than that in case 3 and 4.

Based on the experiment result, we can conclude that DERI decreased with increase of weld pool SH with the same arc length, which is consistent to the simulation results.

In Figure 38, the index of SH was calculated during stable stage from 15s-30s based on the measured variables including DERI, arc length and weld pool width. Consequently, the calculated index of SH was close to the measurement of weld bead from the cross-section view in Figure 35.

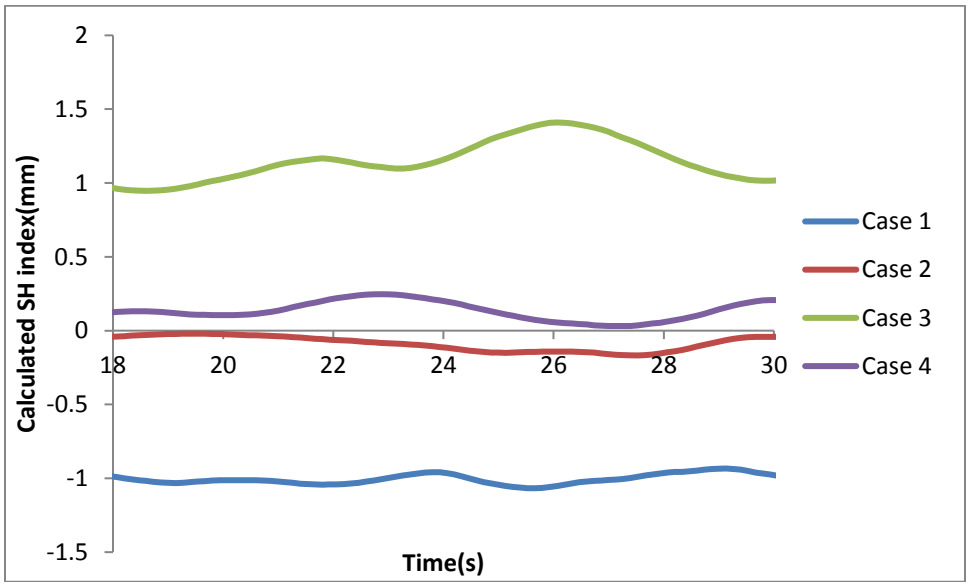

Figure 38. Calculated SH index of experiment case 1-4

4.6 Validation of 3D Weld Pool Geometry Measurement

The experiment of measuring weld pool geometry was conducted on a wedge shape SS304 plate as shown in Figure 39. The weld current remains constant at 120A. Welding speed was 2mm/s. The thickness of the plate gradually reduced from 6mm to 2mm.

The topside and back view of the weld were shown in Figure 40. The blue arrow bar indicated the time line of the welding process. The weld was started from the 6mm thick end travel to the 2mm thick end. The topside width of weld bead was increased with the decrease of thickness. The weld pool gradually penetrated the plate as the thickness reduced which can be seen from the backside.

In Figure 41,cross-section views of the weld bead were collected at four locations (marked in Figure 40) with different penetration condition: partial, complete and over penetration. Figure 41 (A-B) shows a partial penetrated weld where the fusion did not through the whole material. The face reinforcement of weld bead in is close to zero. Figure 41(C) shows a complete penetrated weld is as the fusion extends completely through the thickness of the material, and a concave weld bead surface was formulated. The concavity of weld bead top surface was increased in Figure 41(D), as the penetration depth increased. This weld can be considered as over penetration since the root reinforcement exceeded the ¼ of material thickness based on the ASME pressure vessel code[1].

Figure 39. Wedge shape SS304 workpiece

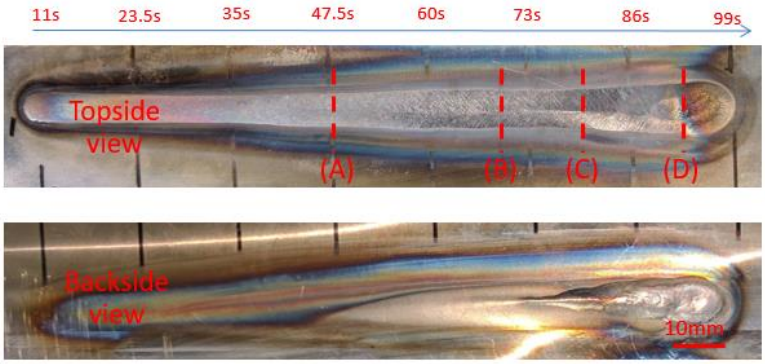

Figure 40. Front view and backside view of weld bead

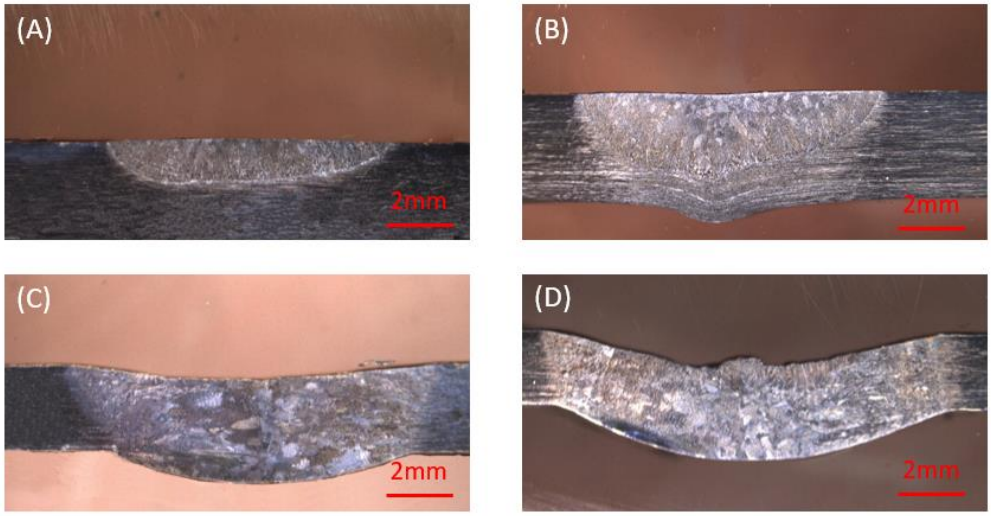

Figure 41. Cross section view of the weld bead

The corresponded REI images obtained with 10 μs were shown in Figure 42 . The image was obtained at 50, 70， 80 and 90 seconds after weld started. As the penetration increased, DERI was extended, and the area of REI increased, resulting from the concavity of the weld pool surface. The concave weld pool surface serves as a concave mirror to generate an amplified REI. The DERI was increased with the increase of weld pool surface concavity.

The corresponded weld pool images obtained at 50, 70,80 and 90 seconds were shown in Figure 43. The weld pool can be visualized with appropriate camera exposure time. The 2D weld pool boundary was fitted using polynomial regression with the detected landmarks. An ellipsoid shape weld pool can be observed from the rear camera as shown in Figure 43(A-B) The weld pool area was increased with the increase of weld penetration. A tear drop shape weld pool was formulated at full penetration in Figure 43(C) and (D).

The distortion of workpiece was more likely to be created at the end of the weld as the workpiece thickness is reduced. Due to the workpiece distortion, the unsymmetrical weld pool shape in Figure 43(D) was observed. Thus, a good clamping is required to further reduce this effect.

The weld pool width can be calculated in real time with the proposed algorithm. The algorithm was implemented using MATLAB. The image processing time to extract REI took less than 10ms per frame. And time consumption for weld pool edge detection was between 20-50ms. The overall time consumption for each period of measurement was below 100ms which can be applied in real time. Figure 44 shows the calculated result of weld pool width w_t and trailing length L_t based on the weld pool edge detection algorithm. The green dots indicate bead width measured after welding.

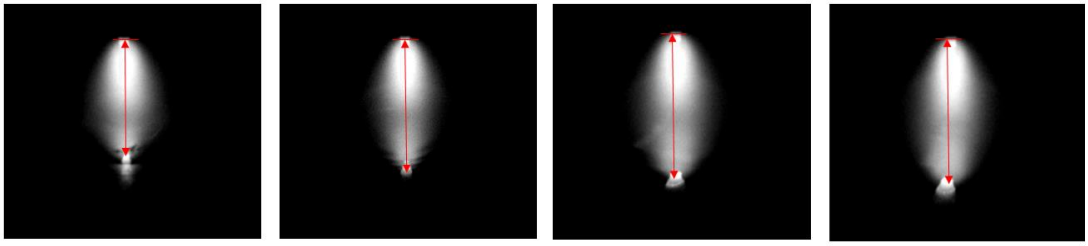

(A) (B) (C) (D)

Figure 42. Comparison of DERI from image type I

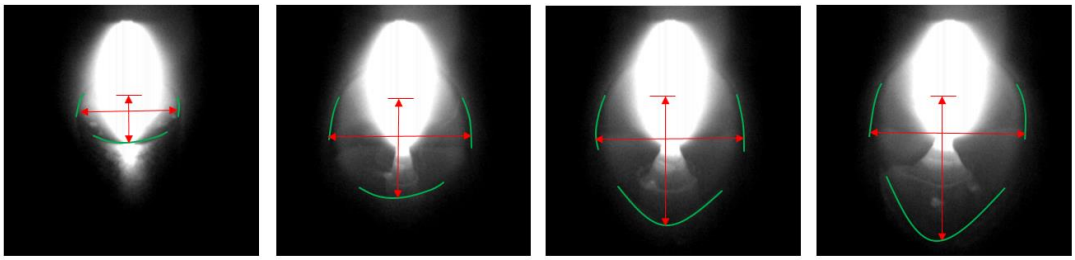

(A) (B) (C) (D)

Figure 43. Weld pool edge detection from image type II

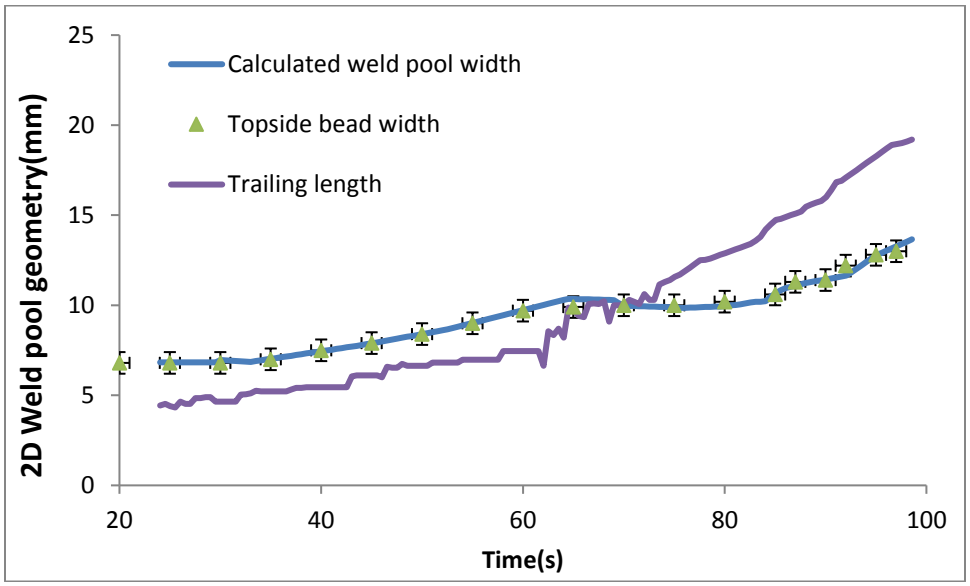

Figure 44. 2D geometry measurement of topside weld pool

The calculated weld pool width is coherent with the bead width on the top side of the workpiece. The mean square error (MSE) between the calculated weld pool width and weld bead width is 0.12mm. From the curve in Figure 44, the increasing rate of w_t was slow down as the weld close to complete penetration. The weld pool trailing length continuously increased and exceeded the width of weld pool as the complete penetration occurs. Meanwhile, the weld pool area changed from an ellipsoid shape to a long tear drop shape with small rear angle.

In Figure 45, the weld pool surface height was calculated using REI method. The red dot around the curve was the face reinforcement of the weld bead. The calculated SH was close to the measurement of face reinforcement. The standard deviation between the calculated SH and weld bead face reinforcement was 0.25. The decreasing rate significantly increased as the weld became over penetrated. Surface tension becomes the major force to support the weld pool from burning through. The concavity of weld pool top surface increased due to the gravity.

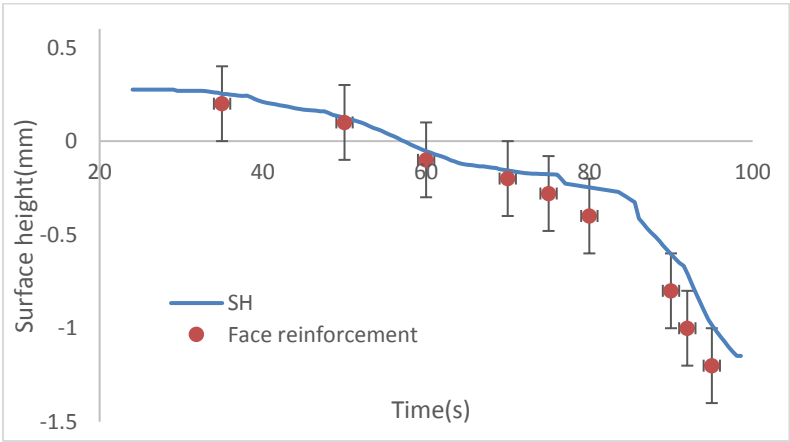

Figure 45. Measurement of weld pool surface height

4.7. Conclusion

In this paper, new image processing method based on adaptive passive vision image was developed to measure weld pool 3D geometry. Based on the result from experiment, the conclusions can be drawn as follows,

The SVM classification model can determine the exposure condition of weld pool image with sufficient accuracy. The camera exposure time was adaptively adjusted to obtain weld pool image in right exposure condition. This method increased the robustness and accuracy of the weld pool edge detection. The weld pool surface height can be calculated based on the measurement of DERI, arc length and weld pool width. Three-dimensional weld pool geometry was measured in real time welding condition. The calculated 3D weld pool surface geometry from the proposed algorithm was close to the actual weld bead size. The measured 3D weld pool surface geometry was closely related to the weld penetration.

CHAPTER V
PENETRATION PREDICTION WITH MACHINE LEARNING MODELS

The backside width can be used as the major variable to identify the penetration status of the weld. However, measuring backside width of the weld usually require sensor on the back of the weldment which is not practical in many welding applications. In manual welding process, the geometry of weld pool top surface geometry is a major reference for welder to determine the penetration condition. This chapter focuses on establishing an artificial intelligent model to predict penetration.

Based on the method discussed in previous chapter, multiple features can be extracted from the weld pool images. Some important features including weld pool width, weld pool trailing length and the surface height was measured during bead on plate autogenous GTAW. These features can be used as the input for the data driven model[99].

Supervised machine learning method: linear regression, artificial neural network (ANN) , bagging trees were tested on the database. Through feature importance analysis, we found out that the weld pool width, trailing length and surface height (SH) played the major role to predict backside width. The performance of prediction was further improved through feature selection. Finally, the trained model was validated with butt joint welding experiments with satisfactory accuracy. The proposed method can be further applied to build real time close-loop penetration control system. The chapter is mainly based on the paper published by Chen, Zongyao, Jian Chen, and Zhili Feng. Welding penetration prediction with passive vision system. Journal of Manufacturing Processes 36 (2018): 224-230. My contributions to the paper include (1) establish the hardware system, (2) design

and conduct the experiments, (3) develop the image processing algorithm, (4) process the data analysis the experiment result.

5.1 Definition of Welding Penetration

The welding penetration can be determined by measuring the root reinforcement on the backside of the weld. For incomplete penetration condition, the weld metal does not extend through joint thickness, and the backside width and the depth of root reinforcement is zero.

According to the ASME Boiler and pressure vessel code[79][1], to conduct a full penetration weld, the backside width of the weld should be above the width of the root gap. And the root reinforcement must be lower than the maximum to avoid over penetration.

In this research, most of the weld was conducted on the plate or butt joint with no gap. The root gap is close to zero. We classified the penetration into four categories based on the weld pool backside width W_b. Incomplete penetration, $W_b = 0$; critical penetration, $0 < W_b < 2mm$; complete penetration, $2mm < W_b < 8mm$; over penetration, $W_b > 8mm$.

In this section, the study focuses on the bead on plate welding under low current (<200A) and low speed (1.5-3mm/s) level. Under this condition, the depression due to arc plasma force is insignificant. Previous numerical studies of weld pool behaviors indicated that weld pool surface shape is an important characteristic that associated with welding penetration [91, 100, 101]. As shown in Figure 46, the weld pool surface gradually changed from convex shape to concave shape as the penetration depth increased.

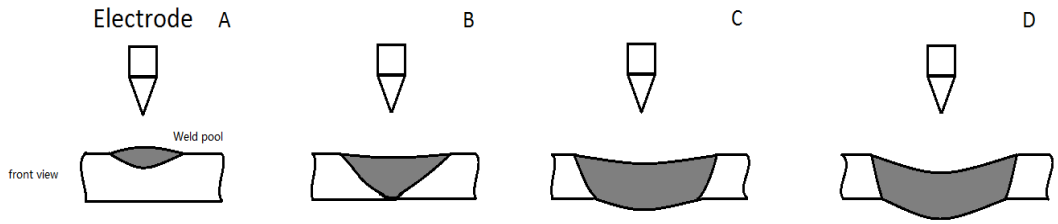

Figure 46. Weld pool surface shape weld in four penetration state during autogenous GTAW. (a) Partial penetration; (b) critical penetration; (c) full penetration; (d) over penetration

During partial penetration state, the weld pool surface is convex due to the expansion of liquid metal. The critical penetration is the transition state from partial penetration to full penetration, when the bottom surface of weld pool started to form on the backside of the workpiece.

For the fully penetrated weld, the area of weld pool bottom surface is increased, and the surface tension becomes the major force to support the liquid metal.

Therefore, the gravity force forms a concave shape top surface of weld pool. The depression of the weld pool surface is further increased at the over penetration state as shown in Figure 46D. For filler wire welding, the volume of liquid weld pool increases. Convexity of the weld pool surface for partial penetrated weld can be further increased. And depression of the weld pool surface in full penetrated weld can be reduced. The wire feed speed can be another factor changes the surface height during welding.

5.2 Data Collection

Welding penetration is affected by such welding parameters as welding current, welding voltage, arc length, gas flow rate, workpiece thickness, which should be wisely selected to cover a wide range of welding conditions for building the regression model. In this paper, the welding voltage is set constantly at 11 V by arc voltage control unit during

the experiments, and argon shielding gas flow rate was set at 30 CFH. The training data includes 1423 instances obtained from 12 trails of weld with different parameters. The range of the welding parameters is shown in Table 4. For each dataset, 8 input features, as shown in

Table 5, were used and the predicted output is backside width w'_b .

5.3 Evaluation Criteria

The performance of regression model is evaluated by root mean square error (RSME), mean absolute error (MAE) and R^2.

The RSME and MAE calculate the difference between the predicted value w'_b and the real back side width w_b. The equation to calculate RSME is given by

$$\text{RSME} = \sqrt{\frac{\sum_{i=1}^{n}(w'_b\,(i)-w_b(i))^2}{n}} \tag{5-1}$$

The mean absolute error (MAE) errors are defined as follows,

$$MAE = \sum_{i=1}^{n} |w'_b(i) - w_b(i)|/_m \tag{5-2}$$

The calculation of R^2 is shown as follows,

$$R^2 = 1 - \frac{\sum_{i=1}^{n}(w_b(i)-\bar{w}_b)^2}{\sum_{i=1}^{n}(w'_b(i)-\bar{w}_b)^2} \tag{5-3}$$

$\bar{w}_b$ is the mean of the target data w_b, i is the index of the dataset, n is the total number of instances. The RSME and MAE indicate the accuracy of the regression model. A high RSME or MAE value means the model may suffer from under fitting or the features in the regression model is insufficient to predict the backside width. R^2, indicated how

well the variables in the selected features subset are correlated to the target.

Table 4. Welding parameters range of training database

Current	100-150 A
Welding speed	1~2 mm/s
Thickness	2~6 mm
Argon flow rate	30 CFH
Arc length	3.6~5.1 mm
Arc voltage	11 $\pm$0.2 V

Table 5. Description of Input features

Abbreviation	Description
I	Welding current
w_t	topside weld pool width
L_t	weld pool trailing length
DERI	distance between electrode and the REI
D0	Arc length
SH	Weld pool surface height
V	Welding speed
R	Ratio between weld pool width and length

5.4 Linear Regression for Penetration Prediction

5.4.1 Linear regression model

The linear regression is one of the commonly used supervised learning models. In previous research, the 3D weld pool geometry characters was used to predict weld penetration by applying least square fitting on a linear model.

The linear model to estimate backside width $\widehat{W_b}(i)$ takes the form as follows,

$$\widehat{W_b}(i) = \theta_0 + \sum_{j=1}^{p} \theta_j x_j(i) \tag{5-4}$$

Where p is the total number of the input features, i is the index of the dataset, and θ are the coefficient of the linear model. The coefficient of model is determined by minimizing the cost function given as follows,

$$J(\theta) = \frac{1}{2}\sum_{i=1}^{m}[\sum_{j=0}^{n} \theta_j x_j(i) - W_b(i)]^2 \tag{5-5}$$

Where m is the total number of the datasets, and $x_0 = 1$.

The value of the θ which minimizes the cost function can be calculated by the normal equation:

$$\theta = (X^T X)^{-1} X^T W_b \tag{5-6}$$

Where $X = \begin{bmatrix} 1 & x_{11} & \cdots & x_{1p} \\ \vdots & \vdots & \ddots & \vdots \\ 1 & x_{n1} & \cdots & x_{np} \end{bmatrix}$

The calculation of the criteria to evaluate the estimation is show as follows,

The performance of the linear regression model can be evaluated by RSME, MAE and R square which are described in section 5.3.

5.4.2 Feature selection

All the 8 features can be used to build the prediction model. However, some of the variables may not correlate with penetration. Sequential forward feature selection (SFS) helps to identify the useful variables in the model. The procedure of SFS is described in

algorithm 3,

Algorithm 3 Sequential forward feature selection
Input: Database with 8 features **Output**: Selected feature subset 1. Conduct 5 folds cross validation using one feature. Find the feature {x}which produce the best prediction accuracy. Using feature {x} as the initial subset. 2. K is the number of features in the current subset. Sequentially add the other feature into the subset and conduct 5 folds cross validation test on the dataset. 3. Find the optimal feature subset with k+1 features which provide best accuracy for the feature subset. 4. If the accuracy of using feature subset with k+1 features is better than all feature subset with k features, then k=k+1, go back to step2; If not, the kth feature subset become the final output.

33 features subset were tested based on SFS method. The performance of 33 feature subsets is shown in Table 6. The bold values indicated the feature subset which has the best performance among the feature subsets with same number of features. For example, the first 8 subsets shown in top four rows of the table contains only one feature. The subset with L_t has the highest R-square value and the lowest RMSE and MAE errors. Thus, it was selected as a permanent feature. The 7 features leftover were sequentially combined with Lt to create new subset with 2 features shown in row 5. And the feature subset with w_t and L_t has the best performance among all the feature subset with 2 features.

SFS determined the optimal feature subset of five features including weld pool width, training length, DERI, SH and travel speed. And the performance of the feature subsets with 6 features did not improve the prediction. The remaining features such as current, arc length and ratio are less important variables. The expression of the final linear regression model is calculated as follows,

$$w'_b(i) = -0.329 + 0.255 * w_t + 0.659 * \boldsymbol{L_t} - 0.3*\text{DERI} - 1.71*\text{SH} - 1.764*\text{v} \qquad (5\text{-}7)$$

The RSME of the final linear regression model is 1.669, and 1.33 for MAE. The highest R-square value was 0.86 which is the best result with linear regression model.

Table 6. Result of the sequential forward feature selection

Feature subset	I	w_t	**L_t**	DERI	D0	SH	v	R
RMSE	4.29	2.87	**2.04**	3.79	4.3	2.64	3.91	4.07
R^2	0.08	0.59	**0.79**	0.28	0.08	0.65	0.24	0.17
MAE	3.64	2.33	**1.639**	3.3	3.65	2.17	3.52	3.3
Feature subset	I, L_t	**w_t, L_t**		DERI , L_t	D0, L_t	SH, L_t	V, L_t	R, L_t
RMSE	2.87	**1.75**	/	1.995	2.006	1.91	1.86	1.85
R^2	0.59	**0.85**	/	0.8	0.8	0.82	0.83	0.83
MAE	2.3	**1.38**	/	1.65	1.63	1.56	1.51	1.43
Feature subset	I, w_t, L_t			DERI, w_t, L_t	D0, w_t, L_t	SH, w_t, L_t	**v, w_t, L_t**	R, w_t, L_t
RMSE	1.75	/	/	1.73	1.755	1.754	**1.71**	1.759
R^2	0.85	/	/	0.85	0.85	0.85	**0.85**	0.85
MAE	1.38	/	/	1.37	1.3804	1.38	**1.34**	1.38
Feature subset	I, v, w_t, L_t			**DERI, v, L_t, w_t**	D0, v, w_t, L_t	SH, v, w_t, L_t		R, v, w_t, L_t
RMSE	1.71	/	/	**1.69**	1.71	1.7	/	1.71
R^2	0.85	/	/	**0.86**	0.85	0.85	/	0.85
MAE	1.35	/	/	**1.347**	1.35	1.34	/	1.35
Feature subset	DERI, v, w_t, L_t,I				DERI, v, w_t, L_t,D0	**DERI, v, w_t, L_t,SH**		DERI, v, w_t, L_t,R
RMSE	1.695	/	/	/	1.695	**1.66**	/	1.698
R^2	0.86	/	/	/	0.86	**0.86**	/	0.86
MAE	1.35	/	/	/	1.35	**1.33**	/	1.35
Feature subset	DERI, v, w_t, L_t,SH, I				DERI, v, w_t, L_t,SH, D0			DERI, v, w_t, L_t,SH, R
RMSE	1.67	/	/	/	1.669	/	/	1.677
R^2	0.86	/	/	/	0.86	/	/	0.86
MAE	1.336	/	/	/	1.337	/	/	1.33

5.5 Penetration Prediction using Artificial Neural Network

The linear regression provides approximate prediction of BW. However, the welding process is a nonlinear dynamic process. The linear model has the limitation to predict the penetration with certain accuracy. In this section, the ANN model was applied to establish the non-linear relationship between features and predictor.

The relationship between the measured variable (front side weld pool geometry and welding parameters) and the backside width was established by artificial neural network (ANN) regression model. The structure of ANN is shown in Figure 47. All the eight variables in the input layer include the top side weld pool geometry extracted from the passive vision images and the welding parameters collected from the welding machine.

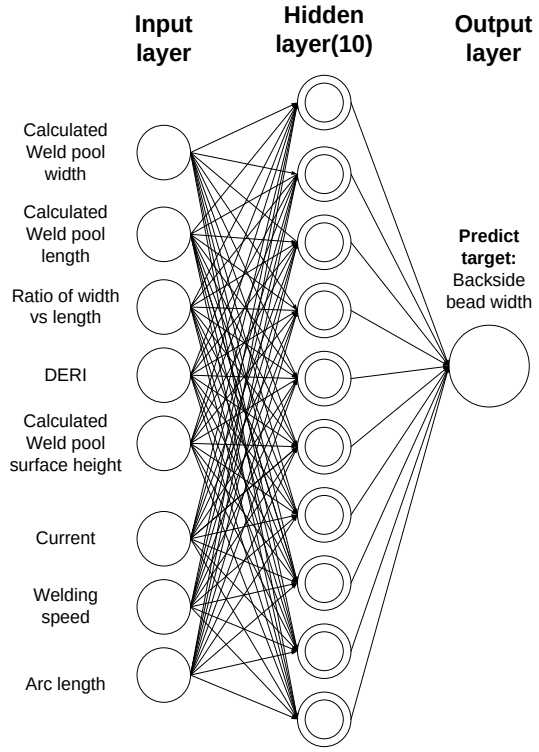

Figure 47. The structure of feedforward neural network for penetration prediction

A standard three layers feedforward neural network is established as shown in Figure 47. The input layer contains 8 features. The first six input features were measured from the weld pool image and current sensor. The weld pool voltage is constant during all the experiments we did. The weld speed and the thickness of material were pre-determined before experiment and was constant for each weld. The number of elements n_2 in hidden layer can be determined based on equation(5-8). where n_1 is the number of the input feature, N is the number of samples, and n_3 is the number of the output layer [102].

$$\frac{N}{10(n_1+n_3)} < n_2 < \frac{N}{5(n_1+n_3)} \tag{5-8}$$

Feature selection is an important procedure to reduce the complexity of the prediction model and running time. Principle component analysis is one of the widely used methods to reduce the dimension of prediction model. Principal component analysis (PCA) can transform the existing features matrix into new sets of orthogonal components through single value decomposition (SVD). In (3), U and V is the orthogonal matrix. The value of the diagonal entries $\sqrt{\lambda_i}$ of Σ indicates the variance of the related component. The first principal component describes the highest variance of the input feature. The importance of succeeding components was reduced. By conducting PCA analysis on the database, the first three components explained 99.6% variance of all input features.

$$M = U\Sigma V^H = [u_0, u_1, \ldots, u_{r-1}] \begin{bmatrix} \sqrt{\lambda_0} & & \\ & \ddots & \\ & & \sqrt{\lambda_{r-1}} \end{bmatrix} \begin{bmatrix} v_0^H \\ v_1^H \\ v_{r-1}^H \end{bmatrix} \tag{5-9}$$

One issue of applying PCA is that its output is not corresponding to the original features. Thus, we may not know the importance of each feature with PCA. An alternative is to apply sequential forward feature selection (SFS) on the existing features.

The performance of the regression model after feature selection is shown in Table

III. The performance of regression was evaluated using 5-fold cross validation. All the datasets were randomly distributed into 5 folds. For each round of test, one-fold was selected for testing and the rest for training. The accuracy was calculated by taking the average of the 5 testing results. The result in Table 7 shows that the feature subset includes weld pool width, weld pool length, surface height and DERI achieved the best accuracy than other combination. And the performance was quite close to that of PCA. This result reflects the fact that the variables relate to the topside weld pool geometry are more important than others.

5.6 Bagging Tree Model Prediction

The bagging trees, also called bootstrap aggregation, is a supervised learning method which can be used in regression and classification. The algorithm is developed based on decision tree, which suffers from high variance also known as over fitting. The bagging trees are built over n_{tree} bootstrap samples $D_n^1, \dots, D_n^{ntree}$ on the training dataset $D_n = \{(x_{1,}w_{b1}), \dots, (x_{n,}w_{bn})\}$. Each tree is fully grown and provides a prediction. The final prediction is calculated based on the average of all predictions. By splitting the training data into several part with bagging, the variance can be reduced [103].

Table 7. Performance evaluation of ANN regression model

Feature selection	Root mean square error(RMSE)
PCA	0.533
$w_f + w_L$	1.235
$w_f + w_L + SH$	0.737
$w_f + w_L + SH + DERI$	0.545
$w_f + w_L + SH + DERI$+current	0.557

Bagging tree method can be used to determine the importance of each variable. The importance of each variable x_j can be calculated as follows,

$$\mathrm{I}(x_j) = \frac{1}{n_{tree}} \sum_{t=1}^{n_{tree}} \left[\frac{1}{|D_n^{tj}|} \sum_{(x_i, w_{bi}) \in D_n^{tj}} (w_{bi} - w'_{bi})^2 - \frac{1}{|D_n^t|} \sum_{(x_i, w_{bi}) \in D_n^t} (w_{bi} - w'_{bi})^2 \right] \tag{5-10}$$

The D_n^t is defined as a collection of out-of-bag samples without permutation of the observed variables. The D_n^{tj} indicate the out of bag samples with permutation of observed j-th variables[104].

The permutation importance of the 8 input features is shown in Figure 48. The three most important variables are weld pool width, trailing length and SH. According to the importance analysis, the key welding parameters such as welding current and welding speed are less important variables in the prediction model. The training database applied here covers wide range of welding conditions. The thickness of material changed from 2mm to 6mm. Thus, the variance of welding current was increased accordingly. If the thickness of material does not change in the experiment database, the weld penetration will be linear correlated with the current.

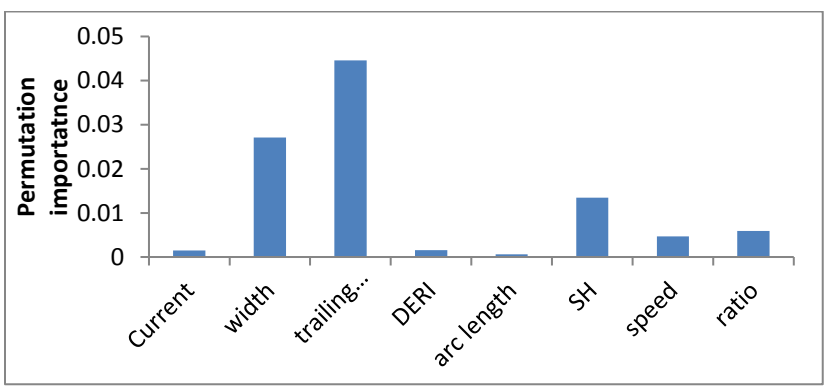

Figure 48. Feature importance analysis

The result shown in Figure 48 indicated the heat input was increased with the increasing of welding current under same welding speed. And the welding penetration was increased linearly with the heat input. However, for the large database with large variation of material thickness and welding speed, the correlation between current and penetration was reduced and even can be neglected. The variables indicate weld pool 3D geometry became the major reference to predict penetration. Further feature selection can be performed based on the importance calculation.

As shown in Table 8, the 8 feature subsets were tested on the training dataset. Based on the importance from high to low, each feature was sequential added into the feature subset and train a new model. The computational expense is less than using SFS method. The training and testing were conducted with 5 folds cross-validation. The model includes 100 trees. The performance of prediction significantly increased as the number of variables increased from one to five. The performance improvement is less significant when the current and DERI were added into the model.

Table 8. Performance of predication with bagging tree

Feature subsets	Root mean square error(RMSE)	R-square	MAE
L_t	1.72	0.85	1.08
$w_t + L_t$	0.91	0.96	0.505
$w_t + L_t + SH$	0.81	0.97	0.454
$w_t + L_t + SH + ratio$	0.751	0.97	0.378
$w_t + L_t + SH + ratio$+speed	0.696	0.98	0.334
$w_t + L_t + SH + ratio$+speed+current	0.659	0.98	0.311
$w_t + L_t + SH + ratio$+speed+DERI+current	0.635	0.98	0.286
All 8 features	0.645	0.98	0.29

This result reflects that the variables relate to the topside weld pool geometry are more important than others. The best performance model contains 7 features. The minimum RSME was reduced to 0.659. And R^2 was increased to 0.98, which means the response has been well explained by the input variables.

5.7 Penetration Prediction on Butt Joint Welding

To verify the performance of the prediction model in real welding condition, a new welding experiment were conducted on the butt joint weldment with zero gap. The weld was conducted on 3 mm thick SS304 plate with 2 mm/s travel speed. The welding current changes from 100 A to 125 A. The topside and backside view of the weld are shown in Figure 49. A partially penetrated weld was formulated in the first 65 mm of the weld with 100 A current. Then, the weld changed to full penetration as the current increases to 125 A.

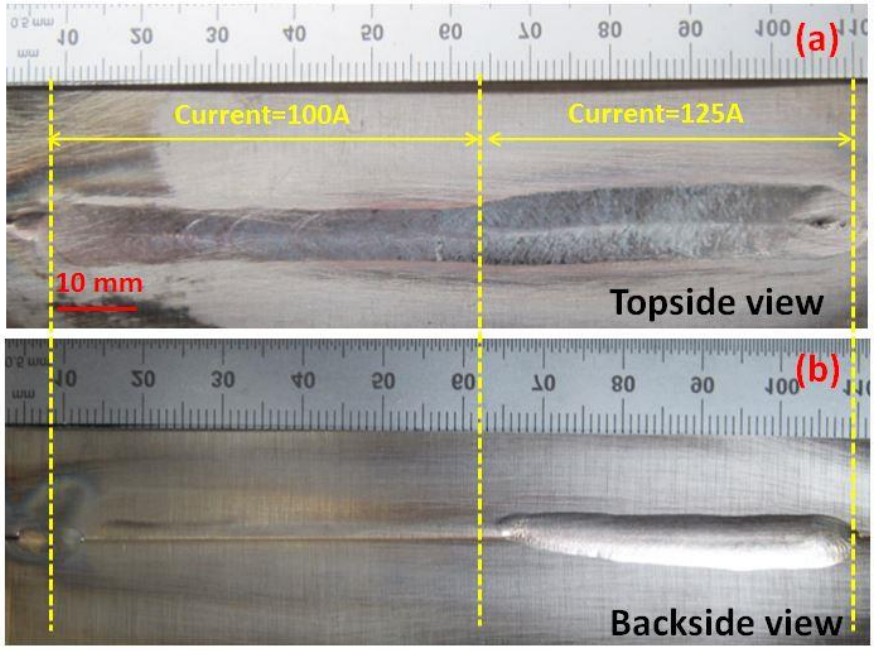

Figure 49. A-Topside view of weld bead; B-Back side view of weld bead

The weld images were obtained and processed in real time. It took less than 200 ms in MATLAB to calculate weld pool surface geometry from passive vision image and less than 100 ms to predict backside width. The passive vision images of partial penetrated weld under 100 A welding current are shown in Figure 50(a)(b). The images of full penetrated weld under 125 A welding current are shown in Figure 50(c)(d). It was found that the weld pool geometry was significantly increased with the increase of welding current. The length of DERI observed from short exposed image in Figure 50(c) was extended compare to Figure 50(a) due to the formulation of complete penetration.

In Figure 51, the calculated $\boldsymbol{w_t}$ shown in the blue curve is consistent with the topside weld bead width measured after welding. $\boldsymbol{w_t}$ was increased during complete penetration period. The SH calculated with REI method is shown in Figure 52. The data in the first 20mm will not be counted due to the unstable arc in the beginning of welding. The SH is close to zero during partial penetration period from 20mm to 65mm. A significant decreasing of SH can be found as the complete penetration started after 65mm.

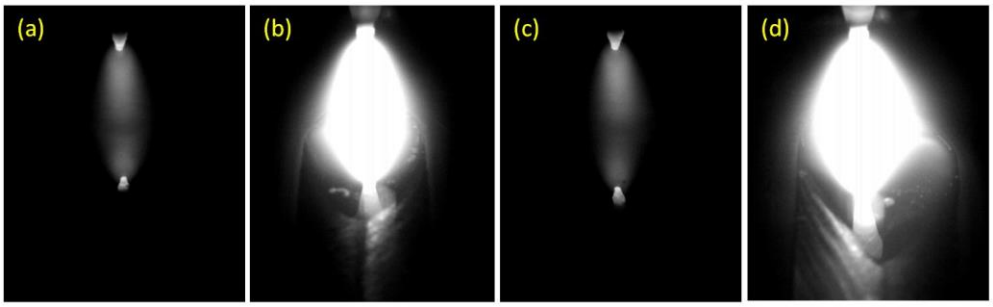

Figure 50. (a) REI of partial penetrated weld; (b) weld pool image of partial penetrated weld; (c) REI of completed penetrated weld; (d) weld pool image of completed penetrated weld

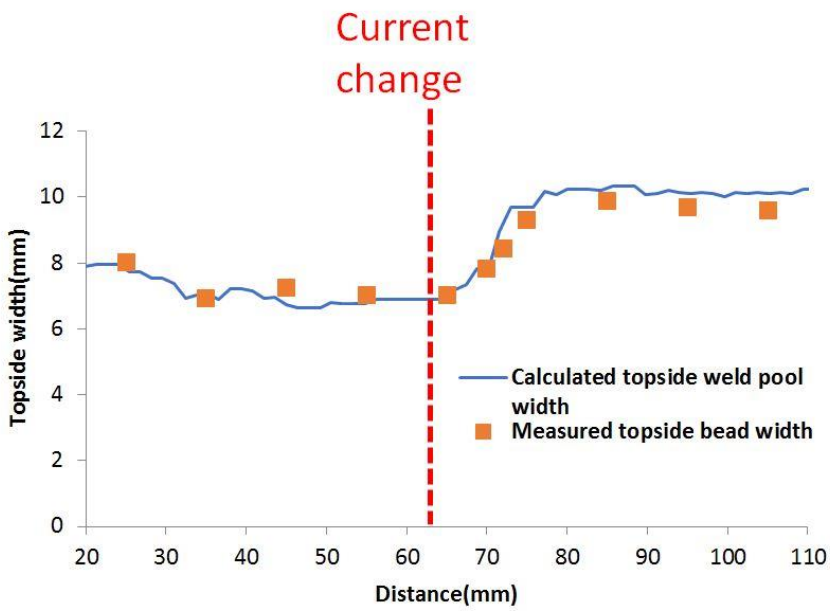

Figure 51. Calculation of weld pool topside width

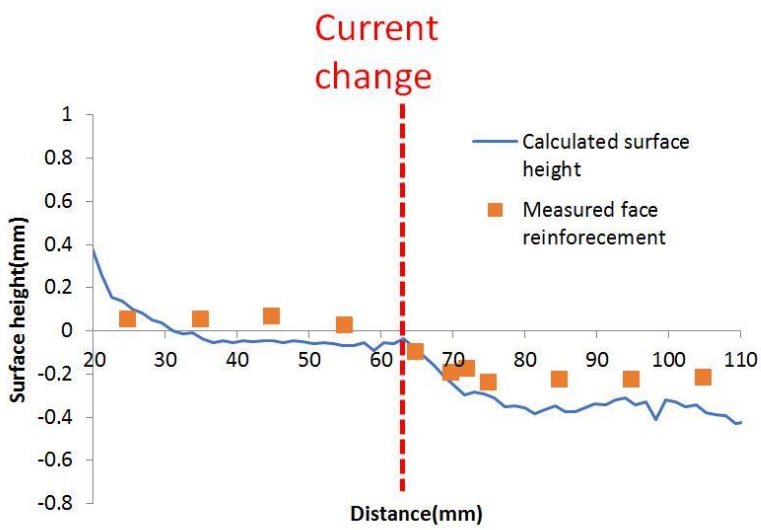

Figure 52. Weld pool surface height calculation

The weld pool backside width was predicted with the proposed machine learning models. The prediction results of linear regression and bagging trees model was shown in

Figure 53. The prediction result using linear regression model has large bias from the real measurement of weld bead. The prediction error using bag tree model is less than linear regression. The standard deviation between the $\boldsymbol{w'_b}$ and $\boldsymbol{w_b}$ is 0.394 mm. The maximum error is 0.86 mm.

5.8 Conclusion

In this section, the supervised machine learning method was applied to monitor welding penetration based on the new features calculated from passive vision images. A training database with large variance of welding conditions was established. The weld pool backside width was predicted with linear regression, artificial neural network and bagging tree method. The conclusion was drawn as follows,

1. The importance analysis and feature selection were conducted for both linear regression and bagging tree. The result shows that the variables related to topside weld pool geometry including weld pool width, weld pool length, surface height play the most important role to predict penetration.

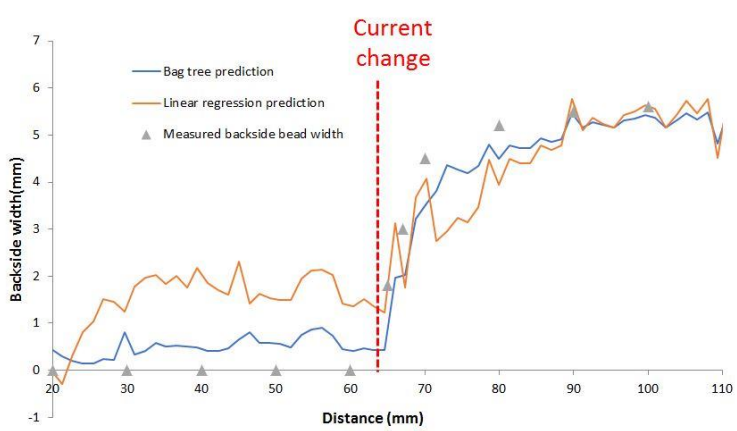

Figure 53. Prediction of weld pool backside width

2. The sequential feature selection was used to find out a better feature subset to improve the performance of linear regression model. However, the computation expense is relatively high.

3. The performance of bagging tree method is better than linear regression for the tests on the training database and new experiment data.

4. The time consumption of image processing and prediction is less than 300 ms which can be applied in real time welding penetration monitoring and control.

CHAPTER VI PENETRATION CONTROL OF BEAD ON PLATE WELDING

6.1 Framework

The close loop control algorithm plays an important role to ensure full penetration during welding. The schematic of penetration control system is shown in Figure 54. PID control method was applied to adjust welding current. As a direct indicator of welding penetration, the weld pool backside width was used as the feed-back of welding process. However, the backside width W_b(t) cannot be measure directly from the sensors. In previous section, the data driven penetration prediction model was established to calculate the estimated backside width W'_b(t) based on the features obtained from the weld pool topside images. The welding current I(t) can be regulated through the PID controller.

The target backside width W_r(t) is the reference of the feed-back control system. The error e(t) is the difference between the current backside width W_b(t) and the reference.

The proportional-integral-derivative(PID) control mechanism was applied in the control system. The function can be described as follow,

$$u(t) = K_P e(t) + K_i \int_0^t e(t')dt' + K_d \frac{de(t)}{dt} \tag{6-1}$$

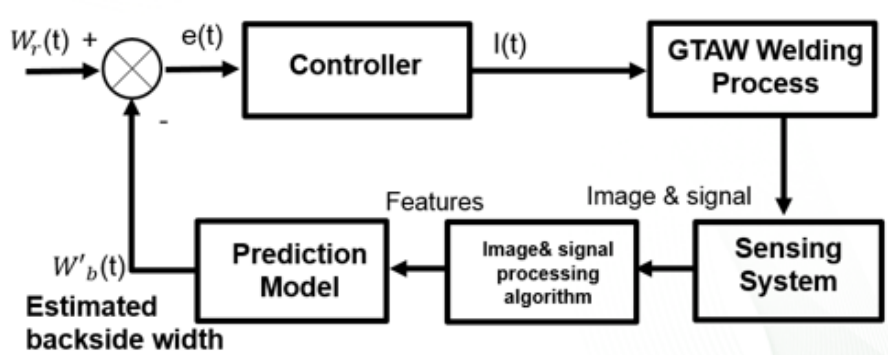

Figure 54. The schematic diagram of PID closed-loop control system

The e(t) is the error between the reference and the feedback value. The K_P , K_i, K_d are the coefficient of proportional-integral-derivative terms. Adjustment of the coefficient highly affected the result of control. The large K_P result in a quick response of the controller but will make the system unstable. The K_i will increase the movement of process towards reference and reduce the residual error. However, it may cause the overshoot issue in the beginning of the movement. The K_d can reduce the overshoot error and improve the stability of the system during steady state. The determination of the three parameters can highly affect the performance of penetration control. The procedure of adjusting the three parameters is shown as follow,

1. Identify the dynamic model of the welding process
2. Adjusting the parameter with PID turner.
3. Simulation and experiment.

6.2 Modeling Welding Dynamic Behavior

6.2.1 Dynamic modeling identification

The dynamic model is the foundation of develop control algorithm. In this section, a linear single input and single output (SISO)model was established to describe the dynamic behavior of welding process.

To obtain the discrete model for the dynamic welding process, an ARX (Auto-Regressive with exogenous input) model was identified through least square method. The equation of ARX model is expressed as follows,

$$W_b(k) = \sum_{i=1}^{n} a_i \, W_b(k-i) + \sum_{j=0}^{m} b_j \, I(k-j-d) + e(k) \qquad (6\text{-}2)$$

Where n and m are the order of the model, and d is the delay of the model.

The z transform of Equation (6-2) can be written as:

$$A(z)y(z) = B(z)u(z) + e(z) \tag{6-3}$$
$$\begin{cases} A(z) = 1 + a_1 z^{-1} + a_2 z^{-2} + \cdots + a_n z^{-n} \\ B(z) = b_0 + b_1 z^{-1} + b_2 z^{-2} + \cdots + b_n z^{-m} \end{cases}$$

Where y(z) is the output backside width, and u(z) is the input current.

The transfer function H(z) was given as,

$$\mathrm{H(z)}=\frac{Y(z)}{X(z)} = \frac{b_0+b_1z^{-1}+b_2z^{-2}+\cdots+b_nz^{-m}}{1+a_1z^{-1}+a_2z^{-2}+\cdots+a_nz^{-n}} \tag{6-4}$$

The dynamic model of welding process was identified based on the input and output data of step response. As shown in Figure 55, the input current changed from 100 to 125 A. And the output backside width was obtained from the result of prediction.

The least squares method was applied to identify the parameters of ARX model as shown in Equation (6-5). MSE was the criteria to evaluate the preformation of estimation. The best MSE was 0.23 with n=3, and m=2, d=0.

$$W_b(k) = 1.3778W_b(k-1) - 0.3003W_b(k-2) + 0.1521W_b(k-3) + 0.05I(k-1) - 0.03I(k-2) \tag{6-5}$$

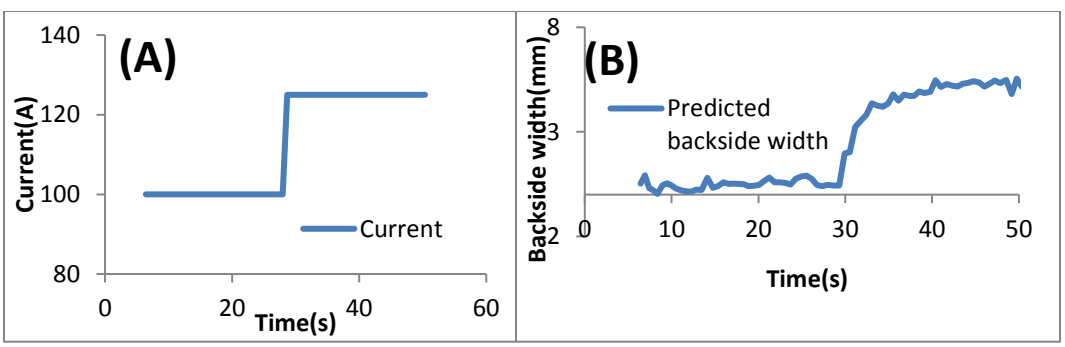

Figure 55. (a) Input signal of step test; (b) output signal of step test

6.2.2 Simulation

The simulation of close loop control system using MATLAB Simulink was established as shown in Figure 56. The ARX model was used as the plant to simulate the welding process. The gains of the PID controller were adjusted through MATLAB PID tuner. The controller with proportional gain at 6.8, integral gain at 4.7 and derivative gain at 0.28 can meet the requirement of control. The performance of the controller can be analyzed through simulation as shown in Figure 57. 5mm weld pool backside was used as the reference. The initial current was 100A. The output W_b increased from 0 to 5mm in a few second. The over shooting is less than 3%. The error band is less than 1% after it the output was stabilized. The setting time is 5.3 second and rising time is 1.12 second.

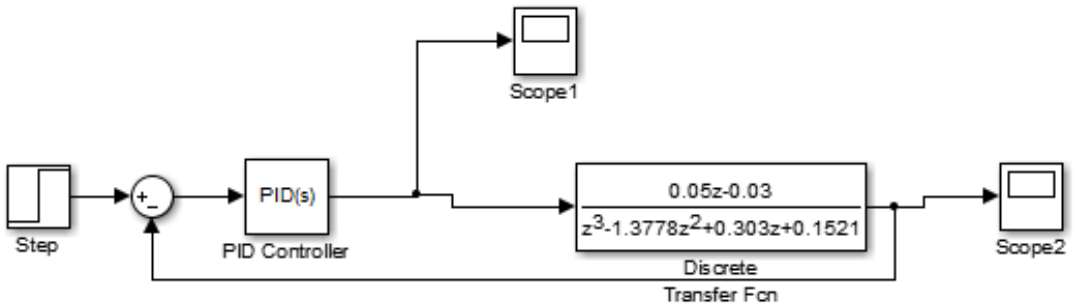

Figure 56. PID control system blocks using simulink

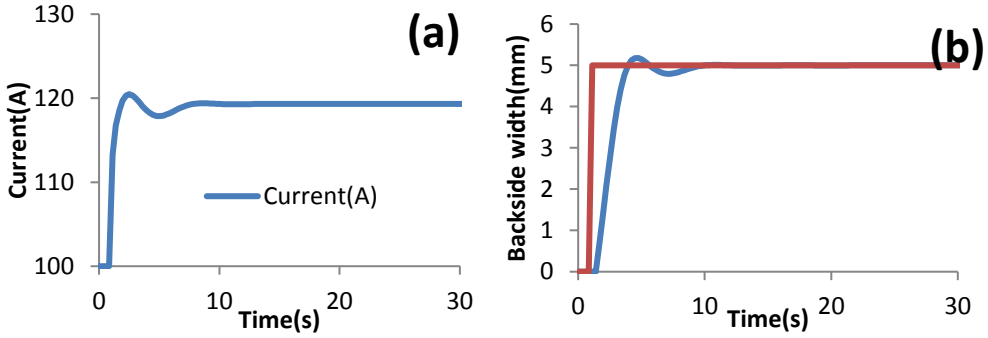

Figure 57. (a)Observation of input current; (b) observation of system output

6.3 Penetration Control on Uniform Thickness Plate

To evaluate the performance of PID controller, two experiments were conducted on 3mm SS304 plate with 2mm/s travel speed. Both experiments were started with same welding condition. The initial welding current is 100 A which is insufficient to penetrate the plate. The value of PID gain was different.

The weld bead of the welding experiment with non-optimized gains is shown in Figure 58. The controller of the experiment has the proportional gain at 8.25, integral gain at 3.3 and derivative gain at 0.1. The large proportional gain can reduce the setting time. However, the stability of system was highly affected. The system output curve was shown in Figure 59, the target increased to 5mm at 26second. In the beginning of the step change, the output value over shoot the reference value. The over penetration was produced. The control system speeds more time to get stabled. The performance of the controller cannot meet the requirement due to the large over shooting and long setting time.

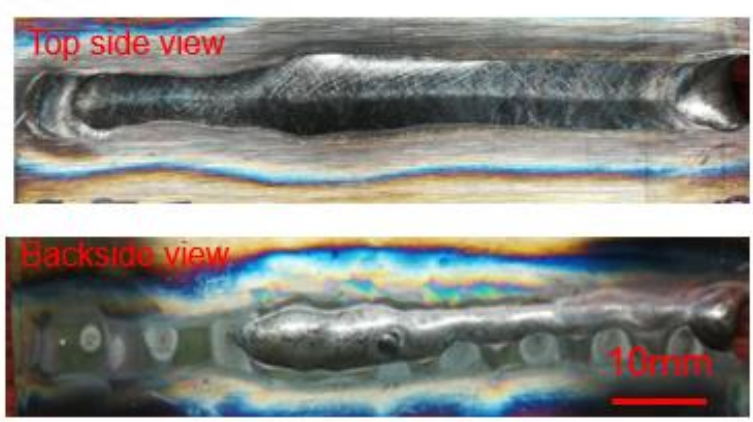

Figure 58. Topside view and backside view of weld bead with non-optimized PID gains

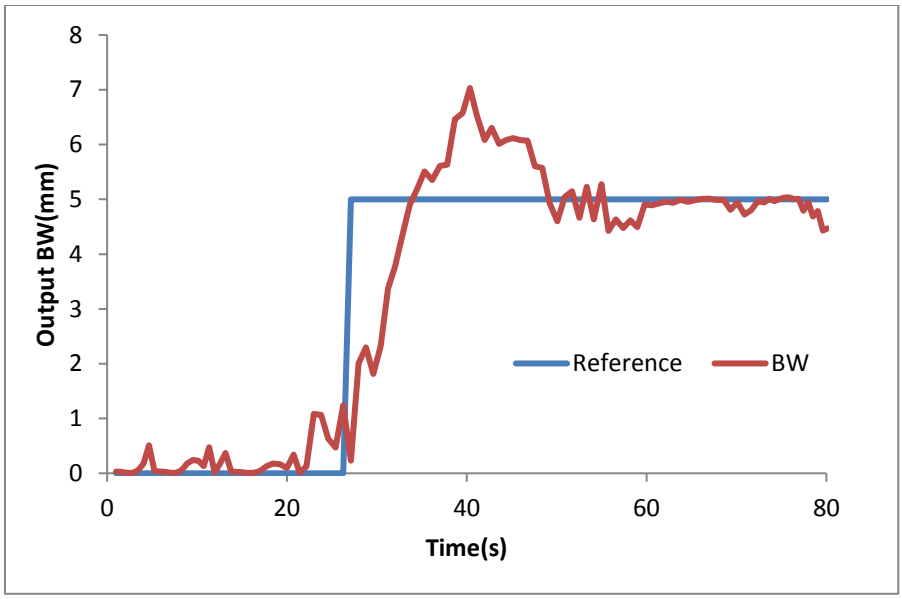

Figure 59. Output signal of non-optimized PID gains

The weld bead of the welding experiment with optimized gains is shown in Figure 60. The backside width control started at 30 second. The proportional gain was 6.8, integral gain was 4.7 and derivative gain was 0.28. The output curve was shown in Figure 61. The overshooting was less than 5%. The setting time was 14 second. And the error band was less than 3% of the reference. The performance of the PID controller satisfied the requirement.

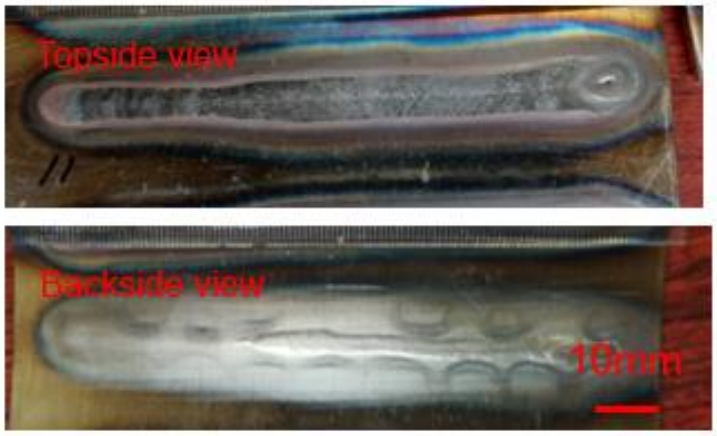

Figure 60. Topside view and backside view of weld bead with optimized PID gains

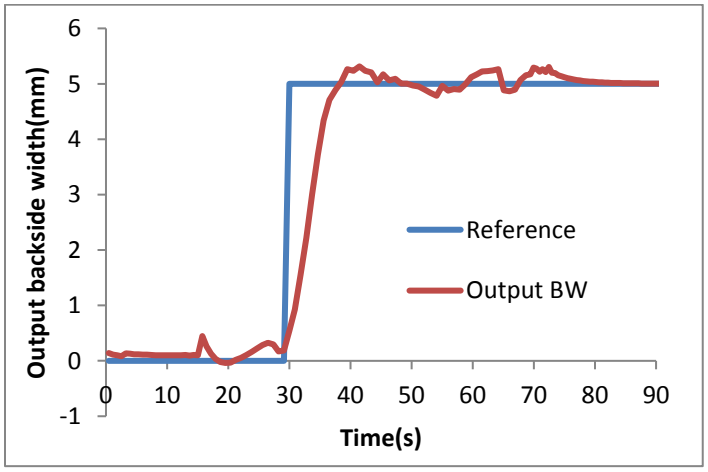

Figure 61. System output with optimized PID gains

6.4 Penetration Control on Different Thickness Plate

6.4.1 System modeling

The material thickness is a major factor that affects the penetration condition. In many manufacturing conditions, the welding parameters and the PID gains should be adjusted due to thickness change of the weldment. In this section, a new control algorithm was developed to control penetration on the workpiece with thickness changed from 2mm to 3mm.

In previous chapter, several bead-on-plate experiments conducted on 2mm and 3mm plate were included in the database. Based on the experiment result with same welding speed(2mm/s), the static correlation between welding current and backside width was plot in Figure 62. For 2mm thick plate, full penetration was produced as the current was above 65A. It was observed that the current and backside width are linearly related for the same thickness weld. However, a large change of current is required to produce same backside width weld on different thickness plate.

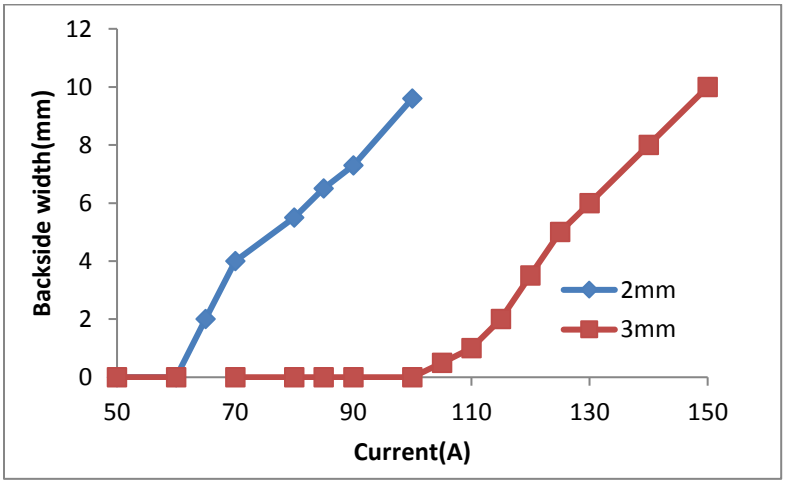

Figure 62. Static correlations between the welding current and backside width on different thickness plate

As an example, if the reference backside width is 5mm. Since the heat dissipation of workpiece are different, 75A current is required to produce full penetration on 2mm, while 125 A is required for 3mm. However, the conventional PID controller developed in previous section takes long time to adjust the current from 70 to125A if the material changed from 2mm to 3mm. Hence, it is important to establish separate dynamic model for the weld on different thickness plate. And the optimal PID parameter will be changed accordingly. The first order system transfer function is shown in equation (6-6). The T is the time coefficient T, gain coefficient K and delay constant τ were identified using MATLAB identification tool box. Three experiments with step change of welding current were conducted for each thickness of workpiece. The coefficients of each experiment were shown in Table 9 and Table 10. The final coefficient was the average of the three experiments. The system gain coefficient K of test under 2mm is higher than the test on 3mm. And time delay was found in 3mm. The result indicated that the W'_b(t) is more sensitive with current change for the test on thin plate.

$$G(s) = e^{-\tau s} \cdot \frac{k}{1+Ts} \tag{6-6}$$

Table 9. Identified coefficient for the experiment on 2mm workpiece

	k	T	τ
Test 1	0.4028	5.789	0
Test 2	0.3804	6.606	0
Test 3	0.36	7.034	0
Mean	0.36	6.4	0

Table 10. Identified coefficient for the experiment on 3mm workpiece

	k	T	τ
Test 1	0.202	6.772	0.25
Test 2	0.24	5.387	0.39
Test 3	0.242	5.996	0.97
Mean	0.23	6.03	0.536

Due to the significant change of plant model, the PID parameters need to be adjusted adaptively. A modified control system frame work with self-tuning PID controller was proposed in Figure 63. A logistical classifier was established to determine the thickness of the workpiece from W'_b(t-1) and I(t-1). The accuracy of thickness determination is 99.1%. The PID gains will be adjusted to optimal value based on the determined thickness. The optimized PID parameters are shown in Table 11.

6.4.2 Experiment

A bead on plate experiment was conducted on the 2mm and 3mm thickness plate with 2mm/s welding speed. As shown in Figure 64, the weld started from 2mm plate and travel towards 3mm plate. The first 32 mm weld was uncontrolled with a constant current. The close loop control was then started, and the reference backside width was 5mm. The PID gains was optimized which was able to meet the requirement to weld on 2mm thin plate. One the weld was travel to 3mm plate. The partial penetration occurred due to the step change of material thickness. The reducing of backside width was detected with the AI prediction model.

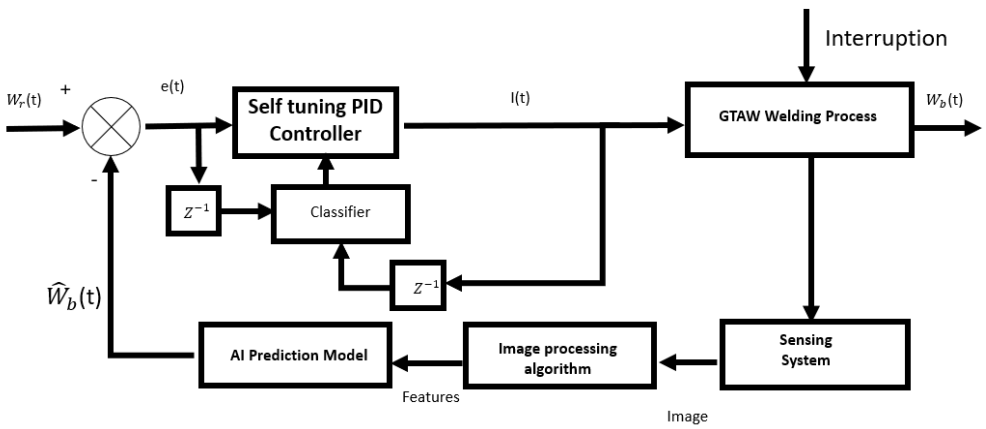

Figure 63. The schematic diagram of self-tuning PID closed-loop control system

Table 11. Optimized PID parameter

	Kp	Ki	Kd	Over shoot	Setting time	Rising time
2mm	3.96	2.38	0.168	4.32%	6.82	2.49
3mm	6.8	4.7	0.28	4.36%	14	2.68

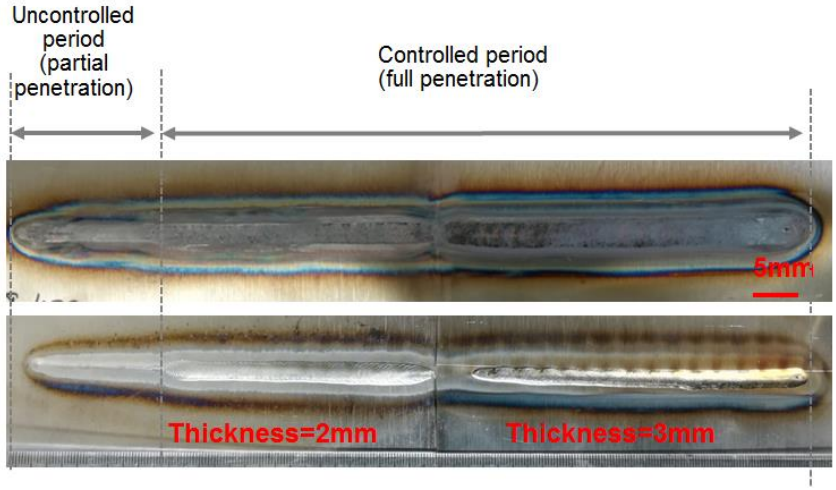

Figure 64. Topside view and backside view of weld bead on non-uniform thickness plate

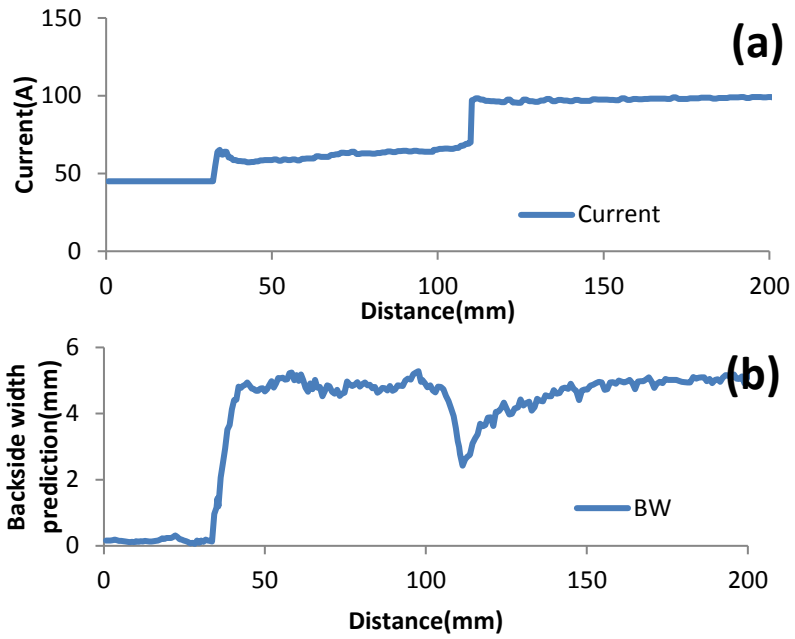

Figure 65. (a) Input current during welding on non-uniform thickness plate; (b) output backside width during welding on different thickness plate

Once the thickness change was detected from the classifier, the gains of PID were automatically adjusted which is suitable for welding on 3mm plate. The control system needed 10 second to adjust the penetration back to the target. The input current signal and output prediction result was shown in Figure 65.

6.5 Conclusion

In this section, close loop control system was implemented to control uniform backside width during bead on plate weld. The conclusion can be drawn as follow,

- The over shooting problem can be solved with optimized PID gains.
- The setting time was reduced to 10 second to reach the reference backside width.
- The PID gains were optimized for the weld on different thickness plate.

- The experiment on uniform thickness plate verified with the self-tuning PID controller. The gains of PID were adaptively adjusted to reach the control reference while the thickness of workpiece was suddenly increased.

CHAPTER VII
PENETRATION DETECTION OF NARROW U-GROOVE WELDING

7.1 Welding Parameters

7.1.1 Welding joint design

The multi-pass groove weld is more commonly used in welding manufacturing. For thick material welding, large heat input is required to get full penetration for the butt joint weld. By filling a groove design joint makes it possible to weld the workpieces with less heat input.

There are many typical groove designs including U type groove, V type and J type. The V-type groove has been used in many manual welding conditions. The U type groove is most commonly used during automatic welding. Most of the welding inside groove requires filter wire. In this section, we focus on develop new method using computer vision and machine learning techniques to detect defects of multi pass groove welding in U-type joint. The design of weld joint is shown in Figure 66. The U groove was milled on the side of the square butt joint. The thickness of plate was 6 mm and 12 mm. The radius of the groove bottom was 5 mm. The root face ranges from 1 to 2 mm.

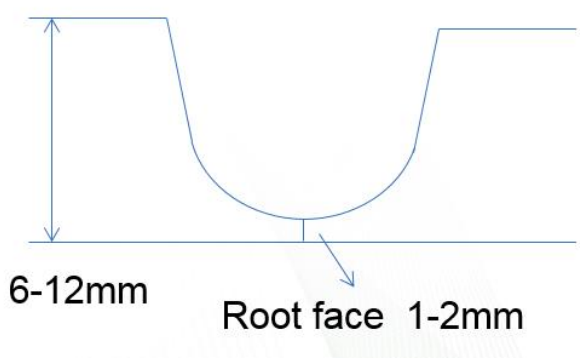

Figure 66. Design of narrow U groove welding joint

Since the zero-gap configuration was applied for the welding joint, no filler wire is required for the root pass weld. To eliminate the potential defect such as incomplete penetration, it is crucial to produce full penetration for the root pass weld. In this section, machine learning approach was applied to detect penetration for the root path of weld inside U groove joint.

7.1.2 Establishment of database

There are 15 trails of first path weld was conducted on the U-groove joint as listed in Table 12. The welding current changed from 90-150A. The welding speed changed from 1 to 2mm. The root face thickness changed from 1 to 2mm. Among all the 15 welds, there are 8 welds of incomplete penetration, 5 welds of complete penetration and two welds of over penetration.

Table 12. Welding parameters of root pass welding

No.	Root face thickness (mm)	Thickness of workpiece(mm)	Current (A)	Speed (mm/s)	Penetration condition
1	1	6	100	1	complete
2	1.5	6	100	1	incomplete
3	2	6	100	1	incomplete
4	1	6	120	1	complete
5	1.5	12	120	1.5	Incomplete
6	2	6	120	1	incomplete
7	1.5	6	90	1	Incomplete
8	1.5	6	100	1.5	incomplete
9	1.5	6	120	1	incomplete
10	1.5	6	130	1	complete
11	1.5	6	140	1	Complete
12	1.5	6	150	1	over
13	1	6	150	1	over
14	1.5	12	150	2	complete
15	1.5	12	150	3	incomplete

The three penetration conditions were determined based on the backside width. The backside width of the incomplete penetration weld was less than 2mm. The complete penetration was between 2mm and 8mm. And the over penetration was above 8mm. A negative reinforcement of bottom bead was formulated as the weld becomes over penetrated. The surface tension is major force which changes the shape of the bead.

7.2 Image Characters of Root Pass Welding

7.2.1 Images character of multi-optical sensing condition

The images obtained with different optical condition were shown in Figure 67. The exposure time increased from 20μs to 470 μs with increment of 50μs. All ten images were obtained within 10ms during one weld. In Figure 67, the electrode and the REI can be visualized in short exposure time image under 20μs .

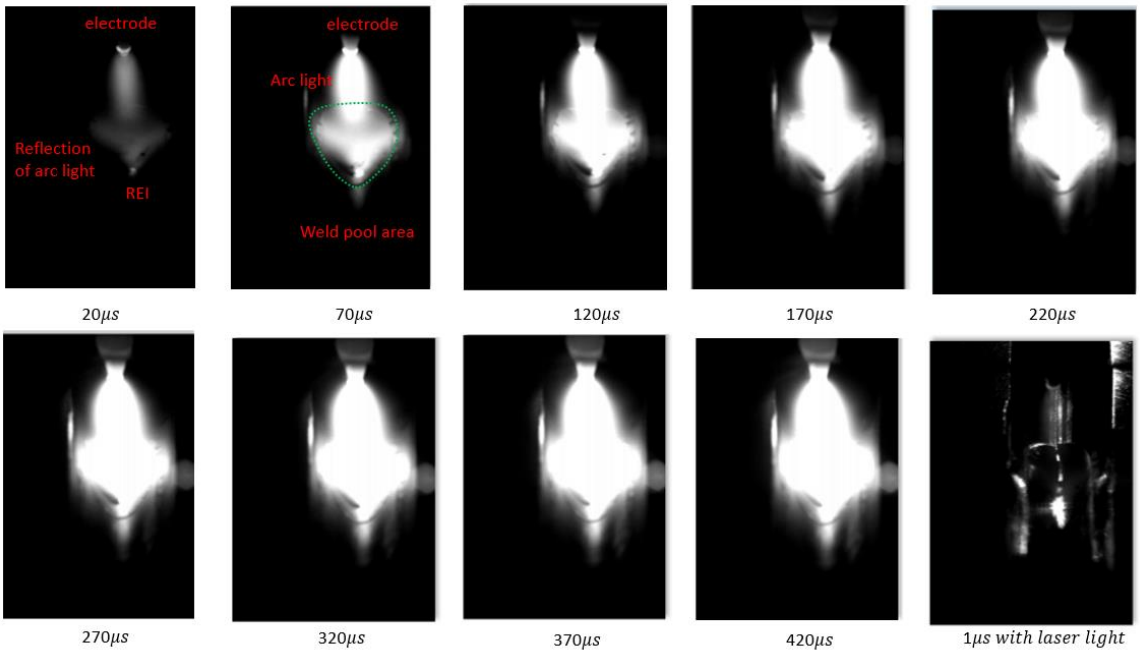

Figure 67. Images acquired during U-groove welding with changing exposure time

The arc reflection area was distorted due to the curvature weld pool surface. The

weld pool can be visualized with $70\mu s$, $120\mu s$ exposure time. By increasing the camera exposure time, reflection of arc area became saturated. And the weld pool was overwhelmed due to over exposure. The active vision image was obtained at the last frame. However, it is hard to visualize the weld pool boundary due to the shadow of the groove side wall. In this paper, the image obtained with 20 us and 120 us exposure time were used for penetration detection.

7.2.2 Acquire images with different welding condition

The images obtained under different optical conditions are important information source which can be used to predict welding penetration. In this section, the images obtained with 20 μs and 120 μs exposure time were studied in different welding condition. To quantitively compare the difference between experiment, four features were extracted as shown in Figure 68. WREI is the width of the REI. Warc is the width of the arc reflection area. IREI is the intensity of the REI. DERI is the distance between electrode location and REI.

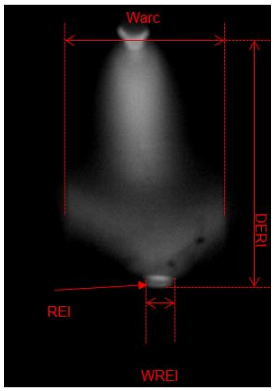

Figure 68. Features extracted from passive vision image

To further understand the effect of input current on the penetration. The experiments

with different welding current on the same welding joint were compared in Figure 69. The root face of the 5 welds was 1.5mm.

The partially penetrated welds were produced under 100A and 110A. A small weld pool was produced in the middle of the groove as shown in Figure 69 (b1, b2). In the image obtained under 10 μs shown in Figure 69(a1, a2). The REI and reflection of arc area was not found in the image because the weld pool area is too small.

The full penetrated welds were produced under 130A and 140A. The weld pool area was increased and changed into a triangle shape. REI and reflection of arc can be visualized in Figure 69(a3, a4). Warc is close to the width of the weld pool.

A over penetrated weld was produced with 150A. As shown in Figure 69(a5), the Warc was expanded to the whole groove. Beside that the WREI was increased due to the concave weld pool surface.

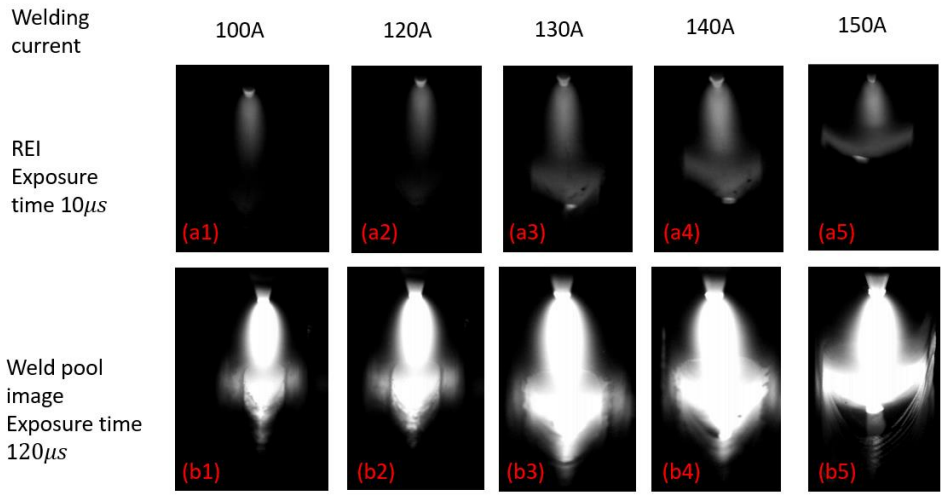

Figure 69. Passive vision images of 5 welds with different welding current

Another important factor affects the penetration was the root face(RF) thickness. In

many manufacturing processes, the root face of the U-groove may various due to the machining error. The image of three welds produced by same welding current I=120A but different RF were compared in Figure 70. For the Rf=1mm case, the weld was fully penetrated. For RF=1.5mm, the weld was just penetrated with small backside width. The weld is not penetrated for the third case with 2mm root face. From the passive vision image shown in Figure 70, the weld pool area was decreased with increase of root face. The reflection arc area and REI was also reduced with the increasing of root face. Which also indicated that the features extracted from REI is related with welding penetration instead of current change.

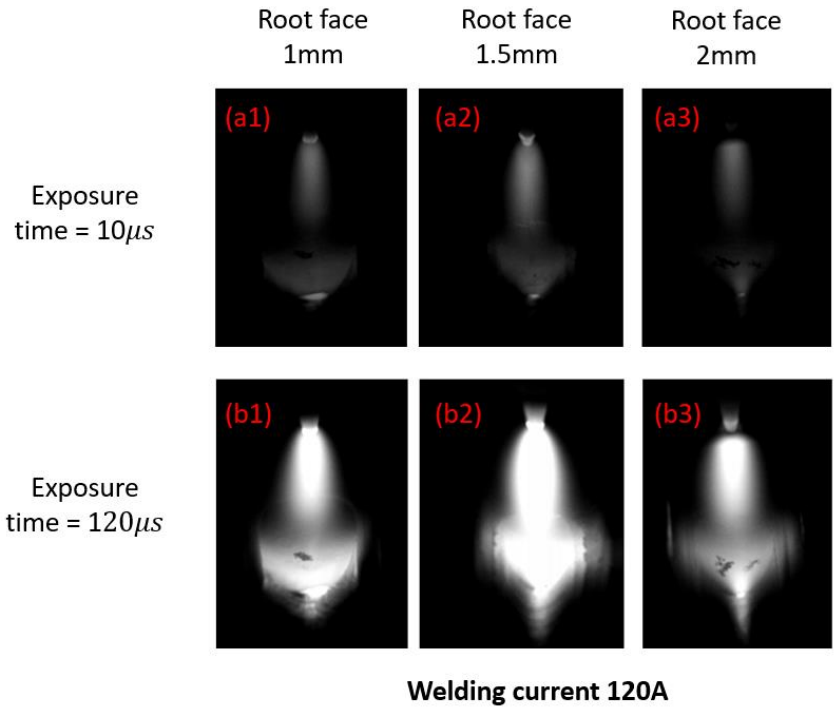

Figure 70. Passive vision images of 3 welds with different root face

7.3 Training of Prediction Model

7.3.1 Classification based on the extracted features

Many features related with penetration can be found from the passive vision images. In this section a bag tree model was trained to classify the penetration based on the features extracted from image, which include WREI, Warc, DERI and IREI. The database includes 620 instances obtained from 15 trails of weld shown in Table 12. Statistical analysis was conducted based on the training database. Each instance of data was labeled based on the backside bead width. The three penetration conditions were included in the database. In Figure 71, the mean value and standard deviation of all the four variables under three penetration states was compared. The significant change of Warc can be found as the penetration changed from partial to over penetration. This feature is related to the weld pool geometry. The weld pool area increased with the increasing of heat input. The width of arc reflection was also increased.

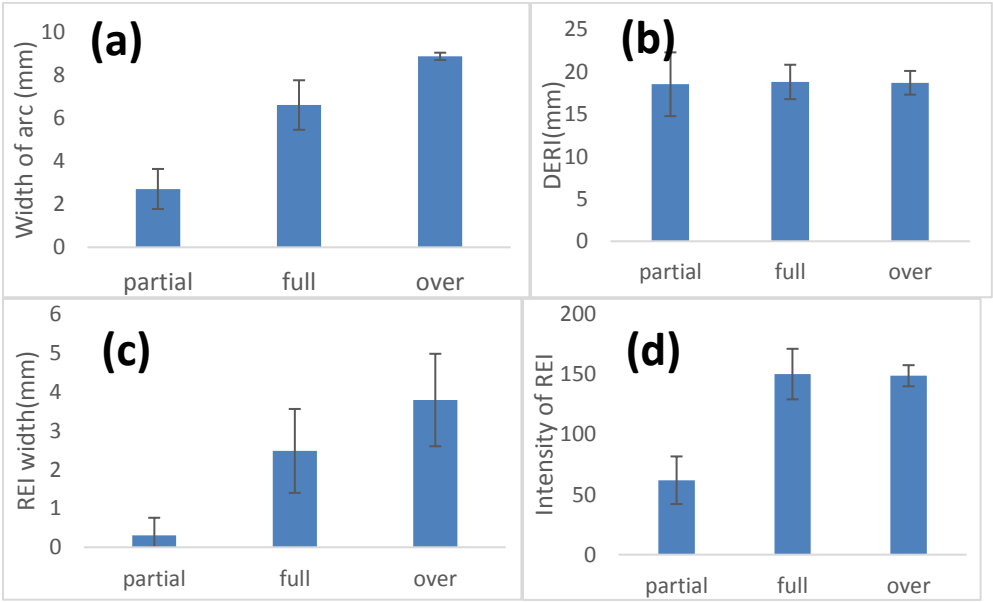

Figure 71. Comparison of the four features under three penetration conditions

The feature of DERI is shown in Figure 71(B), the DERI is related to arc length and surface shape weld pool. The arc length is reduced with the increase of welding current. The mean value of DERI does not change significantly between the three different penetration conditions. However, based on the reflection model in our previous research, the surface height of weld pool can be further calculated based on DERI and arc length.

The REI width is related with the weld pool surface shape. The width of the REI was increased from partial to over penetration. In partial penetration stage, the WREI is close to zero. This feature may due to the two reasons: first the REI cannot be detected due since the weld pool area is small. If the REI cannot be detected on the surface, the IREI value will be much lower than the full penetrated condition. Second, once a convex weld pool surface is formulated during completed penetrated weld. The area of REI can be reduced due to mirror reflection.

Finally, 6 features were used as the input the bag tree model which includes: welding current, arc length, Warc, DERI, WREI, IREI. Figure 72 shows the out of bag error's change during training procedure. The out of bag error estimate the weighted ensemble error for out of bag observations. In classification problem, the weighted ensemble error means the weighted misclassification rate.

The out-of-bag error was significantly reduced over the number of grown classification trees. The upper limit of grown tree is 100. The error was reduced less than 0.02 after 20 trees which means 20 trees was enough to provides a good classification on the training database. The importance of the six features was also given in Figure 73. The third feature Warc and the IREI are the important features for classification. The final accuracy for classification is 98.5% which was evaluated with 5 folds cross validation.

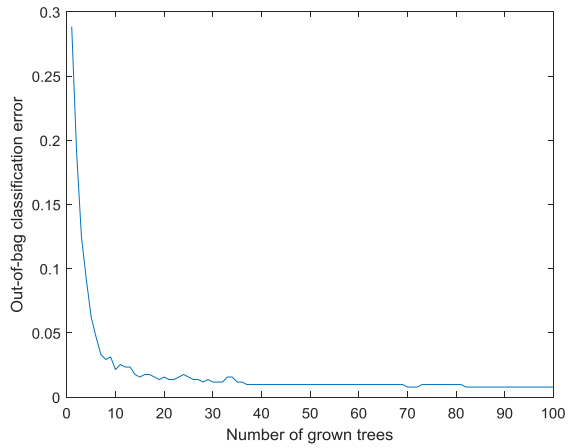

Figure 72. Out-of-bag error vs number of grown trees

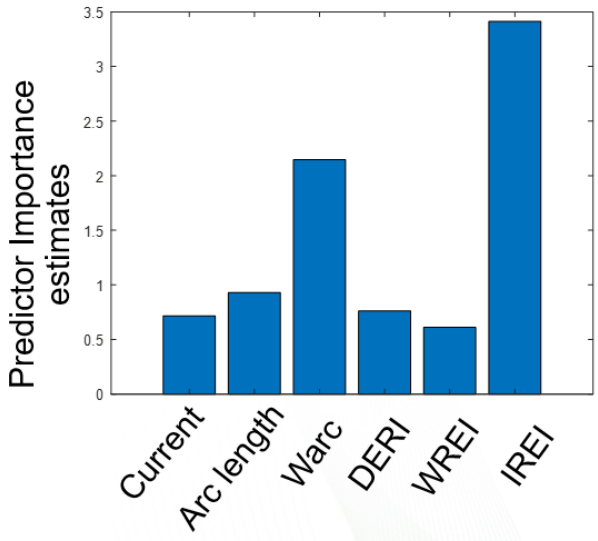

Figure 73. Predictor importance estimates

7.3.2 Backside width prediction with bag tree model

Backside width of weld pool is the important variable for close loop penetration control. The Wb can be predicted using regression tree. First, similar as we did before in chapter V, all the datasets in the database were labelled with the backside width which measured after welding.

The distribution of the error of training and testing dataset was shown in Figure 74. 70% of database was used for training and 30% was used for testing. The RSME of the training is 0.28. And the RSME of the testing datasets was 0.56.

7.4 Experiment Validation

The performance of the trained bagging tree model was further tested on the new experiments which were not included in the database. In Figure 75, three new welds were produced with 100A, 130A,150A current which represent the three different penetration conditions. The welding speed is 1mm/s. And the root face length is 1.5mm.

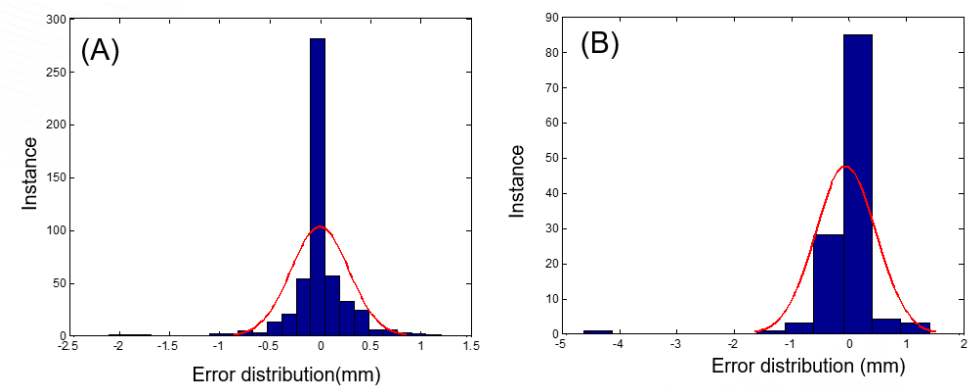

Figure 74. Error distribution for training and testing. (a) Error of the training dataset; (b) error of the testing dataset

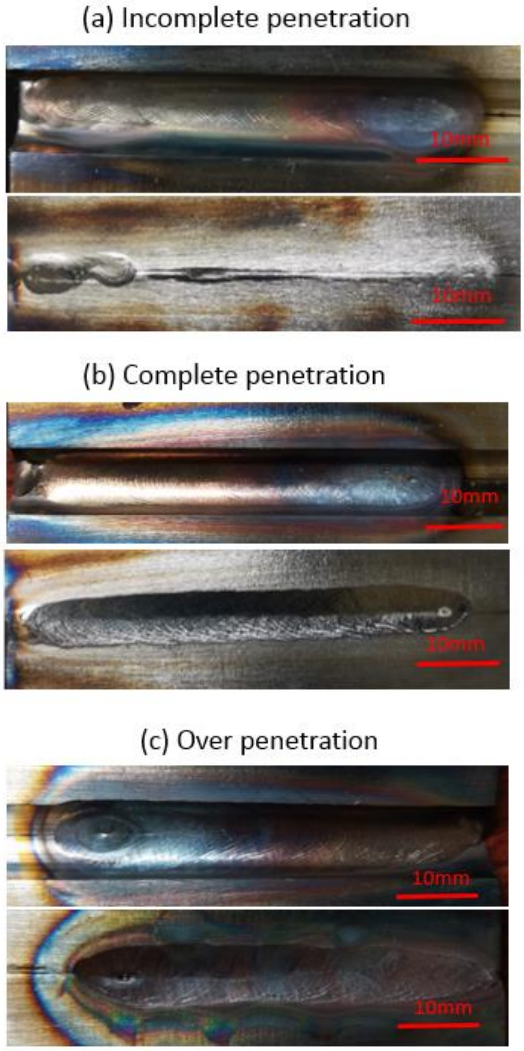

Figure 75. Three penetration condition inside U groove weld. (a) Incomplete penetrated weld performed at 100A current and 1mm/s welding speed; (b) complete penetrated weld performed at 130A current and 1mm/s speed; (c) over penetrated weld performed at 150A current

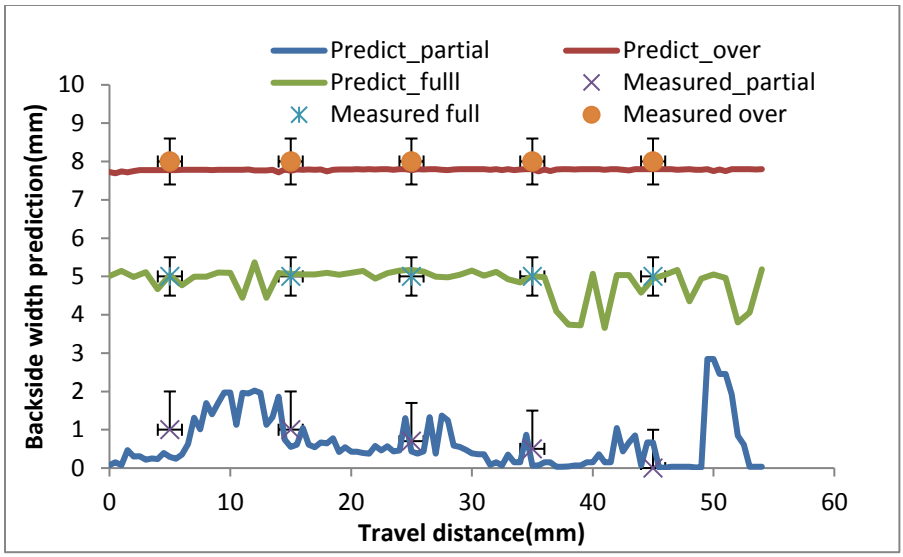

Figure 76. Real time backside width prediction of root pass weld

First, the bagging tree classification model achieved 87.5% accuracy to determine the three different penetration stages. This model may suffer from over-fitting during training process. The predicted result using bagging tree regression model was shown in Figure 76. The predicted backside width is close to the measurement after welding. The RSME of regression is 1.01. And the MAE of the error is 0.71. Thus, the predicted result can be further used as the feedback in close loop control system.

7.5 Conclusions

In this section, the welding penetration was studied for the root pass inside U-groove. The images from passive vision system were used as the major information source to predict penetration. Welding current and root face thickness are the major parameters that affect joint penetration. New features extracted from reversed electrode image (REI) and weld pool images were found closely related to the penetration. The classification and

regression model were also trained based on the established database. Sufficient accuracy was achieved using bagging tree model.

CHAPTER VIII LACK OF FUSION DETECTION INSIDE NARROW U-GROOVE

8.1. Introduction of Lack of Fusion Defect

The lack of fusion (LOF) defect has been a crucial issue for multi-pass groove welding. It is very challenging to detect this defect with non-destructive method. In some circumstances, the LOF can be detected with radiography or ultrasonic sensors if the defect includes voids or inclusions [105]. In reference [106], the ultrasonic device was used to detect lack of fusion on groove side wall. The reflection of ultrasonic waves indicated the presence of lack of fusion in a certain depth. However, the equipment to conduct these tests increased the cost of production. And, currently, there is no effective method which can directly detect the LOF due to discontinuity of welds.

In this section, we proposed a new real time method to predict LOF defect formulated on groove side wall. The prediction model was established based on the features extracted from passive vision images.

8.2. Design of Multi-pass Welding Experiments

The design of U-groove is same as we described in Chapter VII. The schematic of the layer planning is shown in Figure 77. The first path was conducted with filler wire and melt through the root face. Additional 5 to 10 paths of weld with filler wire were performed to fill the groove. The final weld path was on the top of the groove which covers the entire joint. The electrode travels along the center of the groove without swing. In this configuration, the side wall fusion is the major issue needs to be taken care of.

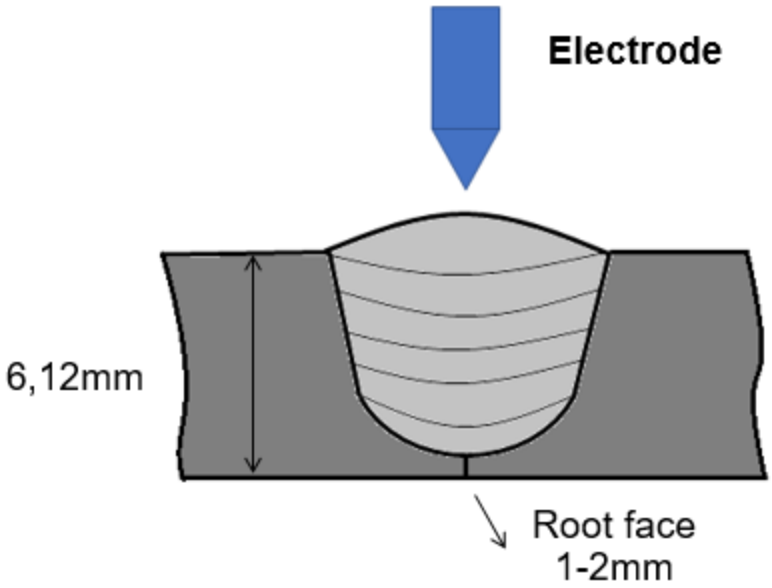

Figure 77. Schematic of layer plan in U-groove joint

Since the width of the groove is increasing from bottom layer to the top layer, the welding parameters including current, traveling speed and wire feeding speed to conduct different layers should be adjusted to prevent lack of fusion on side wall.

The welding parameters to fill the U-groove were shown in Table 13. 12 trails with filter wire were performed on the two types of workpieces. Both two types have similar design of at the bottom of the U-groove. The radius of the groove bottom was 5 mm. And root face is 1.5mm. However, the total thickness of type II is 12mm and type I is only 6mm. The first 5 trails shown in Table 13 were conducted on the workpiece type I with 6mm thickness. And the rest of them were performed on workpiece type II. Since the first layer of weld was conducted with no filler wire, they are not included in this table.

Table 13. Welding parameters of multi-pass narrow gap weld

No.	Layer number	Current (A)	Travel speed (mm/s)	Wire feeding speed(inch/min)	workpiece Thickness	Lack of fusion
Dataset I	I	150	1->2	25	6	Y
	II	150	1->2	30	6	Y
	III	150	1->2	30	6	Y
	IV	150	2	25	6	Y
	V	150	2	20	6	Y
Dataset II	I	150	1->2	25	12	Y
	II	200	1->2	40	12	Y
	III	200	1.8->2	40	12	Y
	IV	200	1->2	40	12	Y
	V	220	1	40	12	N
	VI	220	1->2	40	12	Y
	VII	220	1	50	12	N

The welding speed for some of the experiment show in the table was manually increased during the middle of the welding. Then the lack of fusion defect may be produced due to the decreasing of heat input. The wire feeding speed is also changed for different weld layers.

8.3 Experimental Observations

8.3.1 Weld bead geometry

In this research, the welding seam is kept in the center of the groove without any swing. The weld bead shape for different fusion condition is shown in Figure 78. In good fusion condition, the concave weld pool surface was formulated due to the surface tension and electromagnetic force. A lack of fusion weld may produce with insufficient heat input. As shown in Figure 78(b), the volume of weld pool was reduced with the decrease of heat input. And the edge of weld pool and the groove side weld was detached. A convex weld

pool surface may formulate under this condition.

The topside views of experiments 1-5 were shown in Figure 79. The travel speed was increased during the middle of the welding. The lack of fusion defect on side wall was formulated in most of the welds due to insufficient heat input. The significant defect can be found in the cross section view of the finished welding joint as shown in Figure 80.

The topside views of experiments 6-12 which conducted on workpiece II were shown in Figure 81. The significant lack of fusion was formulated at the 4th and 5th layer due to the increasing of travel speed during the middle of welding. Completed fusion was then produced on the 6th and 7th layer. The completed fusion welds have concave weld bead surface, while the incomplete ones have convex shape weld bead. An insignificant welding defect can be visualized from the cross-section view of the finished welding joint shown in Figure 82. The weld on upper layers can reduce the lack of fusion formulated on the bottom layers. Thus, the lack of fusion in workpiece II was less significant than the defect in workpiece I.

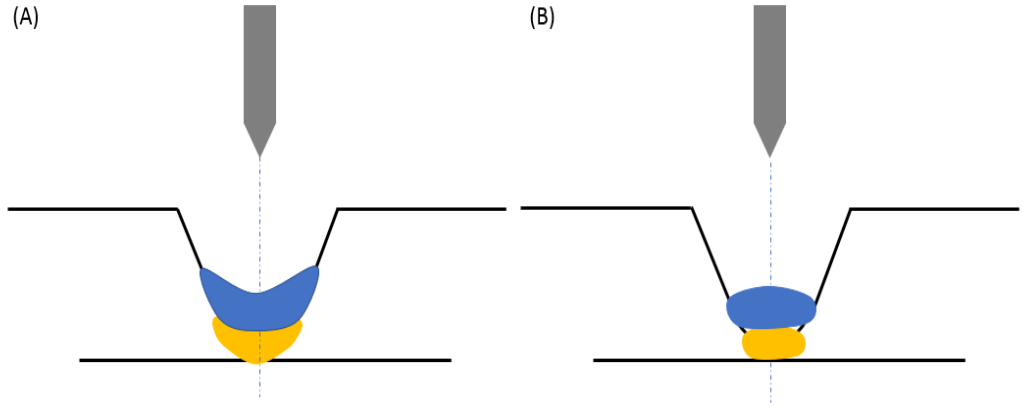

Figure 78. Description of weld pool surface inside U groove

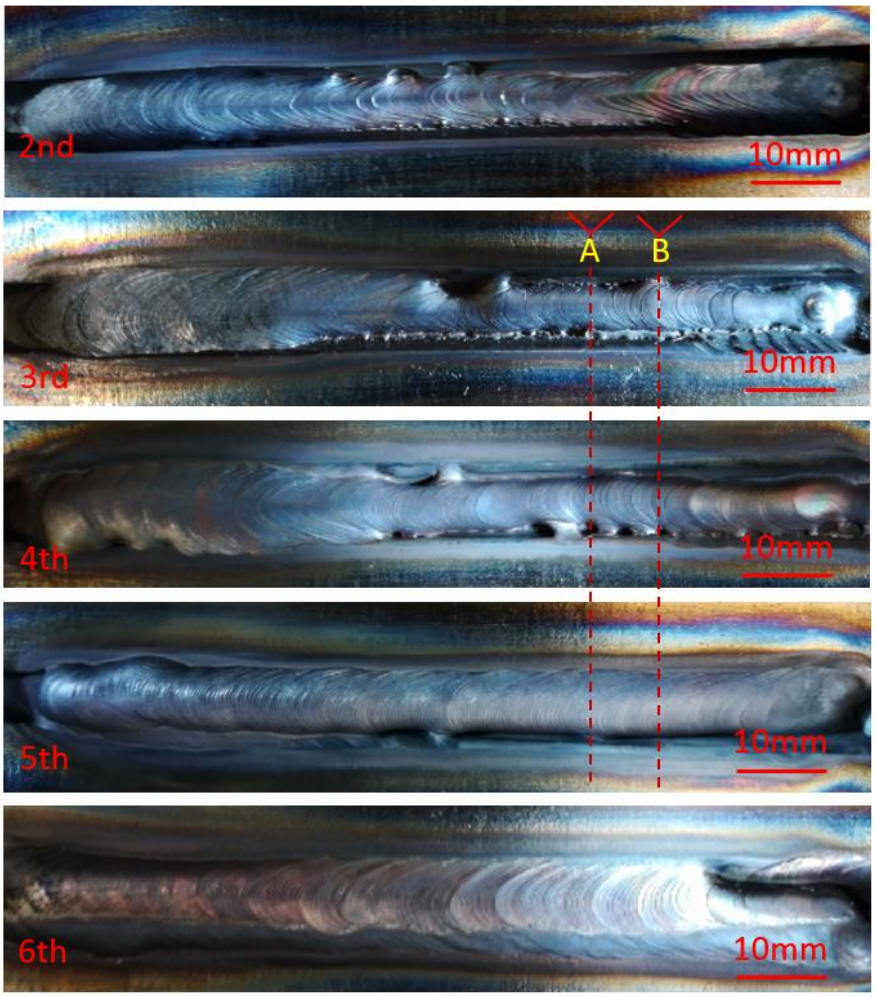

Figure 79. Topside view of the multi pass weld on workpiece I

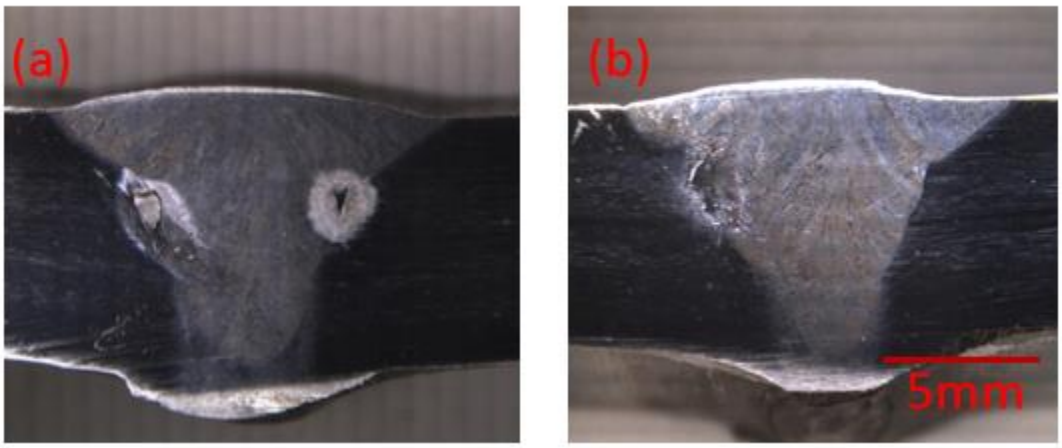

Figure 80. Cross section views of the finished weld joint on workpiece I

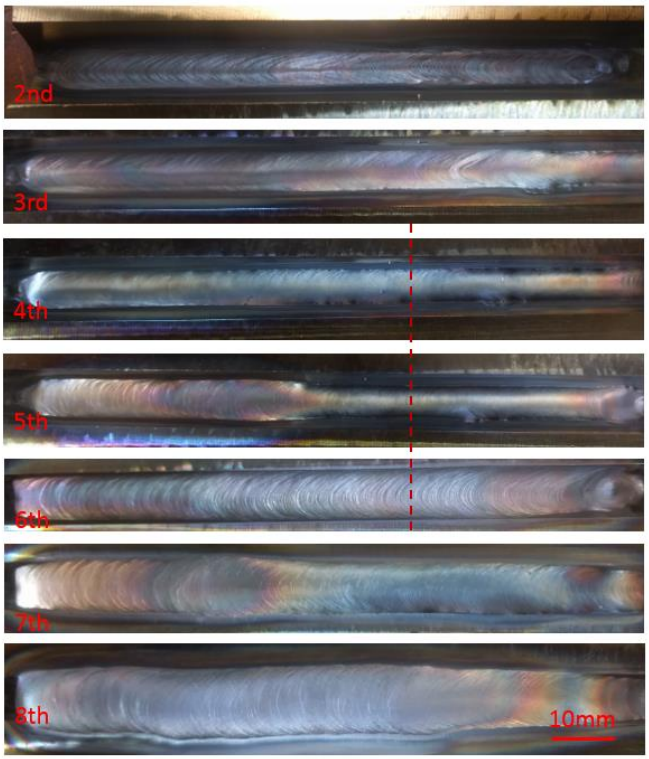

Figure 81. Topside view of the multi pass weld on workpiece II

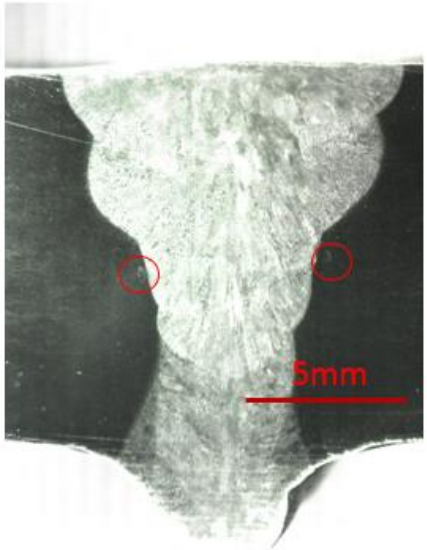

Figure 82. Cross section views of the finished weld joint on workpiece II

8.3.2 Characters of passive vision images

The passive vision images in Figure 83 are related with the cross-section A in the workpiece I. The REI and weld pool images of the five passes were obtained. In this experiment, the second path was fully penetration the root and no LOF defect was produced. The LOF defects were created in the middle of the joint where we conducted the III, IV and V layers. The discontinue weld were created as we increased the travel speed. Since the weld pool did not fully attached to the side wall. The weld pool area was shrinking into a ball. Convex weld pool surface was formulated due to surface tension. The REI size in III to IV was reduced which can be explained by the law of reflection on the convex surface[107]. The significant lack of fusion was also produced on the weld V, the weld pool was only attached to one side wall of the U-groove which formulated an unsymmetrical weld pool. The REI was not able to be visualized under low exposure image. The VI layer was the final layer which cover the top of the joint. A convex weld pool surface was produced to increase the face reinforcement of the joint.

The passive vision images in Figure 84 are related with the cross-section C in the workpiece II. And this time moment, the welds from 2nd layer to 7th layer were under completely fusion condition. The weld pool geometry shown in Figure 84 are symmetrical. The REI can be observed from the image with short exposure time. The size of REI is increased compare with the lack of fusion condition shown in Figure 84.

In complete fusion condition, a concave weld pool surface was formulated during welding. The geometry REI was affected by the concavity of the weld pool. As an example, the REI area of 5th layer was significantly increased with the concavity of weld pool surface which can be explained by the law of mirror reflection.

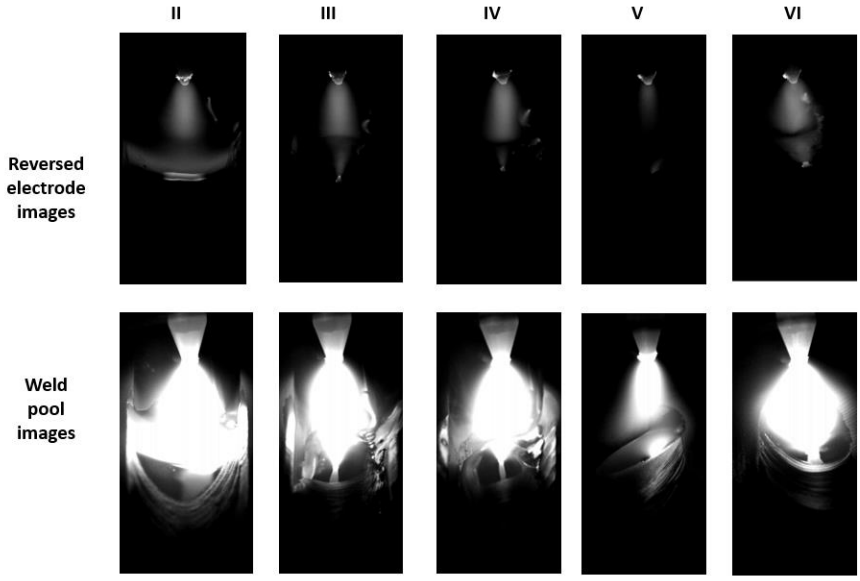

Figure 83. Passive vision images under lack of fusion condition

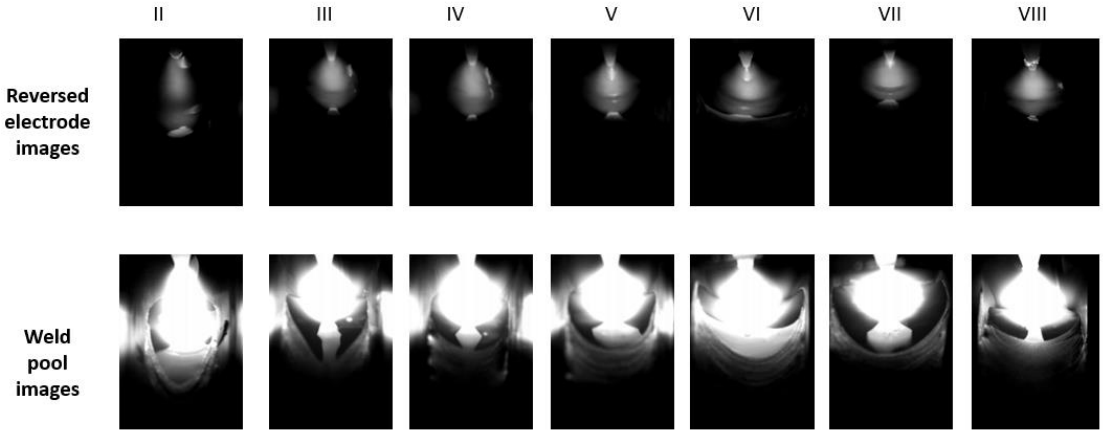

Figure 84. Passive vision images under complete fusion condition

8.3.3 Features extraction from passive vision image

Based on the observation of passive vision images, many important characters were found related to LOF. Four major features were extracted from the REI as shown in in Figure 85. The four features were automatically calculated using the ROI algorithm we developed in Chapter 4.

The extracted features of the welding on the 3rd layer of workpiece I were shown in Figure 86. The lack of fusion defect was produced at the third path of the weld. In the beginning of welding, the weld was fully fused with the side wall. The weld pool surface was concaved. The welding speed was increased after complete 10mm of weld. The volume of the weld pool was decreased. The weld pool detached from the side wall and formulates lack of fusion defect.

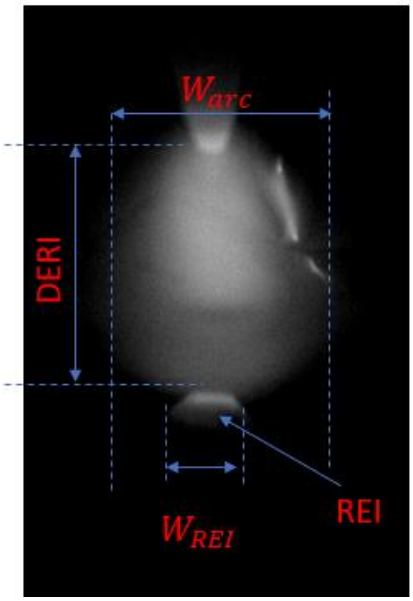

Figure 85. Features extraction from weld images

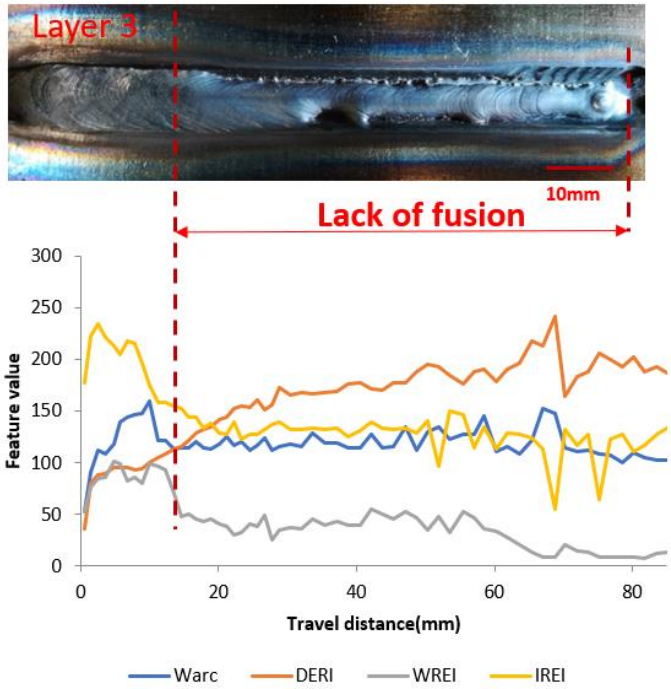

Figure 86. Extracted features of the third weld with lack of fusion defect

The width of REI W_{REI} and the intensity of the REI were reduced as the lack of fusion started. The convex weld pool surface works as a curve mirror which changed the reflection path of light. The feature of DERI was found increased as the lack of fusion started. The weld pool area moves upward as the lack of fusion started. The difference can be found on these three features. Since the standard deviation of the measurement is large, it is hard to determine the threshold which distinguishes the lack of fusion condition based on one feature.

8.4 Predict Lack of Fusion with Data Driven model

The data driven model was established to predict LOF defect using machine learning method. The database to predict lack of fusion was established based on the

experiment result. The dataset I contains 190 instances of data which was obtained from the experiments on workpiece 1; the dataset II includes 1244 instances of data obtained from experiments on workpiece 2. All the datasets were labelled based on the final weldment. The lack of fusion detection was considered as a binary classification problem. The lack of fusion condition was considered as the positive case(P); and the complete fusion was considered as negative case(N). The correct detection of lack of fusion is defined as true positive cases(TP); the correct detection of complete fusion is defined as true negative (TN); the incorrect detection of LOF is defined as FP; and the incorrect detection of complete fusion is defined as FN.

Each instance of the database contains four features extracted from reversed electrode images. The average value of the selected features in complete fusion and lack of fusion condition is compared in Figure 87. Significant difference can be found in the feature of Warc and WREI, which indicated that these two features are more important for classification.

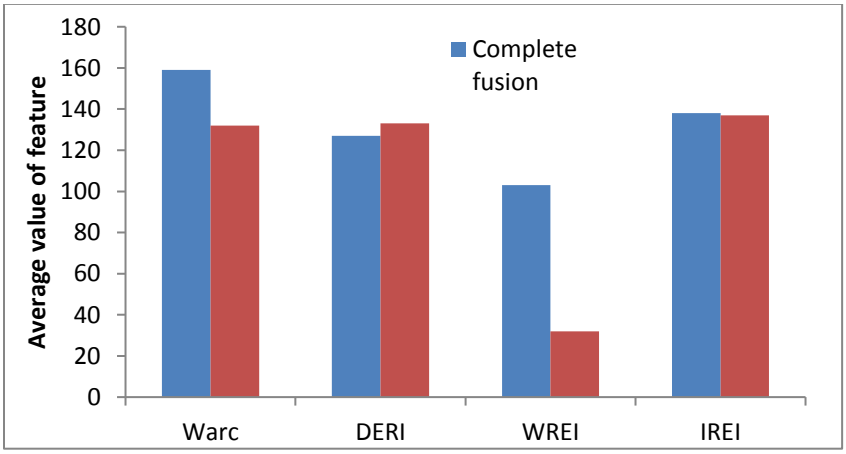

Figure 87. Comparison of feature in fusion and lack of fusion condition

The bagging tree model was trained to detect lack of fusion. All the four features were used for prediction. The performance of model with different training datasets was shown in Table 14. The following metrics were used to evaluate the performance of LOF detection:

- Accuracy indicates the ability to correctly determine fusion condition, accuracy=(TP+TN)/(TP+FP+TN+FN);
- Sensitivity indicates the ability to correct detect the defect with LOF, sensitivity=TP/(TP+FN);
- Specificity indicates the ability to correctly determine the weld does not have LOF defect, specificity=TN/(TN+FP);

The model 1 was trained with 70% of dataset I and tested with 30% of dataset I. Since all the data was obtained under similar welding condition, the accuracy is much higher. The model II was trained with dataset I and tested on dataset II which was conducted on different work piece. Since the welding parameter is slightly different with the training dataset. The accuracy is lower than the first model due to the variance of measured variables. To reduce the over fitting on one dataset, both of data in dataset I and II were used for training model 3. The final accuracy is 95.49%.

Table 14. Performance of bagging tree model with different training datasets

Number of Model	Training data	Testing data	Accuracy （%）	Sensitivity （%）	Specificity （%）
I	70% dataset I	30% dataset I	97.58	90.14	99.44
II	100% dataset I	100% dataset II	95.79	95.45	99.1
III	70% dataset I&II	30% dataset I&II	95.49	94.39	96.13

8.5 Software Integration

A real time multi-functional software was developed for LOF and LOP detection using MATLAB. The software interface was shown in Figure 88. All the images with different exposure condition can be obtained and processed in real time. The trained machine learning models were integrated into the software. For the root pass weld in U-groove and bead on plate weld, the software can be used for LOP detect. The weld pool backside width can be estimated and used for close loop control. The LOF detection function can be used for the welds with filler wire in U-groove.

8.6 Conclusions

In this chapter, new method was developed to detect lack of fusion defect in multi pass groove welding. The lack of fusion detect were formulated due to inappropriate welding speed and current. The weld pool surface geometry was also an important source of information related to LOF. Major features extracted from reversed electrode images may reflect the weld pool surface condition. The bagging tree models was trained to predict LOF defect based on these features. The test accuracy of LOF detection is 95%.

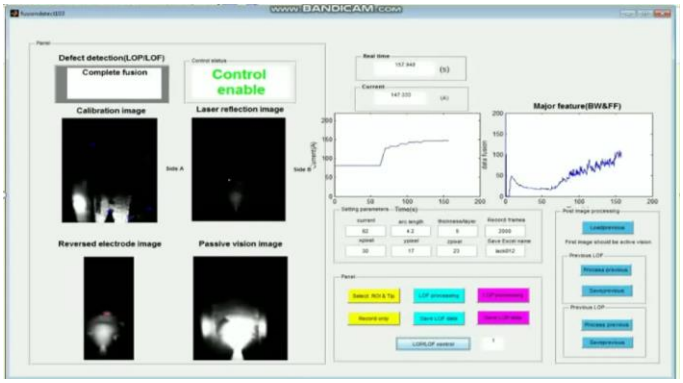

Figure 88. Software interface for LOP and LOF detection

CHAPTER IX CONCLUSIONS AND RECOMMENDATIONS

9.1 Conclusions

The welding defects such as incomplete penetration and lack of fusion are critical issues that affect the integrated of welding component. The weld pool geometry is the major source of information related to the formation of these defects. In this dissertation, new visual sensing and control system was developed to eliminate the welding defects during GTAW.

The development of weld pool surface visual sensing approach is the foundation of all the work in this dissertation. The unique visual sensing system can visualize the weld pool area to overcome the interference from arc light. Both active vision image and passive vision image were obtained during welding process.

In active vision images, the weld pool can be visualized with clear boundary. The random distributed reflection from laser light increase the challenge of boundary extraction. An algorithm with conventional image processing operation was developed to extract weld pool boundary under special optical conditions. Meanwhile, the depression of arc plasma force can also be observed with the presence of laser light reflection. Experimental study was conducted under different welding speed and current condition on 6mm SS304. It was found that the high-speed welding achieves better efficiency to produce same penetration depth compare with the low speed welding condition. The depression area was found increased with the increasing of welding current. The large arc pressure may cause undercut defect for high speed welding.

The passive visual system requires simple experiment setup which is more practical

in manufacturing environment. New algorithms were developed to automatically calculated 3D weld pool surface geometry. The landmarks detection algorithm was developed to calcite the weld pool boundary from 2D passive vision images. It was found that the camera exposure time significantly affected the accuracy of edge detection on weld pool images. To solve this issue, the adaptive exposure control method was developed to adjust the camera exposure time under appropriate exposure condition. The bead on plate experiment shows that the accuracy of weld pool edge detection was improved with the adaptive exposure control method.

A new concept of using reversed electrode image (REI) to monitor weld pool surface height was first proposed in this work. It was found that the measured the distance between REI and electrode (DERI) is relevant to the weld pool surface shape. The increase of surface height will cause decrease of DERI. A reflection model was developed to calculate the SH based on the measurement of DERI, arc length and weld pool width. The method was verified with bead-on-plate experiments. The calculated SH is closely related to the face reinforcement of the weld bead. Thus, the convex and concave weld pool surface shape can be determined based on the calculation result.

The new software framework which integrated all the image processing algorithms was established to obtain three key features of 3D weld pool surface geometry such as weld pool width, trailing length and surface height in real time. The calculated weld pool width and surface height was close to the actual weld bead size measured after welding.

Another major contribution of this dissertation is applying machine learning methods to predict defect based on the features extracted from weld pool images. The supervised machine learning methods such as linear regression and bagging trees were applied to monitor welding penetration for bead on plate and butt-joint welding. The new features extracted from weld pool image and reversed electrode images played the important role to predict weld pool backside width during welding.

The developed algorithms have been further applied in U-groove welding joint. The obtained images have unique features compare to the bead on plate welding. It was found that the new features extracted from reversed electrode image was correlated with the penetration and lack of fusion. A new database was established for penetration prediction in root pass welding. And the bagging tree regression model was trained to predict backside width. Meanwhile, another database was also established for LOF defection. The classification model was trained to determine the fusion condition of the weld. The proposed method was applied on real time experiment. The limitation of the method is the root pass welding must be conducted without filler wire. And for all the multi-pass welds I did before, the welding torch must align with the center line of the U-groove. Thus, the method works better for narrow groove. For the U-groove with wide width, the addition experiment with swing touch should be conducted.

The close-loop control algorithms were further implemented to control uniform backside width during bead on plate weld. The predicted backside width was used as the feed back for prediction. The PID gains were adjusted to reduce the over shooting and setting time. Optimized PID gains were identified through MATLAB simulations. The optimal PID gains should be changed for different thickness workpiece. Thus, a self-tuning

PID controller was developed to perform backside width penetration control for the workpiece with changing thickness.

9.2 Future Work

The improvement of the work in this dissertation can be done in many aspects which include:

For current research of penetration prediction in bead on plate and butt-joint welding, the range of welding current is between 50A-150A, and travel speed is between 1-2mm/s. To improve the efficiency of welding, the high current and high-speed cases can be further studied. The weld pool surface geometry can be affected by the increasing arc pressure. The REI method can be further improved to be applied under these conditions. Besides that, machine learning algorithm such as convolution neural network, reinforce learning can be further applied to improve the accuracy of defect detection.

BIBLIOGRAPHY

[1] A. Boiler and P. V. Code, "Section VIII Division 1," NG-3000, 2004.
[2] J. C. Lippold, S. D. Kiser, and J. N. DuPont, Welding metallurgy and weldability of nickel-base alloys: John Wiley & Sons, 2011.
[3] Z. Chen, G. Yan, Z. Wang, and K. Wang, "Mechanical Design and Analysis of an Articulated-Tracked Robot for Pipe Inspection," in Robotic Welding, Intelligence and Automation, ed: Springer, 2011, pp. 461-467.
[4] S.-B. Chen and J. Wu, Intelligentized methodology for arc welding dynamical processes: Springer, 2009.
[5] Y.-K. Liu and Y.-M. Zhang, "Supervised learning of human welder behaviors for intelligent robotic welding," IEEE Transactions on Automation Science and Engineering, 2015.
[6] Y. Liu, Z. Shao, and Y. Zhang, "Learning human welder movement in pipe GTAW: a virtualized welding approach," Welding Journal, vol. 93, pp. 388s-398s, 2014.
[7] S. Rokhlin and A. Guu, "A study of arc force, pool depression, and weld penetration during gas tungsten arc welding," Welding Journal(USA), vol. 72, p. 381, 1993.
[8] X. Wang, "Three-dimensional vision-based sensing of GTAW: a review," The International Journal of Advanced Manufacturing Technology, vol. 72, pp. 333-345, 2014.
[9] Z. Rui, Z. Pu, D. Aiqing, and X. Peng, "Measurement of laser welding pool geometry using a closed convex active contour model," Measurement Science and Technology, vol. 25, p. 035603, 2014.
[10] D. Hardt and J. Katz, "Ultrasonic measurement of weld penetration," Welding Journal, vol. 63, pp. 273s-281s, 1984.
[11] S. Zhang, S. Hu, and Z. Wang, "Weld penetration sensing in pulsed gas tungsten arc welding based on arc voltage," Journal of materials processing technology, vol. 229, pp. 520-527, 2016.
[12] J. Wu and S. B. Chen, "Software System Designs of Real-Time Image Processing of Weld Pool Dynamic Characteristics," in Robotic Welding, Intelligence and Automation, T.-J. Tarn, S.-B. Chen, and C. Zhou, Eds., ed Berlin, Heidelberg: Springer Berlin Heidelberg, 2007, pp. 303-309.
[13] Y. J. Wenhang Li, Jing Wu, Jiayou Wang, "A modified welding image feature extraction algorithm for Rotating Arc Narrow Gap MAG Welding," Industrial Robot, An International Journal, vol. 42, 2015.
[14] W. Li, K. Gao, J. Wu, J. Wang, and Y. Ji, "Groove sidewall penetration modeling for rotating arc narrow gap MAG welding," The International Journal of Advanced Manufacturing Technology, vol. 78, pp. 573-581, 2015.
[15] H.-y. Shen, J. Wu, T. Lin, and S.-b. Chen, "Arc welding robot system with seam tracking and weld pool control based on passive vision," The International Journal of Advanced Manufacturing Technology, vol. 39, pp. 669-678, 2008.
[16] J. W. Wenhang Li, Ting Hu, Feng Yang, "Rough set based modeling for welding groove bottom state in narrow gap MAG welding," Industrial Robot: An International Journal, vol. 42, pp. 110-116, 2015.

[17] W.-H. Li, K. Gao, J. Wu, and J.-Y. Wang, "Modeling Welding Deviation of Rotating Arc NGW Based on Support Vector Machine," in Robotic Welding, Intelligence and Automation: RWIA'2014, T.-J. Tarn, S.-B. Chen, and X.-Q. Chen, Eds., ed Cham: Springer International Publishing, 2015, pp. 459-468.

[18] S. C. J. Wu, "Software System Designs of Real-time Image Processing of Weld Pool Dynamic Characteristics," in 2006 International Conference on Robotic Welding, Intelligence and Automation, Shanghai, China, 2006.

[19] J. Wu and S. Chen, "Software system designs of real-time image processing of weld pool dynamic characteristics," in Robotic Welding, Intelligence and Automation, ed: Springer, 2007, pp. 303-309.

[20] W. P. Gu, Z. Y. Xiong, and W. Wan, "Autonomous seam acquisition and tracking system for multi-pass welding based on vision sensor," The International Journal of Advanced Manufacturing Technology, vol. 69, pp. 451-460, October 01 2013.

[21] J. Wang, T. Lin, and S. Chen, "Obtaining weld pool vision information during aluminium alloy TIG welding," The International Journal of Advanced Manufacturing Technology, vol. 26, pp. 219-227, 2005.

[22] H.-C. Nguyen and B.-R. Lee, "Laser-vision-based quality inspection system for small-bead laser welding," International Journal of Precision Engineering and Manufacturing, vol. 15, pp. 415-423, March 01 2014.

[23] H. Chen, W. Liu, L. Huang, G. Xing, M. Wang, and H. Sun, "The decoupling visual feature extraction of dynamic three-dimensional V-type seam for gantry welding robot," The International Journal of Advanced Manufacturing Technology, vol. 80, pp. 1741-1749, October 01 2015.

[24] H. Y.-s. H. Z.-j. H. Z.-m. X. Xiao-wen, "An improved algorithm of close neighbor clustering was used on underwater weld recognition," Electric Welding Machine, vol. 43, pp. 89-92, 2013.

[25] B. Abdullah, J. Smith, W. Lucas, J. Lucas, and F. Malek, "Monitoring of TIG welding using laser and diode illumination sources: A comparison study," in Electronic Design, 2008. ICED 2008. International Conference on, 2008, pp. 1-4.

[26] Y. Zhang, R. Kovacevic, and S. Ruan, "Sensing and control of weld pool geometry for automated GTA welding," Transactions of the ASME, vol. 117, pp. 210-222, 1995.

[27] J. Liu, Z. Fan, S. I. Olsen, K. H. Christensen, and J. K. Kristensen, "Boosting Active Contours for Weld Pool Visual Tracking in Automatic Arc Welding," IEEE Transactions on Automation Science and Engineering, 2015.

[28] J. Liu, Fan, Z., Olsen, S., Christensen, K., and Kristensen, J., "A vision system without external illuminations for seam tracking and weld pool sensing in arc welding," presented at the The 16th International Conference on the Joining of Materials JOM16, Trieste, Italy, 2011.

[29] M. B. Gharsallah and E. B. Braiek, "Image segmentation for defect detection based on level set active contour combined with saliency map," in 2015 16th International Conference on Sciences and Techniques of Automatic Control and Computer Engineering (STA), 2015, pp. 388-392.

[30] D. Wu, M.-H. Hu, L.-L. Chen, H.-B. Chen, T. Lin, and S.-B. Chen, "Active Shape Model for Visual Detection and Localization of Variable Polarity PAW Weld

Pool," in Robotic Welding, Intelligence and Automation: RWIA'2014, T.-J. Tarn, S.-B. Chen, and X.-Q. Chen, Eds., ed Cham: Springer International Publishing, 2015, pp. 361-371.

[31] F. Shi, X. Huang, Y. Duan, and S. Chen, "Part-based model for visual detection and localization of gas tungsten arc weld pool," The International Journal of Advanced Manufacturing Technology, vol. 47, pp. 1097-1104, 2010/04/01 2010.

[32] H. Song and Y. Zhang, "Measurement and analysis of three-dimensional specular gas tungsten arc weld pool surface," WELDING JOURNAL-NEW YORK-, vol. 87, p. 85, 2008.

[33] H. S. Song and Y. M. Zhang, "Three-dimensional reconstruction of specular surface for a gas tungsten arc weld pool," Measurement Science and Technology, vol. 18, p. 3751, 2007.

[34] H. Song and Y. Zhang, "Image processing for measurement of three-dimensional GTA weld pool surface," WELDING JOURNAL-NEW YORK-, vol. 86, p. 323, 2007.

[35] B. Mi and C. Ume, "Real-time weld penetration depth monitoring with laser ultrasonic sensing system," Journal of manufacturing science and engineering, vol. 128, pp. 280-286, 2006.

[36] R. Kovacevic, Y. M. Zhang, and S. Ruan, "Sensing and Control of Weld Pool Geometry for Automated GTA Welding," Journal of Engineering for Industry, vol. 117, pp. 210-222, 1995.

[37] H. Song and Y. Zhang, "Error analysis of a three-dimensional GTA weld pool surface measurement system," Welding Journal, vol. 88, pp. 141-148, 2009.

[38] B. K. Horn, "Shape from shading: A method for obtaining the shape of a smooth opaque object from one view," 1970.

[39] J. Wang, L. Zhou, and S. Chen, "Measurement for three dimensional surface of welding pool in GTAW welding," in Robotic Welding, Intelligence and Automation, ed: Springer, 2007, pp. 219-225.

[40] R. Zhang, P.-S. Tsai, J. E. Cryer, and M. Shah, "Shape-from-shading: a survey," IEEE transactions on pattern analysis and machine intelligence, vol. 21, pp. 690-706, 1999.

[41] D. B. Zhao, J. Q. Yi, S. B. Chen, L. Wu, and Q. Chen, "Extraction of Three-Dimensional Parameters for Weld Pool Surface in Pulsed GTAW With Wire Filler," Journal of Manufacturing Science and Engineering, vol. 125, pp. 493-503, 2003.

[42] D. Zhao, Y. Lou, S. Chen, and L. Wu, "Surface height and geometry parameters for describing shape of weld pool during pulsed GTAW," in SPIE International Symposium on Intelligent System and Advanced Manufacturing, Boston, Massachusetts, USA, 1999, pp. 91-99.

[43] C. Mnich, F. Al-Bayat, C. Debrunner, J. Steele, and T. Vincent, "In situ weld pool measurement using stereovision," in Japan-USA Symposium on Flexible Automation, Denver, CO, 2004.

[44] B. Pan, K. Qian, H. Xie, and A. Asundi, "Two-dimensional digital image correlation for in-plane displacement and strain measurement: a review," Measurement science and technology, vol. 20, p. 062001, 2009.

[45] H. Bruck, S. McNeill, M. A. Sutton, and W. Peters Iii, "Digital image correlation using Newton-Raphson method of partial differential correction," Experimental Mechanics, vol. 29, pp. 261-267, 1989.

[46] B. Pan, A. Asundi, H. Xie, and J. Gao, "Digital image correlation using iterative least squares and pointwise least squares for displacement field and strain field measurements," Optics and Lasers in Engineering, vol. 47, pp. 865-874, 2009.

[47] M. A. Sutton, J. J. Orteu, and H. Schreier, Image correlation for shape, motion and deformation measurements: basic concepts, theory and applications: Springer Science & Business Media, 2009.

[48] B. Pan, H. Xie, Z. Guo, and T. Hua, "Full-field strain measurement using a two-dimensional Savitzky-Golay digital differentiator in digital image correlation," Optical Engineering, vol. 46, pp. 033601-033601-10, 2007.

[49] Y. Zhou, C. Sun, Y. Song, and J. Chen, "Image pre-filtering for measurement error reduction in digital image correlation," Optics and Lasers in Engineering, vol. 65, pp. 46-56, 2015.

[50] B. Pan, "Bias error reduction of digital image correlation using Gaussian pre-filtering," Optics and Lasers in Engineering, vol. 51, pp. 1161-1167, 2013.

[51] H. W. Schreier and M. A. Sutton, "Systematic errors in digital image correlation due to undermatched subset shape functions," Experimental Mechanics, vol. 42, pp. 303-310, 2002.

[52] A. Reynolds and F. Duvall, "Digital image correlation for determination of weld and base metal constitutive behavior," WELDING JOURNAL-NEW YORK-, vol. 78, pp. 355-s, 1999.

[53] C. Leitão, I. Galvão, R. Leal, and D. Rodrigues, "Determination of local constitutive properties of aluminium friction stir welds using digital image correlation," Materials & Design, vol. 33, pp. 69-74, 2012.

[54] B. Grant, H. Stone, P. Withers, and M. Preuss, "High-temperature strain field measurement using digital image correlation," The Journal of Strain Analysis for Engineering Design, vol. 44, pp. 263-271, 2009.

[55] M. De Strycker, P. Lava, W. Van Paepegem, L. Schueremans, and D. Debruyne, "Measuring welding deformations with the digital image correlation technique," Welding Journal, vol. 90, pp. 107-112, 2011.

[56] H. Coules, P. Colegrove, L. Cozzolino, and S. Wen, "Experimental measurement of biaxial thermal stress fields caused by arc welding," Journal of Materials Processing Technology, vol. 212, pp. 962-968, 2012.

[57] J. Chen, X. Yu, R. G. Miller, and Z. Feng, "In situ strain and temperature measurement and modelling during arc welding," Science and Technology of Welding and Joining, vol. 20, pp. 181-188, 2015/03/18 2015.

[58] N. Ma, H. Huang, X. Yin, and N. Guo, "Welding distortion and inherent deformation under temporary tacking and its released states," Science and Technology of Welding and Joining, vol. 21, pp. 389-396, 2016.

[59] N. Ma, H. Huang, and H. Murakawa, "Effect of jig constraint position and pitch on welding deformation," Journal of Materials Processing Technology, vol. 221, pp. 154-162, 2015.

[60] W. Cheng, "In-plane shrinkage strains and their effects on welding distortion in thin-wall structures," The Ohio State University, 2005.

[61] Z. Chen, J. Chen, and Z. Feng, "Strain Measurement in Arc Welding using Digital Image Correlation," Oak Ridge National Lab.(ORNL), Oak Ridge, TN (United States)2016.

[62] Z. Chen, J. Chen, Z. Feng, and Y. Zhang, "In situ strain monitoring in gas tungsten arc welding processes," in Advanced Intelligent Mechatronics (AIM), 2016 IEEE International Conference on, 2016, pp. 800-804.

[63] J. Chen, J. Tatman, Z. Chen, Z. Feng, and G. Frederick, "Proactive In-Situ Welding Stress Control for Laser Repair Welding of Irradiated Austenitic Materials," in ASME 2017 Pressure Vessels and Piping Conference, 2017, pp. V06BT06A020-V06BT06A020.

[64] S. Chen, J. Wu, and Q. Du, "Non-linear modelling and compound intelligent control of pulsed gas tungsten arc welding dynamics," Proceedings of the Institution of Mechanical Engineers, Part I: Journal of Systems and Control Engineering, vol. 225, pp. 113-124, 2011.

[65] S. Chen and J. Wu, "A Survey on Intelligentized Technologies for Visual Information Acquirement, modeling and Control of Arc Welding Pool Dynamics," in Industrial Electronics Society, 2007. IECON 2007. 33rd Annual Conference of the IEEE, 2007, pp. 781-785.

[66] Z. Chen and X. Gao, "Detection of weld pool width using infrared imaging during high-power fiber laser welding of type 304 austenitic stainless steel," The International Journal of Advanced Manufacturing Technology, vol. 74, pp. 1247-1254, 2014.

[67] K. Pal and S. K. Pal, "Monitoring of weld penetration using arc acoustics," Materials and Manufacturing Processes, vol. 26, pp. 684-693, 2011.

[68] S. Chokkalingham, N. Chandrasekhar, and M. Vasudevan, "Predicting the depth of penetration and weld bead width from the infra red thermal image of the weld pool using artificial neural network modeling," Journal of Intelligent Manufacturing, vol. 23, pp. 1995-2001, 2012.

[69] S. Chen, Y. Lou, L. Wu, and D. Zhao, "Intelligent methodology for sensing, modeling and control of pulsed GTAW: Part 1--Bead-on-plate welding," Welding Journal(USA), vol. 79, p. 151, 2000.

[70] S. Chen, D. Zhao, L. Wu, and Y. Lou, "Intelligent methodology for sensing, modeling and control of pulsed GTAW: Part 2--Butt joint welding," Welding Journal(USA), vol. 79, p. 164, 2000.

[71] S. Chen, D. Zhao, Y. Lou, and L. Wu, "Computer vision sensing and intelligent control of welding pool dynamics," in Robotic Welding, Intelligence and Automation, ed: Springer, 2004, pp. 25-55.

[72] X. Li, Z. Shao, Y. Zhang, and L. Kvidahl, "Monitoring and control of penetration in GTAW and pipe welding," Weld. J, vol. 92, pp. 190S-196S, 2013.

[73] Z. Wang, Y. Zhang, and L. Wu, "Measurement and estimation of weld pool surface depth and weld penetration in pulsed gas metal arc welding," Welding Journal, vol. 89, pp. 117s-126s, 2010.

[74] J. Wu and S.-b. Chen, "DIDO Hammerstein identification of mild steel welding pool in pulsed GTAW dynamic process with wire filler," arXiv preprint arXiv:1804.09258, 2018.

[75] T.-Y. Wu and I. C. Ume, "Prediction and experimental validation of penetration depth of butt welds in thin plates using superimposed laser sources," NDT & E International, vol. 50, pp. 10-19, 2012.

[76] R. Fenn and Y. Lu, "A real-time welding quality control and assessment system," Insight, vol. 39, pp. 93-96, 1997.

[77] S. Wu, H. Gao, W. Zhang, and Y. Zhang, "Real-time estimation of weld penetration using weld pool surface based calibration," in Industrial Electronics Society, IECON 2016-42nd Annual Conference of the IEEE, 2016, pp. 294-299.

[78] M. Hermans, B. Yudodibroto, Y. Hirata, G. den Ouden, and I. Richardson, "The oscillation behaviour of liquid metal in arc welding," in Materials science forum, 2007, pp. 3877-3882.

[79] Y. Shi, G. Zhang, X. Ma, Y. Gu, J. Huang, and D. Fan, "Laser Vision Based Measurement and Analysis of Weld Pool Oscillation Frequency in GTAW-P," Welding Journal, vol. 94, pp. 176s-187s, 2015.

[80] C. Sorensen and T. Eagar, "Modeling of oscillations in partially penetrated weld pools," Journal of dynamic systems, measurement, and control, vol. 112, pp. 469-474, 1990.

[81] Y. Xiao and G. Den Ouden, "A study of GTA weld pool oscillation," Weld. J., vol. 69, p. 289, 1990.

[82] N. Lv, Y. Xu, J. Zhong, H. Chen, J. Wang, and S. Chen, "Research on detection of welding penetration state during robotic GTAW process based on audible arc sound," Industrial Robot: An International Journal, vol. 40, pp. 474-493, 2013.

[83] N. Lv, J. Zhong, H. Chen, T. Lin, and S. Chen, "Real-time control of welding penetration during robotic GTAW dynamical process by audio sensing of arc length," The International Journal of Advanced Manufacturing Technology, vol. 74, pp. 235-249, 2014.

[84] P. Li and Y.-M. Zhang, "Robust sensing of arc length," IEEE Transactions on instrumentation and measurement, vol. 50, pp. 697-704, 2001.

[85] S. Egerland, "A Contribution to Arc Length Discussion," Soldagem & Inspeção, vol. 20, pp. 367-380, 2015.

[86] Y. Zhang, X. Li, and Z. Shao, "Method to monitor and control weld penetration in gas tungsten welding and full-position pipe welding," ed: Google Patents, 2017.

[87] Z. Li, X. Gu, Y. Wang, and C. Xue, "Radiation of arc and its application in GTA welding measurement and testing," in Measuring Technology and Mechatronics Automation, 2009. ICMTMA'09. International Conference on, 2009, pp. 100-103.

[88] M. Lin and T. Eagar, "Influence of arc pressure on weld pool geometry," Welding Journal, vol. 64, pp. 163s-169s, 1985.

[89] M. Lin and T. Eagar, "Influence of surface depression and convection on arc weld pool geometry," Transport Phenomena in Materials Processing, vol. 10, pp. 63-69, 1983.

[90] R. Choo, J. Szekely, and R. Westhoff, "Modeling of high-current arcs with emphasis on free surface phenomena in the weld pool," Welding Journal, vol. 69, pp. 346-361, 1990.

[91] Y. Zhang, Z. Cao, and R. Kovacevic, "Numerical analysis of fully penetrated weld pools in gas tungsten arc welding," Proceedings of the Institution of Mechanical Engineers, Part C: Journal of Mechanical Engineering Science, vol. 210, pp. 187-195, 1996.

[92] T. Nguyen, D. Weckman, D. Johnson, and H. Kerr, "High speed fusion weld bead defects," Science and Technology of Welding and Joining, vol. 11, pp. 618-633, 2006.

[93] T. Nguyen, D. Weckman, D. Johnson, and H. Kerr, "The humping phenomenon during high speed gas metal arc welding," Science and Technology of Welding and Joining, vol. 10, pp. 447-459, 2005.

[94] B. Scholkopf, Smola, A., Learning with kernels. Cambridge, MA: MIT Press, 2002.

[95] W. Li, K. Gao, J. Wu, T. Hu, and J. Wang, "SVM-based information fusion for weld deviation extraction and weld groove state identification in rotating arc narrow gap MAG welding," The International Journal of Advanced Manufacturing Technology, vol. 74, pp. 1355-1364, 2014.

[96] J. Wu, E. E. Abdel-Fatah, and M. R. Mahfouz, "Fully automatic initialization of two-dimensional–three-dimensional medical image registration using hybrid classifier," Journal of Medical Imaging, vol. 2, p. 024007, 2015.

[97] J. Wu, "2D-3D Registration of Knee Joint from Single Plane X-ray Fluoroscopy Using Nonlinear Shape Priors," 2016.

[98] E. B. Dos Santos, L. H. Kuroiwa, A. F. C. Ferreira, R. Pistor, and A. P. Gerlich, "On the Visualization of Gas Metal Arc Welding Plasma and the Relationship Between Arc Length and Voltage," Applied Sciences, vol. 7, p. 503, 2017.

[99] Z. Chen, J. Chen, and Z. Feng, "Welding penetration prediction with passive vision system," Journal of Manufacturing Processes, vol. 36, pp. 224-230, 2018.

[100] G. Zhang, Y. Shi, Y. Gu, D. Fan, and M. Zhu, "Laser Vision-Based Detection of Weld Penetration in GTAW An inspection method was proposed to monitor weld penetration for investigating the control of weld defects," Welding Journal, vol. 96, pp. 163S-172S, May 2017.

[101] W. Zhang, Y. Liu, X. Wang, and Y. Zhang, "Characterization of three-dimensional weld pool surface in GTAW," Welding Journal, vol. 91, pp. 195s-203s, 2012.

[102] R. Kovacevic, Y. Zhang, and L. Li, "Monitoring of Weld Joint Penetrations Based on Weld Pool Geometrical Appearance," Welding Journal-Including Welding Research Supplement, vol. 75, pp. 317-329, 1996.

[103] R. Genuer, J.-M. Poggi, and C. Tuleau-Malot, "Variable selection using random forests," Pattern Recognition Letters, vol. 31, pp. 2225-2236, 2010.

[104] B. Gregorutti, B. Michel, and P. Saint-Pierre, "Correlation and variable importance in random forests," Statistics and Computing, vol. 27, pp. 659-678, 2017.

[105] A. Ghasempoor, P. Wild, M. Auger, and R. Mueller, "Automatic detection of lack of fusion defects in CO 2 laser gear welding," Journal of laser applications, vol. 15, pp. 77-83, 2003.

[106] M. Jovanović, G. Rihar, and J. Grum, Analysis of ultrasonic indications in lack of fusion occuring in welds, 2006.

[107] Z. Chen, J. Chen, and Z. Feng, "Monitoring Weld Pool Surface and Penetration Using Reversed Electrode Images," Welding Journal, vol. 96, pp. 367S-375S, 2017.

VITA

Zongyao Chen was born in Heilongjiang, China in 1987. He attended Shanghai Jiaotong University in 2005, receiving his Bachelor of Science and Master of Science degree in Electrical Engineering in 2009 and 2012. He came to United States for his Ph.D. at the University of Tennessee since 2012.

During his early stage in graduate school, he made his effort in design and implement of mobile and under water robotic system. He joined welding and joining research group in oak ridge national lab in 2015 under the supervision of Dr. Zhili Feng and Dr. Jian Chen. Then his started focusing on applying artificial intelligent and computer vision technology on welding and manufacturing.

Zongyao's current research interests include robotic, welding automation, computer vision and machine learning.